Journal of Scientific Computing (2023) 97:52
https://doi.org/10.1007/s10915-023-02351-x

A Broken FEEC Framework for Electromagnetic Problems on Mapped Multipatch Domains

Yaman Güçlü[1] · **Said Hadjout**[2] · **Martin Campos Pinto**[1]

Received: 6 October 2022 / Revised: 4 August 2023 / Accepted: 5 September 2023 /
Published online: 12 October 2023
© The Author(s) 2023, corrected publication 2023

Abstract

We present a framework for the structure-preserving approximation of partial differential equations on mapped multipatch domains, extending the classical theory of finite element exterior calculus (FEEC) to discrete de Rham sequences which are broken, i.e., fully discontinuous across the patch interfaces. Following the Conforming/Nonconforming Galerkin (CONGA) schemes developed in Campos Pinto and Sonnendrücker (Math Comput 85:2651–2685, 2016) and Campos Pinto and Güçlü (Broken-FEEC discretizations and Hodge Laplace problems. arXiv:2109.02553, 2022), our approach is based on: (i) the identification of a conforming discrete de Rham sequence with stable commuting projection operators, (ii) the relaxation of the continuity constraints between patches, and (iii) the construction of conforming projections mapping back to the conforming subspaces, allowing to define discrete differentials on the broken sequence. This framework combines the advantages of conforming FEEC discretizations (e.g. commuting projections, discrete duality and Hodge–Helmholtz decompositions) with the data locality and implementation simplicity of interior penalty methods for discontinuous Galerkin discretizations. We apply it to several initial- and boundary-value problems, as well as eigenvalue problems arising in electromagnetics. In each case our formulations are shown to be well posed thanks to an appropriate stabilization of the jumps across the interfaces, and the solutions are extremely robust with respect to the stabilization parameter. Finally we describe a construction using tensor-product splines on mapped cartesian patches, and we detail the associated matrix operators. Our numerical experiments confirm the accuracy and stability of this discrete framework, and they allow us to verify that expected structure-preserving properties such as divergence or harmonic constraints are respected to floating-point accuracy.

✉ Martin Campos Pinto
martin.campos-pinto@ipp.mpg.de

Yaman Güçlü
yaman.guclu@ipp.mpg.de

Said Hadjout
saidaissa.hadjout@tum.de

[1] NMPP Division, Max-Planck-Institut für Plasmaphysik, Garching bei München, Germany

[2] Department of Mathematics, Technische Universität München, Garching bei München, Germany

Keywords Finite element exterior calculus · Broken spaces · Mapped multipatch geometry · Compatible Discretization · Electromagnetic Simulation

Mathematics Subject Classification 65M60 · 65N30 · 65N25

1 Introduction

Thanks to enlightening research conducted over the last few decades [1, 6, 11, 15, 33, 35, 38], it is now well understood that preserving the geometrical de Rham structure of physical problems is a key tool in the design of good finite element methods. A significant field of success is electromagnetics, where this principle has produced stable and accurate discretization methods, from simplicial Whitney forms [9, 49] to high order curved elements in isogeometric analysis [14, 27], via edge Nédélec elements [8, 42]. The latter, in particular, have been proven to yield Maxwell solvers that are free of spurious eigenmodes in a series of works dedicated to this issue [7, 10, 26, 43]. Here the existence of stable commuting projection operators plays a central role, as highlighted in the unifying analysis of finite element exterior calculus (FEEC) [1, 2].

A central asset of structure-preserving finite elements is their ability to reproduce discrete Hodge–Helmholtz decompositions which, in combination with proper commuting projection operators, allow them to preserve important physical invariants such as the divergence constraints in Maxwell's equations [21, 22, 44], or the Hamiltonian structure of the MHD and Vlasov–Maxwell equations [24, 36, 40]. In the latter application the aforementioned commuting projection operators couple structure-preserving finite element fields with numerical particles.

As they primarily involve strong differential operators, structure-preserving finite elements have been essentially developed within the scope of *conforming* methods, where the discrete spaces form a sub-complex of the continuous de Rham sequence. In practice this imposes continuity conditions at the cell interfaces which strongly degrade the locality of key operations such as L^2 projections, as sparse finite element mass matrices have no sparse inverses in general. In the natural framework of dual complexes composed of weak differential operators, this leads to Galerkin Hodge operators which are *global*, in the sense that on a given cell their values depend a priori on the function values on the whole domain. As the Hodge operators allow to map from the dual spaces to the primal ones, this results in discrete coderivatives operators that share this undesirable globality property. Furthermore the canonical commuting projection operators for the dual sequence are also global, since they coincide with the L^2 projections on the discrete finite element spaces. This feature makes their application potentially expensive on fine meshes, and it represents a serious hurdle in parallel codes where communications between distant cells should be avoided as much as possible.

In this article we follow the *broken* FEEC approach [23] first developed for Conforming/Nonconforming Galerkin (CONGA) schemes in [18, 19]. The principle is to consider local de Rham sequences on subdomains (which we shall call patches) and discretize the global problems with broken finite element spaces, which are fully discontinuous at the patch interfaces. Strong differential operators are then obtained by composing the local (broken) ones with conforming projection operators that enforce the proper continuity conditions at the interfaces. Being fully discontinuous at the patch interfaces, the broken finite element spaces have mass matrices which are block diagonal (with blocks corresponding to patches)

so that the inverse mass matrices are also block diagonal. This readily yields L^2 projections and Galerkin Hodge operators which are patch-local.

Since the coupling between neighboring patches is encoded by discrete conforming projection operators which in practice involve the averaging of degrees of freedom across interfaces, the corresponding derivative and coderivative operators are *local* in the sense that on a given patch their values only depend on the function values on the contiguous patches. In addition our broken FEEC sequences admit dual commuting projection operators that involve L^2 projections on the broken spaces and transposed conforming projection matrices [23], so these are also local.

The good news is that this approach does not sacrifice structure preservation, indeed our broken FEEC sequences satisfy primal/dual commuting diagrams, uniform stability estimates and discrete Hodge–Helmholtz decompositions [18, 23]. In particular, broken FEEC sequences should allow one to construct structure-preserving finite element solvers on complex domains with enhanced locality properties.

In the present work we follow this principle and propose specific numerical schemes for several boundary value problems arising in electromagnetics. We describe their precise form in the case of multipatch mapped spline spaces [15, 27] on general non-contractible domains, and we perform several numerical experiments to study their practical behaviour. As our results show, this approach indeed allows us to preserve most properties of the conforming FEEC approximations, such as stability and accuracy of the solutions, topological invariants, as well as harmonic and divergence constraints of the discrete fields.

The outline is as follows: We first recall in Sect. 2 the main lines of FEEC discretizations using conforming spaces and we describe their extension to broken spaces, with a detailed description of the fully discrete diagrams involving the primal (strong) and dual (weak) de Rham sequences and their respective broken commuting projection operators. In Sect. 3 we apply this discretization framework to a series of classical electromagnetic problems, namely Poisson's and harmonic Maxwell's equations, curl-curl eigenvalue problems, and magnetostatic problems; we also recall the approximation of the time-dependent Maxwell equations from Campos Pinto and Sonnendrücker [18]. For each problem we state a priori results about the solutions, assuming the well-posedness of the corresponding conforming FEEC discretization. In Sect. 4 we detail the construction of a geometric broken FEEC spline discretization on mapped multipatch domains. Here we consider a 2D setting for simplicity, but the same method applies to 3D domains. In Sect. 5 we conduct extensive numerical experiments for the electromagnetic problems described in the article, which verify the robustness of our approach. Finally, in Sect. 6 we summarize the main results of our work and provide an outlook on future research.

Some necessary "standard" definitions are specified in the Appendix, which provides a self-contained notation for the material of Sect. 4: Appendix Sect. A describes the construction of broken multipatch spline complexes, while Appendix Sect. B defines the geometric degrees of freedom and the corresponding commuting projection operators.

2 Principle of FEEC and Broken FEEC Discretizations

2.1 De Rham Sequences and Hodge–Helmholtz Decompositions

In this work we consider discretizations of Hilbert de Rham sequences. At the continuous level these are of the form

$$V^0 \xrightarrow{\text{grad}} V^1 \xrightarrow{\text{curl}} V^2 \xrightarrow{\text{div}} V^3 \tag{1}$$

with infinite-dimensional spaces such as

$$V^0 = H_0^1(\Omega), \quad V^1 = H_0(\text{curl};\Omega), \quad V^2 = H_0(\text{div};\Omega), \quad V^3 = L^2(\Omega). \tag{2}$$

Following the well established analysis of Hilbert complexes by Arnold, Falk and Winther [1, 2] we also consider the dual sequence

$$V_0^* \xleftarrow{\text{div}} V_1^* \xleftarrow{\text{curl}} V_2^* \xleftarrow{\text{grad}} V_3^* \tag{3}$$

involving the adjoint differential operators (denoted with their usual name) and their corresponding domains, namely

$$V_3^* = H^1(\Omega), \quad V_2^* = H(\text{curl};\Omega), \quad V_1^* = H(\text{div};\Omega), \quad V_0^* = L^2(\Omega). \tag{4}$$

Here the construction is symmetric, in the sense that the inhomogeneous sequence (4) could have been chosen for the primal one and the homogeneous (2) for the dual one. Since the symmetry is broken in the finite element discretization, to fix the ideas in this article we mostly consider the choice (1)–(4), except for a few places where we adopt a specific notation. A key property of these sequences is that each operator maps into the kernel of the next one, i.e., we always have $\text{curl}\,\text{grad} = 0$ and $\text{div}\,\text{curl} = 0$. This allows us to write an orthogonal Hodge–Helmholtz decomposition for $L^2(\Omega)^3$, of the form

$$L^2(\Omega)^3 = \text{grad}\, V^0 \overset{\perp}{\oplus} \mathcal{H}^1 \overset{\perp}{\oplus} \text{curl}\, V_2^* \tag{5}$$

where $\mathcal{H}^1 := \{v \in V^1 \cap V_1^* : \text{curl}\, v = \text{div}\, v = 0\}$, see e.g. [2, Eq. (15)]. This space corresponds to harmonic 1-forms, as it coincides with the kernel of the 1-form Hodge–Laplace operator

$$\mathcal{L}^1 := -\,\text{grad}\,\text{div} + \text{curl}\,\text{curl} \tag{6}$$

seen as an operator $\mathcal{L}^1 : D(\mathcal{L}^1) \to L^2(\Omega)$ with domain space

$$D(\mathcal{L}^1) := \{v \in V^1 \cap V_1^* : \text{curl}\, v \in V_2^* \text{ and } \text{div}\, v \in V^0\}. \tag{7}$$

Another orthogonal decomposition for $L^2(\Omega)^3$ is

$$L^2(\Omega)^3 = \text{curl}\, V^1 \overset{\perp}{\oplus} \mathcal{H}^2 \overset{\perp}{\oplus} \text{grad}\, V_3^*, \tag{8}$$

where $\mathcal{H}^2 := \{w \in V^2 \cap V_2^* : \text{curl}\, w = \text{div}\, w = 0\}$ is the space of harmonic 2-forms, which coincides with the kernel of the 2-form Hodge–Laplace operator $\mathcal{L}^2 := -\,\text{grad}\,\text{div} + \text{curl}\,\text{curl}$ with domain space $D(\mathcal{L}^2) := \{w \in V^2 \cap V_2^* : \text{curl}\, w \in V_1^* \text{ and } \text{div}\, w \in V^3\}$.

We point out that, while the 1-form and 2-form Hodge–Laplace operators are formally identical, their domain spaces differ in the boundary conditions and hence $\mathcal{H}^1 \neq \mathcal{H}^2$: in the case considered here where the primal sequence has homogeneous boundary conditions, the harmonic 1-forms have vanishing tangential trace on $\partial\Omega$, while the harmonic 2-forms have vanishing normal trace on $\partial\Omega$. In the symmetric case where the non-homogeneous de Rham sequence is considered as the primal one, one obtains the same decompositions (5) and (8) but with opposite order: $(\mathcal{H}^\ell)_{\text{non-hom.}} = \mathcal{H}^{3-\ell}$. This isomorphism, known as Poincaré duality, is provided by the Hodge star operator; see [2, Sects. 5.6, 6.2].

On contractible domains the above sequences are exact in the sense that the image of each operator coincides exactly with the kernel of the next one, and the harmonic space is trivial, $\mathcal{H}^1 = \{0\}$. However if the domain Ω is non-contractible, this is no longer the case

and there exist non trivial harmonic forms. Indeed, the dimensions of these two harmonic spaces depend on the domain topology: $\dim(\mathcal{H}^2) = \dim(\mathcal{H}^1)_{\text{non-hom.}} = b_1(\Omega)$ is the first Betti number, which counts the number of "tunnels" through the domain, while $\dim(\mathcal{H}^1) = \dim(\mathcal{H}^2)_{\text{non-hom.}} = b_2(\Omega)$ is the second Betti number, which counts the number of "voids" enclosed by the domain.

2.2 Conforming FEEC Discretizations

Finite Element Exterior Calculus (FEEC) discretizations consist of Finite Element spaces that form discrete de Rham sequences,

$$V_h^{0,c} \xrightarrow{\text{grad}} V_h^{1,c} \xrightarrow{\text{curl}} V_h^{2,c} \xrightarrow{\text{div}} V_h^{3,c} . \tag{9}$$

Here, the superscript c indicates that the spaces are assumed *conforming* in the sense that $V_h^{\ell,c} \subset V^\ell$, and the subscript h loosely represents some discretization parameters, such as the resolution of an underlying mesh. A key tool in the analysis of FEEC discretizations is the existence of projection operators $\Pi_h^{\ell,c} : V^\ell \to V_h^{\ell,c}$ that commute with the differential operators, in the sense that the relation

$$d^\ell \Pi_h^{\ell,c} v = \Pi_h^{\ell+1,c} d^\ell v \quad v \in V^\ell \tag{10}$$

holds for the different operators in the sequence (9),

$$d^0 = \text{grad}, \quad d^1 = \text{curl}, \quad d^2 = \text{div} . \tag{11}$$

In particular, the stability and the accuracy of several discrete problems posed in the sequence (9), relative to usual discretization parameters such as the mesh resolution h or the order of the finite element spaces, follow from the stability of the commuting projections in V^ℓ or L^2 norms, see e.g. [2, Theorems 3.9, 3.19].

Denoting explicitly by

$$\text{grad}_h^c := \text{grad}\,|_{V_h^{0,c}}, \quad \text{curl}_h^c := \text{curl}\,|_{V_h^{1,c}}, \quad \text{div}_h^c := \text{div}\,|_{V_h^{2,c}} \tag{12}$$

the differential operators restricted to the discrete spaces, we define their adjoints by discrete L^2 duality, i.e.,

$$\begin{cases} \langle (\text{grad}_h^c)^* v, \varphi \rangle = \langle v, \text{grad}\, \varphi \rangle & \forall v \in V_h^{1,c},\ \varphi \in V_h^{0,c} \\ \langle (\text{curl}_h^c)^* w, v \rangle = \langle w, \text{curl}\, v \rangle & \forall w \in V_h^{2,c},\ v \in V_h^{1,c} \\ \langle (\text{div}_h^c)^* \rho, w \rangle = \langle \rho, \text{div}\, w \rangle & \forall \rho \in V_h^{3,c},\ w \in V_h^{2,c} \end{cases} \tag{13}$$

where $\langle \cdot, \cdot \rangle$ denotes the $L^2(\Omega)$ scalar product. Owing to the homogeneous boundary conditions, we denote the resulting coderivative operators by

$$\begin{cases} \widetilde{\text{div}}_h^c := (-\text{grad}_h^c)^* : & V_h^{1,c} \to V_h^{0,c} \\ \widetilde{\text{curl}}_h^c := (\text{curl}_h^c)^* : & V_h^{2,c} \to V_h^{1,c} \\ \widetilde{\text{grad}}_h^c := (-\text{div}_h^c)^* : & V_h^{3,c} \to V_h^{2,c}. \end{cases} \tag{14}$$

This yields a compatible discretization of both the primal and dual sequences (1) and (3), in strong and weak form, respectively, using the same spaces (9). Note that in (13) the discrete spaces $V_h^{\ell,c}$ are implicitely identified with their dual spaces when equipped with the L^2 norm,

which is standard practice, see e.g. [2, Sec 3.3]. This framework can be summarized in the following diagram

$$
\begin{array}{ccccccc}
V^0 & \xrightarrow{\text{grad}} & V^1 & \xrightarrow{\text{curl}} & V^2 & \xrightarrow{\text{div}} & V^3 \\
\downarrow \Pi_h^{0,c} & & \downarrow \Pi_h^{1,c} & & \downarrow \Pi_h^{2,c} & & \downarrow \Pi_h^{3,c} \\
V_h^{0,c} & \underset{\widetilde{\text{div}}_h^c}{\overset{\text{grad}_h^c}{\rightleftarrows}} & V_h^{1,c} & \underset{\widetilde{\text{curl}}_h^c}{\overset{\text{curl}_h^c}{\rightleftarrows}} & V_h^{2,c} & \underset{\widetilde{\text{grad}}_h^c}{\overset{\text{div}_h^c}{\rightleftarrows}} & V_h^{3,c} \\
\uparrow Q_{V_h^{0,c}} & & \uparrow Q_{V_h^{1,c}} & & \uparrow Q_{V_h^{2,c}} & & \uparrow Q_{V_h^{3,c}} \\
V_0^* & \xleftarrow{\text{div}} & V_1^* & \xleftarrow{\text{curl}} & V_2^* & \xleftarrow{\text{grad}} & V_3^*
\end{array}
\tag{15}
$$

where the operators $Q_{V_h^{\ell,c}} : L^2(\Omega) \to V_h^{\ell,c}$ represent L^2 projections to the conforming discrete spaces. We observe that these projections commute with the dual differential operators, as a result of (14).

Assumption 1 Throughout the article we assume that the primal projection operators $\Pi_h^{\ell,c}$ are L^2 stable and satisfy the commuting property (10).

Remark 1 In practice commuting projection operators also play an important role as they permit to approximate coupling or source terms in a structure-preserving way, see e.g. [24]. For this purpose V^ℓ or L^2-stable projections may not be the best choices as they can be difficult to apply, and simpler commuting projections, defined through proper degrees of freedom, are often preferred. These projections are then usually defined on sequences

$$
U^0 \xrightarrow{\text{grad}} U^1 \xrightarrow{\text{curl}} U^2 \xrightarrow{\text{div}} U^3 \tag{16}
$$

involving spaces $U^\ell \subset V^\ell$ that require more smoothness (or integrability) as the ones in (2). We refer to e.g. [5, 24, 41, 45] for some examples, and to Sect. 2.4 below for more details on such constructions.

Another asset of FEEC discretizations is to provide structure-preserving Hodge–Helmholtz decompositions for the different spaces. For 1-forms, the discrete analog of the continuous decomposition (5) reads

$$
V_h^{1,c} = \text{grad}_h^c \, V_h^{0,c} \overset{\perp}{\oplus} \mathcal{H}_h^1 \overset{\perp}{\oplus} \widetilde{\text{curl}}_h^c \, V_h^{2,c} \tag{17}
$$

where $\mathcal{H}_h^1 := \{v \in V_h^{1,c} : \text{curl}_h^c \, v = \widetilde{\text{div}}_h^c v = 0\}$ is the kernel of the discrete Hodge–Laplace operator $\mathcal{L}_h^{1,c} : V_h^{1,c} \to V_h^{1,c}$ defined as

$$
\mathcal{L}_h^{1,c} := -\,\text{grad}_h^c \, \widetilde{\text{div}}_h^c + \widetilde{\text{curl}}_h^c \, \text{curl}_h^c \ . \tag{18}
$$

The space $\mathcal{H}_h^1$ may thus be seen as discrete harmonic 1-forms and under suitable approximation properties of the discrete spaces, its dimension coincides with that of the continuous harmonic forms $\mathcal{H}^1$, which corresponds to a Betti number of Ω depending on the boundary conditions, see [2, Sects. 5.6, 6.2].

2.3 Broken FEEC Discretizations

In the case where the domain is decomposed in a partition of open subdomains Ω_k, $k = 1, \dots, K$, we now consider local FEEC sequences

$$V_h^0(\Omega_k) \xrightarrow{\text{grad}_{\Omega_k}} V_h^1(\Omega_k) \xrightarrow{\text{curl}_{\Omega_k}} V_h^2(\Omega_k) \xrightarrow{\text{div}_{\Omega_k}} V_h^3(\Omega_k) \tag{19}$$

and global spaces obtained by a simple juxtaposition of the local ones

$$V_h^\ell := \{v \in L^2(\Omega) : v|_{\Omega_k} \in V_h^\ell(\Omega_k)\}. \tag{20}$$

One attractive feature of the broken spaces (20) is that they are naturally equipped with local basis functions Λ_i^ℓ that are supported each on a single patch Ω_k with $k = k(i)$. The corresponding mass matrices are then patch-diagonal, i.e., block-diagonal with blocks corresponding to the different patches, so that their inversion – and hence the L^2 projection on V_h^ℓ – can be performed in each patch independently of the others.

However, the spaces (20) are in general not subspaces of their infinite-dimensional counterparts, indeed it is well-known that piecewise smooth fields must satisfy some interface constraints in order to be globally smooth [5]: for H^1 smoothness the fields must be continuous on the interfaces, while $H(\text{curl})$ and $H(\text{div})$ smoothness of vector-valued fields require the continuity of the tangential and normal components, respectively, on the interfaces. As these constraints are obviously not satisfied by the broken spaces (20), we have in general

$$V_h^\ell \not\subset V^\ell.$$

The approach developed for the CONGA schemes in [18, 23] extends the construction of Sect. 2.2 to this broken FEEC setting, by associating to each discontinuous space a projection operator on its conforming subspace,

$$P_h^\ell : V_h^\ell \to V_h^\ell \cap V^\ell =: V_h^{\ell,c}. \tag{21}$$

In practice P_h^ℓ can be defined by a local averaging of interface degrees of freedom.

Provided that these conforming spaces form a de Rham sequence (9), this allows us to define new primal differential operators on the broken spaces

$$\begin{cases} \text{grad}_h := \text{grad}\, P_h^0 & : V_h^0 \to V_h^{1,c} \subset V_h^1 \\ \text{curl}_h := \text{curl}\, P_h^1 & : V_h^1 \to V_h^{2,c} \subset V_h^2 \\ \text{div}_h := \text{div}\, P_h^2 & : V_h^2 \to V_h^{3,c} \subset V_h^3 \end{cases} \tag{22}$$

and new dual ones $\widetilde{\text{div}}_h : V_h^1 \to V_h^0$, $\widetilde{\text{curl}}_h : V_h^2 \to V_h^1$ and $\widetilde{\text{grad}}_h : V_h^3 \to V_h^2$ as discrete L^2 adjoints, characterized by the relations

$$\begin{cases} \langle \widetilde{\text{div}}_h v, \varphi \rangle = -\langle v, \text{grad}\, P_h^0 \varphi \rangle & \forall\, v \in V_h^1, & \varphi \in V_h^0 \\ \langle \widetilde{\text{curl}}_h w, v \rangle = \langle w, \text{curl}\, P_h^1 v \rangle & \forall\, w \in V_h^2,\ v \in V_h^1 & \\ \langle \widetilde{\text{grad}}_h \rho, w \rangle = -\langle \rho, \text{div}\, P_h^2 w \rangle & \forall\, \rho \in V_h^3, & w \in V_h^2\,. \end{cases} \tag{23}$$

We represent this broken FEEC discretization with the following diagram

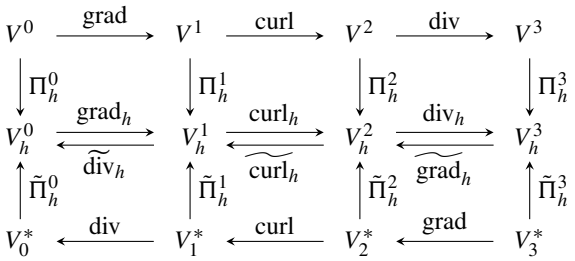

(24)

where Π_h^ℓ and $\tilde{\Pi}_h^\ell$ are projection operators that commute with the new primal and dual sequences. Here Π_h^ℓ are seen as unbounded operators with dense domains $U^\ell \subset V^\ell$. For the dual sequence the commuting projections $\tilde{\Pi}_h^\ell$ will be bounded in L^2: We postpone their description to the next sections.

We note that the presence of conforming projections P_h^ℓ in the differential operators (22) leads to larger kernels. Specifically, we have

$$\begin{cases} \ker \mathrm{grad}_h = \left(V_h^{0,c} \cap \ker \mathrm{grad}\right) \oplus \ker P_h^0 \\ \ker \mathrm{curl}_h = \left(V_h^{1,c} \cap \ker \mathrm{curl}\right) \oplus \ker P_h^1 \\ \ker \mathrm{div}_h = \left(V_h^{2,c} \cap \ker \mathrm{div}\right) \oplus \ker P_h^2 \end{cases}$$

where the projection kernels

$$\ker P_h^\ell = (I - P_h^\ell) V_h^\ell \tag{25}$$

correspond intuitively to "jump spaces" associated with the conforming projections. In [17, 19] these extended kernels motivated a modification of the discrete differential operators in order to retain exact sequences on contractible domains. Here we follow the approach of [23] where the jump spaces (25) are handled by stabilisation and filtering operators in the equations, through extended Hodge–Helmholtz decompositions.

2.4 Commuting Projections with Broken Degrees of Freedom

A practical approach for designing commuting projection operators $\Pi_h^{\ell,c}$ and Π_h^ℓ for the above diagrams is to define them via commuting degrees of freedom on the discrete Finite Element spaces. In the standard case of conforming spaces these are linear forms

$$\sigma_i^{\ell,c} : U^\ell \to \mathbb{R}, \quad i = 1, \ldots, N^{\ell,c} := \dim(V_h^{\ell,c})$$

defined on infinite-dimensional spaces $U^\ell \subset V^\ell$ satisfying $d^\ell U^\ell \subset U^{\ell+1}$, that are unisolvent in $V_h^{\ell,c}$ and commute with the differential operators in the sense that there exist coefficients $D_{i,j}^\ell$ such that

$$\sigma_i^{\ell+1,c}(d^\ell v) = \sum_{j=1}^{N^{\ell,c}} D_{i,j}^\ell \sigma_j^{\ell,c}(v) \quad \text{for } i = 1, \ldots N^{\ell+1,c}, \quad v \in U^\ell \tag{26}$$

where we have denoted again $d^0 = \mathrm{grad}$, $d^1 = \mathrm{curl}$ and $d^2 = \mathrm{div}$. Letting $\Lambda_i^{\ell,c}$ be the basis of $V_h^{\ell,c}$ characterized by the relations $\sigma_i^{\ell,c}(\Lambda_j^{\ell,c}) = \delta_{i,j}$ for $i, j = 1, \ldots N^{\ell,c}$, one verifies

indeed that the operators

$$\Pi_h^{\ell,c} : U^\ell \to V_h^{\ell,c}, \quad v \mapsto \sum_{i=1}^{N^{\ell,c}} \sigma_i^{\ell,c}(v)\Lambda_i^{\ell,c}$$

are projections satisfying the commuting property (10), see e.g. [24, Lemma 2] and in passing we note that D^ℓ is the matrix of d^ℓ in the bases just defined.

Here, we extend this approach as follows:

– *Broken degrees of freedom.* Each local space $V_h^\ell(\Omega_k)$, $k = 1, \dots, K$, is equipped with unisolvent degrees of freedom

$$\sigma_{k,\mu}^\ell : U^\ell(\Omega_k) \to \mathbb{R}, \quad \mu \in \mathcal{M}_h^\ell(\Omega_k) \tag{27}$$

defined on local spaces $U^\ell(\Omega_k) \subset V^\ell(\Omega_k)$ satisfying $d^\ell U^\ell(\Omega_k) \subset U^{\ell+1}(\Omega_k)$, with multi-index sets with cardinality $\#\mathcal{M}_h^\ell(\Omega_k) = \dim(V_h^\ell(\Omega_k))$. On the full domain we simply set

$$\sigma_{k,\mu}^\ell(v) := \sigma_{k,\mu}^\ell(v|_{\Omega_k}). \tag{28}$$

– *Broken basis functions.* To the above degrees of freedom we associate local basis functions $\Lambda_{k,\mu}^\ell \in V_h^\ell(\Omega_k)$ (extended by zero outside of their patch), characterized by the relations

$$\sigma_{k,\mu}^\ell(\Lambda_{k,\nu}^\ell) = \delta_{\mu,\nu} \quad \text{for} \quad \mu, \nu \in \mathcal{M}_h^\ell(\Omega_k).$$

– *Local commutation property.* A relation similar to (26) must hold on each patch Ω_k, i.e., there exist coefficients $D_{k,\mu,\nu}^\ell$ such that

$$\sigma_{k,\mu}^{\ell+1}(d^\ell v) = \sum_{\nu \in \mathcal{M}_h^\ell(\Omega_k)} D_{k,\mu,\nu}^\ell \sigma_{k,\nu}^\ell(v) \tag{29}$$

holds for all $\mu \in \mathcal{M}_h^{\ell+1}(\Omega_k)$ and all $v \in U^\ell(\Omega_k)$.

– *Inter-patch conformity*. The global projection on V_h^ℓ,

$$\Pi_h^\ell : v \mapsto \sum_{k=1}^K \Pi_{h,k}^\ell v \quad \text{with} \quad \Pi_{h,k}^\ell : v \mapsto \sum_{\mu \in \mathcal{M}_h^\ell(\Omega_k)} \sigma_{k,\mu}^\ell(v)\Lambda_{k,\mu}^\ell \tag{30}$$

must map smooth functions to conforming finite element fields, namely

$$\Pi_h^\ell U^\ell \subset V_h^{\ell,c} \quad \text{where} \quad U^\ell := \{v \in V^\ell : v|_{\Omega_k} \in U^\ell(\Omega_k),\ \forall k = 1, \dots K\}. \tag{31}$$

This setting guarantees that the commutation properties of the local projection operators extend to the global ones, since one has then

$$d^\ell P_h^\ell \Pi_h^\ell v = d^\ell \Pi_h^\ell v = \Pi_h^{\ell+1} d^\ell v, \quad v \in U^\ell,$$

and it yields simple expressions for the latter in the broken bases. We refer to Sect. 4 for a detailed construction of broken degrees of freedom that satisfy the above properties.

The dual projection operators (namely, the projection operators on the finite element spaces which commute with the differential operators from the dual sequences) can then be defined following the canonical approach of Campos-Pinto and Güçlü [23], as "filtered" L^2 projections

$$\tilde{\Pi}_h^\ell = (P_h^\ell)^* Q_{V_h^\ell} : L^2 \to V_h^\ell, \tag{32}$$

where $Q_{V_h^\ell}$ is now the L^2 projection on the broken space V_h^ℓ,

$$\langle \tilde{\Pi}_h^\ell v, w\rangle = \langle v, P_h^\ell w\rangle, \quad \forall v \in L^2,\ w \in V_h^\ell. \tag{33}$$

By definition of the dual differentials (23), these operators indeed commute with the dual part of the diagram (24), in the sense that

$$\tilde{\Pi}_h^0 \operatorname{div} = \widetilde{\operatorname{div}}_h \tilde{\Pi}_h^1, \quad \tilde{\Pi}_h^1 \operatorname{curl} = \widetilde{\operatorname{curl}}_h \tilde{\Pi}_h^2, \quad \tilde{\Pi}_h^2 \operatorname{grad} = \widetilde{\operatorname{grad}}_h \tilde{\Pi}_h^3 \tag{34}$$

hold on V_1^*, V_2^* and V_3^* respectively. We further observe that (32)–(33) defines projection operators on the subspaces of V_h^ℓ corresponding to the orthogonal complements of the "jump spaces" (25). Indeed, $(\tilde{\Pi}_h^\ell)^2 = \tilde{\Pi}_h^\ell$ holds with

$$\operatorname{Im}(\tilde{\Pi}_h^\ell) = \operatorname{Im}((P_h^\ell)^*) = (\ker P_h^\ell)^\perp = \{v \in V_h^\ell : \langle v, (I - P_h^\ell)w\rangle = 0,\ \forall w \in V_h^\ell\}.$$

2.5 Differential Operator Matrices in Primal and Dual Bases

Using broken degrees of freedom and basis functions as described in the previous section, we now derive practical representations for the operators involved in the diagram (24). To do so we first observe that the non-conforming differential operators $d_h^\ell := d^\ell P_h^\ell$ can be reformulated as $d_h^\ell = d_{\mathrm{pw}}^\ell P_h^\ell$ where $d_{\mathrm{pw}}^\ell : v \to \sum_{k=1}^K \mathbb{1}_{\Omega_k} d^\ell|_{\Omega_k} v$ is the patch-wise differential operator which coincides with d^ℓ on all v such that $d^\ell v \in L^2$. Using some implicit flattening $(k, \mu) \mapsto i \in \{1, \dots, N^\ell\}$ for the multi-indices, we represent these operators as matrices

$$(\mathbb{G})_{i,j} = \sigma_i^1(\operatorname{grad}_{\mathrm{pw}} \Lambda_j^0), \quad (\mathbb{C})_{i,j} = \sigma_i^2(\operatorname{curl}_{\mathrm{pw}} \Lambda_j^1), \quad (\mathbb{D})_{i,j} = \sigma_i^3(\operatorname{div}_{\mathrm{pw}} \Lambda_j^2) \tag{35}$$

of respective sizes $N^1 \times N^0$, $N^2 \times N^1$ and $N^3 \times N^2$. These matrices have a "patch-diagonal" structure, in the sense that they are block-diagonal, with blocks corresponding to the differential operators in each independent patch [namely, the matrices D_k^ℓ in (29)]. The matrices of the conforming projections, seen as endomorphisms in V_h^ℓ, are

$$(\mathbb{P}^\ell)_{i,j} = \sigma_i^\ell(P_h^\ell \Lambda_j^\ell), \quad i, j = 1, \dots, N^\ell. \tag{36}$$

In general $\mathbb{P}^\ell$ is not patch-diagonal, as it maps in the coefficient space of the conforming spaces $V_h^{\ell,c}$, where the global smoothness corresponds to some matching of the degrees of freedom across the interfaces.

With these elementary matrices we can build the operator matrices of the non-conforming differential operators d_h^ℓ: they read

$$\begin{aligned}\left(\mathbb{O}(d_h^\ell)\right)_{i,j} &:= \sigma_i^{\ell+1}\left(d_h^\ell \Lambda_j^\ell\right) = \sigma_i^{\ell+1}\left(d_{\mathrm{pw}}^\ell P_h^\ell \Lambda_j^\ell\right) = \sigma_i^{\ell+1}\left(d_{\mathrm{pw}}^\ell \sum_{k=1}^{N^\ell} \Lambda_k^\ell \sigma_k^\ell\left(P_h^\ell \Lambda_j^\ell\right)\right) \\ &= \sum_{k=1}^{N^\ell} \sigma_i^{\ell+1}\left(d_{\mathrm{pw}}^\ell \Lambda_k^\ell\right) \sigma_k^\ell\left(P_h^\ell \Lambda_j^\ell\right) = \sum_{k=1}^{N^\ell} \left({}^\ell\right)_{i,k} \left(\mathbb{P}^\ell\right)_{k,j} = \left({}^\ell\mathbb{P}^\ell\right)_{i,j},\end{aligned}$$

where we have denoted $(^{\ell})_{\ell} = (\mathbb{G}, \mathbb{C}, \mathbb{D})$ for brevity. Therefore,

$$\begin{cases} \mathbb{O}(\mathrm{grad}_h) & = \left(\sigma_i^1\left(\mathrm{grad}\, P_h^0\Lambda_j^0\right)\right)_{\substack{1\le i\le N^1\\ 1\le j\le N^0}} = \mathbb{G}\mathbb{P}^0, \\ \mathbb{O}(\mathrm{curl}_h) & = \left(\sigma_i^2\left(\mathrm{curl}\, P_h^1\Lambda_j^1\right)\right)_{\substack{1\le i\le N^2\\ 1\le j\le N^1}} = \mathbb{C}\mathbb{P}^1, \\ \mathbb{O}(\mathrm{div}_h) & = \left(\sigma_i^3\left(\mathrm{div}\, P_h^2\Lambda_j^2\right)\right)_{\substack{1\le i\le N^3\\ 1\le j\le N^2}} = \mathbb{D}\mathbb{P}^2. \end{cases} \tag{37}$$

A simple representation of the dual discrete operators (23) is obtained in the dual bases $\{\tilde\Lambda_i^{\ell} : i = 1, \dots, N^{\ell}\}$ of the broken spaces V_h^{ℓ}. These are characterized by the relations

$$\tilde\sigma_i^{\ell}(\tilde\Lambda_j^{\ell}) = \delta_{i,j}, \quad i, j = 1, \dots N^{\ell} \tag{38}$$

with dual degrees of freedom defined as

$$\tilde\sigma_i^{\ell}(v) := \langle v, \Lambda_i^{\ell}\rangle, \quad v \in L^2(\Omega), \tag{39}$$

where $\langle\cdot,\cdot\rangle$ denotes again the L^2 scalar product. It follows from (38) and (39) that the primal and dual bases are in L^2 duality, i.e. $\langle\Lambda_i^{\ell}, \tilde\Lambda_j^{\ell}\rangle = \delta_{i,j}$. The matrices of the dual differential operators in the dual bases read then

$$\begin{aligned} \left(\tilde{\mathbb{O}}(\tilde d_h^{3-\ell})\right)_{i,j} &:= \tilde\sigma_i^{\ell}\left(\tilde d_h^{3-\ell}\tilde\Lambda_j^{\ell+1}\right) = \langle \tilde d_h^{3-\ell}\tilde\Lambda_j^{\ell+1}, \Lambda_i^{\ell}\rangle = (-1)^{\ell+1}\langle\tilde\Lambda_j^{\ell+1}, d_h^{\ell}\Lambda_i^{\ell}\rangle \\ &= (-1)^{\ell+1}\left\langle\tilde\Lambda_j^{\ell+1}, \sum_{k=1}^{N^{\ell+1}}\Lambda_k^{\ell+1}\sigma_k^{\ell+1}\left(d_h^{\ell}\Lambda_i^{\ell}\right)\right\rangle \\ &= (-1)^{\ell+1}\sum_{k=1}^{N^{\ell+1}}\langle\tilde\Lambda_j^{\ell+1}, \Lambda_k^{\ell+1}\rangle\sigma_k^{\ell+1}\left(d_h^{\ell}\Lambda_i^{\ell}\right) \\ &= (-1)^{\ell+1}\sum_{k=1}^{N^{\ell+1}}\delta_{j,k}\left(\mathbb{D}^{\ell}\mathbb{P}^{\ell}\right)_{k,i} = (-1)^{\ell+1}\left(\mathbb{D}^{\ell}\mathbb{P}^{\ell}\right)_{j,i}, \end{aligned}$$

where again $(\mathbb{D}^{\ell})_{\ell} = (\mathbb{G}, \mathbb{C}, \mathbb{D})$ for brevity. Therefore,

$$\begin{cases} \tilde{\mathbb{O}}(\widetilde{\mathrm{div}}_h) & = \left(\tilde\sigma_i^0\left(\widetilde{\mathrm{div}}_h\tilde\Lambda_j^1\right)\right)_{\substack{1\le i\le N^0\\ 1\le j\le N^1}} = -(\mathbb{G}\mathbb{P}^0)^T, \\ \tilde{\mathbb{O}}(\widetilde{\mathrm{curl}}_h) & = \left(\tilde\sigma_i^1\left(\widetilde{\mathrm{curl}}_h\tilde\Lambda_j^2\right)\right)_{\substack{1\le i\le N^1\\ 1\le j\le N^2}} = (\mathbb{C}\mathbb{P}^1)^T, \\ \tilde{\mathbb{O}}(\widetilde{\mathrm{grad}}_h) & = \left(\tilde\sigma_i^2\left(\widetilde{\mathrm{grad}}_h\tilde\Lambda_j^3\right)\right)_{\substack{1\le i\le N^2\\ 1\le j\le N^3}} = -(\mathbb{D}\mathbb{P}^2)^T. \end{cases} \tag{40}$$

The change-of-basis matrices are described in the next section.

2.6 Primal-Dual Diagram in Matrix Form

Using the matrix form of the differential operators just described, we extend the broken FEEC diagram (24) as follows:

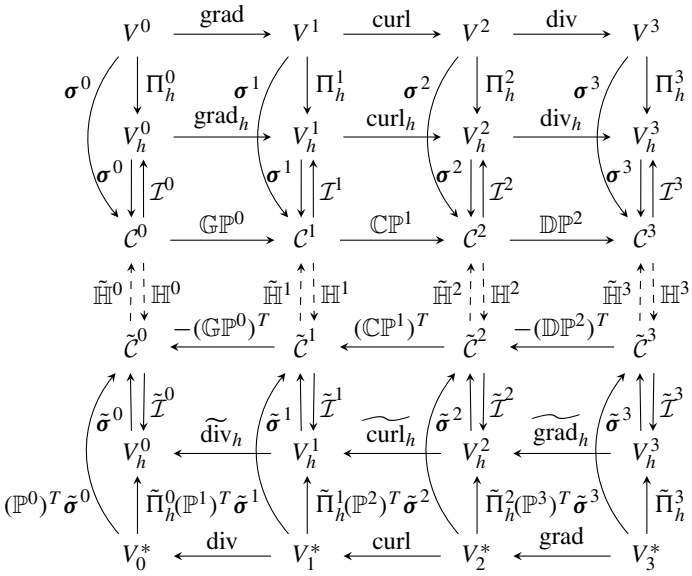

(41)

Here $\mathcal{C}^\ell$ and $\tilde{\mathcal{C}}^\ell$ are the spaces of scalar coefficients associated with the primal and dual basis functions described in the previous Section. Both are of the form $\mathbb{R}^{N^\ell}$ with $N^\ell = \dim(V_h^\ell)$, but we use a different notation to emphasize the different roles played by the coefficient vectors. The interpolation operators $\mathcal{I}^\ell : \mathcal{C}^\ell \to V_h^\ell$ and $\tilde{\mathcal{I}}^\ell : \tilde{\mathcal{C}}^\ell \to V_h^\ell$, which read

$$\mathcal{I}^\ell : \mathbf{c} \mapsto \sum_{i=1}^{N^\ell} c_i \Lambda_i^\ell \quad \text{and} \quad \tilde{\mathcal{I}}^\ell : \tilde{\mathbf{c}} \mapsto \sum_{i=1}^{N^\ell} \tilde{c}_i \tilde{\Lambda}_i^\ell \,, \tag{42}$$

are the right-inverses of the respective degrees of freedom $\boldsymbol{\sigma}^\ell$ and $\tilde{\boldsymbol{\sigma}}^\ell$, and also their left-inverses on V_h^ℓ.

The matrices $\mathbb{H}^\ell$ and $\tilde{\mathbb{H}}^\ell$ are change-of-basis matrices which allow us to go from one sequence to the other, in the sense that $\mathcal{I}^\ell = \tilde{\mathcal{I}}^\ell \mathbb{H}^\ell$ and $\tilde{\mathcal{I}}^\ell = \mathcal{I}^\ell \tilde{\mathbb{H}}^\ell$: they correspond to discrete Hodge operators [34]. Here it follows from the duality construction (38)–(39) that they are given by the mass matrices and their inverses,

$$\mathbb{H}^\ell = (\tilde{\mathbb{H}}^\ell)^{-1} = \mathbb{M}^\ell \quad \text{where} \quad (\mathbb{M}^\ell)_{i,j} = \langle \Lambda_i^\ell, \Lambda_j^\ell \rangle. \tag{43}$$

In our framework, the Hodge matrices have a patch-diagonal structure due to the local support of the broken basis functions. In particular, the dual basis functions are also supported on a single patch.

The remaining operators are the primal and dual commuting projections, respectively defined by (30) and (32)–(33), expressed in terms of primal and dual coefficients. Using the interpolation operators (42) we may write them as

$$\Pi^\ell = \mathcal{I}^\ell \boldsymbol{\sigma}^\ell \quad \text{on } U^\ell \subset V^\ell \quad \text{and} \quad \tilde{\Pi}^\ell = \tilde{\mathcal{I}}^\ell (\mathbb{P}^\ell)^T \tilde{\boldsymbol{\sigma}}^\ell \quad \text{on } V_\ell^* \,. \tag{44}$$

Finally we remind that here the commutation of the primal (upper) diagram follows from the assumed properties of the primal degrees of freedom (27)–(31), while the commutation of the dual (lower) diagram follows from the weak definition of the dual differential operators.

Remark 2 (*Conforming case*) The conforming FEEC diagram (15) (corresponding, e.g., to a single patch discretization) may be extended in the same way as the broken FEEC one (24). Apart from the differences between the discrete differential operators and commuting projection operators already visible in (15) and (24), the resulting 6-rows diagram would be formally the same as (41), but no conforming projection matrices would be involved any longer.

Remark 3 (*Change of basis*) It may happen that the basis functions Λ_i^ℓ associated with the commuting degrees of freedom σ_i^ℓ are not the most convenient ones when it comes to actually implement the discrete operators. In such cases a few changes are to be done to the diagram (41), such as the ones described in Sect. 4.2 for local spline spaces.

2.7 Discrete Hodge–Laplace and Jump Stabilization Operators

In addition to the first order differential operators, an interesting feature of the diagram (41) is to provide us with natural discretizations for the Hodge–Laplace operators. On the space V^0 this is the standard Laplace operator, $\mathcal{L}^0 = -\Delta$, which is discretized as

$$\mathcal{L}_h^0 := -\widetilde{\mathrm{div}}_h \,\mathrm{grad}_h : V_h^0 \to V_h^0 \tag{45}$$

with an operator matrix in the primal basis that reads

$$\mathbb{L}^0 = \tilde{\mathbb{H}}^0 (\mathbb{G}\mathbb{P}^0)^T \mathbb{H}^1 \mathbb{G}\mathbb{P}^0 \,. \tag{46}$$

As for the Hodge–Laplace operator for 1-forms, $\mathcal{L}^1 = \mathrm{curl}\,\mathrm{curl} - \mathrm{grad}\,\mathrm{div}$, its discretization is

$$\mathcal{L}_h^1 := \widetilde{\mathrm{curl}}_h \,\mathrm{curl}_h - \mathrm{grad}_h \,\widetilde{\mathrm{div}}_h : V_h^1 \to V_h^1 \tag{47}$$

with an operator matrix (again in the primal basis)

$$\mathbb{L}^1 = \tilde{\mathbb{H}}^1 (\mathbb{C}\mathbb{P}^1)^T \mathbb{H}^2 \mathbb{C}\mathbb{P}^1 + \mathbb{G}\mathbb{P}^0 \tilde{\mathbb{H}}^0 (\mathbb{G}\mathbb{P}^0)^T \mathbb{H}^1. \tag{48}$$

The Hodge–Laplace operators for 2 and 3-forms are discretized similarly.

As discussed in Sect. 2.2, a key asset of FEEC discretizations is their ability to preserve the exact dimension of the harmonic forms, defined here as the kernel of the Hodge–Laplace operators. In our broken FEEC framework this property is a priori not preserved by the non-conforming operators due to the extended kernels of the conforming projection operators, but it is for the *stabilized* operators $\mathcal{L}_{h,\alpha}^\ell = \mathcal{L}_h^\ell + \alpha S_h^\ell$ where

$$S_h^\ell := (I - P_h^\ell)^* (I - P_h^\ell) \tag{49}$$

is the symmetrized projection operator on the jump space (25), and α is a stabilization parameter. Indeed, it was shown in [23] that the kernel of $\mathcal{L}_{h,\alpha}^\ell$ coincides with that of the conforming discrete Hodge–Laplacian, for any positive value of $\alpha > 0$. Finally we note that the corresponding stabilization matrix is readily derived from the operators in the diagram. It reads

$$\mathbb{S}^\ell = \tilde{\mathbb{H}}^\ell (\mathbb{I} - \mathbb{P}^\ell)^T \mathbb{H}^\ell (\mathbb{I} - \mathbb{P}^\ell). \tag{50}$$

3 Broken FEEC Approximations of Electromagnetic Problems

In this section we propose broken FEEC approximations for several problems arising in electromagnetics, and we state a priori results for the solutions. Let us begin by listing the main differences between broken and conforming FEEC approximations:

- Differential and projection operators from the commuting diagram (41) apply to broken (fully discontinuous) spaces and involve conforming projection operators which in practice couple interface degrees of freedom and can be applied matrix free.
- For problems that involve solving a system (e.g., Poisson, time-harmonic Maxwell and Magnetostatic equations), symmetric stabilization operators must be added to make the system non singular. This is not needed for the time-dependent Maxwell equations.
- For the former problems, our stabilized broken FEEC schemes yield the same solution as the corresponding conforming FEEC method. This is not the case for the time-dependent Maxwell equations.
- For eigenvalue problems several formulations can be used (with or without stabilization terms), depending on whether zero or positive eigenmodes are searched for.

For the sake of completeness we will provide several formulations (all equivalent) for the discrete problems: one in operator form, one in weak form and one in matrix form, using the primal and dual bases introduced in Sect. 2.4. As pointed out in Remark 3, practical implementation may be more efficient with other basis functions. In this case the matrices need to be changed, as will be described in Sect. 4.2 below.

Throughout this section we will mostly work with the homogeneous spaces V^ℓ corresponding to (2). In the few cases where we will need the inhomogeneous spaces, we shall use a specific notation $\bar{V}^\ell$ for the spaces in (4), for the sake of clarity.

3.1 Poisson's Equation

For the Poisson problem with homogeneous Dirichlet boundary conditions: given $f \in L^2(\Omega)$, find $\phi \in V^0 = H_0^1(\Omega)$ such that

$$-\Delta\phi = f, \tag{51}$$

we combine the stabilized broken FEEC discretization described in Sect. 2.7 for the Laplace operator, and a dual commuting projection (32)–(33) for the source. The resulting problem reads: Find $\phi_h \in V_h^0$ such that

$$(\mathcal{L}_h^0 + \alpha S_h^0)\phi_h = \tilde{\Pi}_h^0 f \tag{52}$$

and it enjoys the following property.

Proposition 1 *For all $\alpha \neq 0$, Eq. (52) admits a unique solution ϕ_h which belongs to the conforming space $V_h^{0,c} = V_h^0 \cap H_0^1(\Omega)$ and solves the conforming Poisson problem*

$$\langle \operatorname{grad} \varphi^c, \operatorname{grad} \phi_h \rangle = \langle \varphi^c, f \rangle \quad \forall \varphi^c \in V_h^{0,c}. \tag{53}$$

In particular, ϕ_h is independent of both α and the specific projection P_h^0.

Proof By definition of the different operators, (52) reads

$$\big(-\widetilde{\operatorname{div}}_h \operatorname{grad}_h + \alpha (I - P_h^0)^*(I - P_h^0)\big)\phi_h = \tilde{\Pi}_h^0 f \tag{54}$$

which may be reformulated using test functions $\varphi \in V_h^0$, as

$$\langle \text{grad}\, P_h^0\varphi, \text{grad}\, P_h^0\phi_h\rangle + \alpha\langle (I - P_h^0)\varphi, (I - P_h^0)\phi_h\rangle = \langle P_h^0\varphi, f\rangle. \tag{55}$$

Taking $\varphi = (I - P_h^0)\phi_h$ yields $\phi_h = P_h^0\phi_h \in V_h^{0,c}$ as long as $\alpha \neq 0$, and (53) follows by considering test functions φ in the conforming subspace $V_h^{0,c}$. □

The matrix formulation of (52) is easily derived by using the diagram (41), writing the equation in the dual basis in order to obtain symmetric matrices as is usual with the Poisson problem. Denoting by $\boldsymbol{\phi} = \boldsymbol{\sigma}^0(\phi_h)$ the coefficient vector of ϕ_h in the primal basis, we thus find

$$\mathbb{A}^0\boldsymbol{\phi} = (\mathbb{P}^0)^T\tilde{\boldsymbol{\sigma}}^0(f) \tag{56}$$

with a stabilized stiffness matrix

$$\mathbb{A}^0 = \mathbb{H}^0(\mathbb{L}^0 + \alpha\mathbb{S}^0) = (\mathbb{G}\mathbb{P}^0)^T\mathbb{H}^1\mathbb{G}\mathbb{P}^0 + \alpha(\mathbb{I} - \mathbb{P}^0)^T\mathbb{H}^0(\mathbb{I} - \mathbb{P}^0). \tag{57}$$

3.2 Time-Harmonic Maxwell's Equation

The time-harmonic Maxwell equation with homogeneous boundary conditions reads: given $\omega \in \mathbb{R}$ and $J \in L^2(\Omega)$, find $u \in H_0(\text{curl}; \Omega)$ such that

$$-\omega^2 u + \text{curl}\,\text{curl}\, u = J. \tag{58}$$

Here the (complex) electric field corresponds to $E(t, x) = i\omega\, u(x)e^{-i\omega t}$. When ω^2 is not an eigenvalue of the curl curl operator, Eq. (58) is well-posed: see e.g. [3, Theorem 8.3.3]. For this problem we propose a stabilized broken FEEC discretization where $u_h \in V_h^1$ solves

$$(-\omega^2(P_h^1)^* P_h^1 + \widetilde{\text{curl}}_h\, \text{curl}_h + \alpha S_h^1)u_h = \tilde{\Pi}_h^1 J, \tag{59}$$

with a parameter $\alpha \in \mathbb{R}$. We remind that $S_h^1 := (1 - P_h^1)^*(1 - P_h^1)$ is the jump stabilization operator, according to (49) and (25) for $\ell = 1$. With test functions $v \in V_h^1$, the discrete problem (59) writes

$$-\omega^2\langle P_h^1 v, P_h^1 u_h\rangle + \langle \text{curl}\, P_h^1 v, \text{curl}\, P_h^1 u_h\rangle + \alpha\langle (I - P_h^1)v, (I - P_h^1)u_h\rangle = \langle P_h^1 v, J\rangle. \tag{60}$$

Here, we note that the zeroth-order term is filtered by the symmetric operator $(P_h^1)^* P_h^1$: this allows us to obtain a conforming solution in the broken space.

Proposition 2 *Let $\alpha \neq 0$, and ω such that ω^2 is not an eigenvalue of the* conforming *discrete* $\widetilde{\text{curl}}_h^c\, \text{curl}_h^c$ *operator defined in* (12)–(14). *Then Eq.* (59) *admits a unique solution u_h which belongs to the conforming space $V_h^{1,c} = V_h^1 \cap H_0(\text{curl}; \Omega)$, and solves the conforming FEEC Maxwell problem*

$$-\omega^2\langle v^c, u_h\rangle + \langle \text{curl}\, v^c, \text{curl}\, u_h\rangle = \langle v^c, J\rangle, \quad \forall v^c \in V_h^{1,c}. \tag{61}$$

In particular, u_h is independent of both α and the specific projection P_h^1.

Proof Taking $v = (I - P_h^1)u_h$ in (60) gives $u_h = P_h^1 u_h \in V_h^{1,c}$ as long as $\alpha \neq 0$, and (61) follows by considering test functions $v = v^c$ in $V_h^{1,c}$. Existence and uniqueness follow from the assumption that ω is not an eigenvalue of the conforming curl curl operator. □

The matrix form of (59) is easily derived from diagram (41). It reads

$$\mathbb{A}^1 \mathbf{u} = (\mathbb{P}^1)^T \tilde{\boldsymbol{\sigma}}^1(J) \tag{62}$$

where $\mathbf{u} := \boldsymbol{\sigma}^1(u_h)$ is the (column) vector containing the coefficients of u_h in the primal basis of V_h^1, and $\mathbb{A}^1$ is the resulting stabilized stiffness matrix,

$$\mathbb{A}^1 = (\mathbb{P}^1)^T(-\omega^2\mathbb{H}^1 + \mathbb{C}^T\mathbb{H}^2\mathbb{C})\mathbb{P}^1 + \alpha(\mathbb{I} - \mathbb{P}^1)^T\mathbb{H}^1(\mathbb{I} - \mathbb{P}^1). \tag{63}$$

3.3 Lifting of Boundary Conditions

In the case of inhomogeneous boundary conditions a standard approach is to introduce a lifted solution and solve the modified problem in the homogeneous spaces. This approach applies seamlessly to broken FEEC approximations. For a Poisson equation of the form

$$\begin{cases} -\Delta\phi = f & \text{in } \Omega \\ \phi = g & \text{on } \partial\Omega \end{cases} \tag{64}$$

this corresponds to introducing $\phi_g \in H^1(\Omega)$ such that $\phi_g = g$ on $\partial\Omega$, and characterizing the solution as $\phi = \phi_g + \phi_0$, where $\phi_0 \in V^0 = H_0^1(\Omega)$ solves (51) with a modified source, namely

$$-\Delta\phi_0 = f + \Delta\phi_g.$$

For an inhomogeneous Maxwell equation of the form

$$\begin{cases} -\omega^2 u + \operatorname{curl}\operatorname{curl} u = J & \text{in } \Omega \\ n \times u = g & \text{on } \partial\Omega \end{cases} \tag{65}$$

we introduce $u_g \in H(\operatorname{curl};\Omega)$ such that $n \times u_g = g$ on $\partial\Omega$, and characterize the solution as $u = u_g + u_0$, where $u_0 \in H_0(\operatorname{curl};\Omega)$ solves (58) with a modified source, namely

$$-\omega^2 u_0 + \operatorname{curl}\operatorname{curl} u_0 = J + (\omega^2 - \operatorname{curl}\operatorname{curl})u_g. \tag{66}$$

The lifting approach can be applied in broken FEEC methods by combining the discretizations of the homogeneous and inhomogeneous sequences (2) and (4), which amounts to combining different conforming projections. For clarity we denote in this section the respective homogeneous and inhomogeneous spaces by V^ℓ and $\bar{V}^\ell$. At the discrete level the broken spaces V_h^ℓ have no boundary conditions, so that the distinction only appears in the conforming projections to the spaces $V_h^{\ell,c} = V_h^\ell \cap V^\ell$ and $\bar{V}_h^{\ell,c} = V_h^\ell \cap \bar{V}^\ell$, which we naturally denote by P_h^ℓ and $\bar{P}_h^\ell$ respectively. In practice the latter projects on the inhomogeneous conforming spaces, while the former further sets the boundary degrees of freedom to zero.

For the Poisson equation where $V^0 = H_0^1(\Omega)$ and $\bar{V}^0 = H^1(\Omega)$, we first compute $\phi_{g,h} \in V_h^0$ that approximates g on $\partial\Omega$, and then we compute the homogeneous part of the solution, $\phi_{0,h} := \phi_h - \phi_{g,h} \in V_h^0$, by solving the homogeneous CONGA problem with modified source

$$\begin{aligned} &\langle \operatorname{grad} P_h^0\varphi, \operatorname{grad} P_h^0\phi_{0,h}\rangle + \alpha\langle (I - P_h^0)\varphi, (I - P_h^0)\phi_{0,h}\rangle \\ &\quad = \langle P_h^0\varphi, f\rangle - \langle \operatorname{grad} P_h^0\varphi, \operatorname{grad} \bar{P}_h^0\phi_{g,h}\rangle \end{aligned} \tag{67}$$

for all $\varphi \in V_h^0$, which also reads in matrix form

$$\mathbb{A}^0\boldsymbol{\phi}_0 = (\mathbb{P}^0)^T\left(\tilde{\boldsymbol{\sigma}}^0(f) - \mathbb{G}^T\mathbb{H}^1\mathbb{G}\bar{\mathbb{P}}^0\boldsymbol{\phi}_g\right) \tag{68}$$

where $\mathbb{A}^0$ is the stabilized stiffness matrix (57), $\bar{\mathbb{P}}^0$ is the matrix of the inhomogeneous projection $\bar{P}_h^0$, and the coefficient vectors involve the broken degrees of freedom $\boldsymbol{\phi}_0 = \boldsymbol{\sigma}^0(\phi_{0,h})$, $\boldsymbol{\phi}_g = \boldsymbol{\sigma}^0(\phi_{g,h})$ in the full broken space V_h^0.

For the Maxwell equation where $V^1 = H_0(\mathrm{curl};\Omega)$ and $\bar{V}^1 = H(\mathrm{curl};\Omega)$, the method consists of first computing $u_{g,h} \in V_h^1$ such that $n \times u_{g,h}$ approximates g on $\partial\Omega$, and then characterizing the homogeneous part of the solution, $u_{0,h} := u_h - u_{g,h} \in V_h^1$, by

$$\begin{aligned} &-\omega^2\langle P_h^1 v, P_h^1 u_{0,h}\rangle + \langle \mathrm{curl}\, P_h^1 v, \mathrm{curl}\, P_h^1 u_{0,h}\rangle + \alpha\langle (I-P_h^1)v, (I-P_h^1)u_{0,h}\rangle \\ &\quad = \langle P_h^1 v, J\rangle + \omega^2\langle P_h^1 v, \bar{P}_h^1 u_{g,h}\rangle - \langle \mathrm{curl}\, P_h^1 v, \mathrm{curl}\, \bar{P}_h^1 u_{g,h}\rangle \end{aligned} \tag{69}$$

for all $v \in V_h^1$. In matrix terms, this reads

$$\mathbb{A}^1 \mathbf{u}_0 = (\mathbb{P}^1)^T \left(\tilde{\boldsymbol{\sigma}}^1(J) + (\omega^2 \mathbb{H}^1 - \mathbb{C}^T \mathbb{H}^2 \mathbb{C}) \bar{\mathbb{P}}^1 \mathbf{u}_g \right) \tag{70}$$

where $\mathbb{A}^1$ is the stabilized stiffness matrix (63), $\bar{\mathbb{P}}^1$ is the matrix of the inhomogeneous projection $\bar{P}_h^1$, and the coefficient vectors involve the broken degrees of freedom $\mathbf{u}_0 = \boldsymbol{\sigma}^1(u_{0,h})$, $\mathbf{u}_g = \boldsymbol{\sigma}^1(u_{g,h})$ in the full broken space V_h^1.

Proposition 3 *Let α and ω be as in Proposition 2. Then (69) admits a unique solution $u_{0,h}$ which belongs to the conforming space $V_h^{1,c} = V_h^1 \cap H_0(\mathrm{curl};\Omega)$. The projection of the full solution in $\bar{V}_h^{1,c} = V_h^1 \cap H(\mathrm{curl};\Omega)$, $u_h^c := \bar{P}_h^1 u_h$, approximates the boundary condition, $n \times u_h^c \approx g$ on $\partial\Omega$, and it solves the discrete conforming Maxwell equation inside Ω, in the sense that*

$$-\omega^2\langle v^c, u_h^c\rangle + \langle \mathrm{curl}\, v^c, \mathrm{curl}\, u_h^c\rangle = \langle v^c, J\rangle, \quad \forall v^c \in V_h^{1,c}. \tag{71}$$

In particular, u_h^c is independent of both α and P_h^1. Moreover if the lifted boundary condition $u_{g,h}$ is chosen in $\bar{V}_h^{1,c}$, then $u_h = u_h^c$.

Proof The conformity and unicity of $u_{0,h}$ can be shown with the same arguments as in Proposition 2. This shows that $u_h^c = u_{0,h} + \bar{P}_h^1 u_{g,h}$ and that the tangential trace of u_h^c coincides with that of $\bar{P}_h^1 u_{g,h}$ on the boundary, which itself should coincide with that of $u_{g,h}$ as there are no conformity constraints there for the inhomogeneous space $\bar{V}^1 = H(\mathrm{curl};\Omega)$. Equation (71) and the additional observations follow easily. □

3.4 Eigenvalue Problems

Broken FEEC approximations to Hodge–Laplace eigenvalue problems of the form

$$\mathcal{L}^\ell u = \lambda u \tag{72}$$

are readily derived using the discrete operators presented in Sect. 2.7. For a general stabilization parameter $\alpha \geq 0$, they take the form:

$$(\mathcal{L}_h^\ell + \alpha S_h^\ell) u_h = \lambda_h u_h \tag{73}$$

with $u_h \in V_h^\ell \setminus \{0\}$. Their convergence can be established under the assumption of a strong stabilization regime and of moment-preserving properties for the conforming projections, see [23]. There it has also been shown that for arbitrary positive penalizations $\alpha > 0$, the zero eigenmodes coincide with their conforming counterparts, namely the conforming harmonic forms,

$$\ker(\mathcal{L}_h^\ell + \alpha S_h^\ell) = \ker \mathcal{L}_h^{\ell,c} = \mathcal{H}_h^\ell$$

see (17)–(18).

For the first space $V^0 = H_0^1(\Omega)$ the corresponding operator is the standard Laplace operator $\mathcal{L}^0 = -\Delta$ and its broken FEEC discretization reads: Find $\lambda_h \in \mathbb{R}$ and $\phi_h \in V_h^0 \backslash \{0\}$ such that

$$(\mathcal{L}_h^0 + \alpha S_h^0)\phi_h = \lambda_h \phi_h \tag{74}$$

where $\mathcal{L}_h^0$ and S_h^0 are given by (45) and (49), with stabilization parameter α. For $V^1 = H_0(\mathrm{curl};\Omega)$ the Hodge–Laplace operator is $\mathcal{L}^1 = \mathrm{curl}\,\mathrm{curl} - \mathrm{grad}\,\mathrm{div}$ and its discretization reads: Find $\lambda_h \in \mathbb{R}$ and $u_h \in V_h^1 \backslash \{0\}$ such that

$$(\mathcal{L}_h^1 + \alpha S_h^1)u_h = \lambda_h u_h \tag{75}$$

where $\mathcal{L}_h^1 = \widetilde{\mathrm{curl}}_h \,\mathrm{curl}_h - \mathrm{grad}_h \,\widetilde{\mathrm{div}}_h$, see (47), and S_h^1 is given again by (49). Eigenvalue problems in V_h^2 and V_h^3 are discretized in a similar fashion.

Another important eigenvalue problem is that of the curl-curl operator, for which one could simply adapt the broken FEEC discretization (75) used for the Hodge–Laplace operator, by dropping the term $(-\mathrm{grad}_h \,\widetilde{\mathrm{div}}_h)$. By testing such an equality with $v \in \mathrm{grad}\, P_h^0 V_h^0$ we see that the non-zero eigenmodes satisfy $\widetilde{\mathrm{div}}_h u_h = 0$, hence they are also eigenmodes of (75) and their convergence follows from the results mentionned above in the case of strong penalization regimes. In the unpenalized case ($\alpha = 0$) their convergence was also established, as shown in [18].

The main drawback of the approach just described is that the computed eigenvalues do not coincide with those of the conforming operator $\widetilde{\mathrm{curl}}_h^c \,\mathrm{curl}_h^c$, but only approximate them. (We recall that the knowledge of the eigenvalues of $\widetilde{\mathrm{curl}}_h^c \,\mathrm{curl}_h^c$ is needed in order to verify the hypotheses of Proposition 2 for the source problem: ω^2 should not concide with one of them.) To overcome this difficulty we propose a novel broken FEEC discretization, which consists of the generalized eigenvalue problem

$$\widetilde{\mathrm{curl}}_h \,\mathrm{curl}_h\, u_h = \lambda_h \left[(P_h^1)^* P_h^1 + (I - P_h^1)^*(I - P_h^1)\right] u_h. \tag{76}$$

With test functions $v \in V_h^1$, the discrete problem (76) writes

$$\langle \mathrm{curl}\, P_h^1 v, \mathrm{curl}\, P_h^1 u_h\rangle = \lambda_h \left[\langle P_h^1 v, P_h^1 u_n\rangle + \langle (1 - P_h^1)v, (1 - P_h^1)u_h\rangle\right] \tag{77}$$

and its matrix formulation is provided below.

Proposition 4 *For $\lambda_h \neq 0$, the (generalized) CONGA eigenvalue problem (76) has the same solutions as the conforming eigenproblem*

$$\widetilde{\mathrm{curl}}_h^c \,\mathrm{curl}_h^c\, u_h = \lambda_h u_h, \quad \text{with } u_h \in V_h^{1,c}. \tag{78}$$

For $\lambda_h = 0$, the corresponding eigenspace is

$$\ker\left(\widetilde{\mathrm{curl}}_h \,\mathrm{curl}_h\right) = \left(\mathrm{grad}\, V_h^{0,c} \overset{\perp}{\oplus} \mathcal{H}_h^1\right) \oplus (I - P_h^1)V_h^1. \tag{79}$$

Proof For $\lambda_h \neq 0$ we take $v = (I - P_h^1)u_h$ in (77), and find that $u_h = P_h^1 u_h \in V_h^{1,c}$. Hence we can restrict the test space to functions $v = P_h^1 v \in V_h^{1,c}$, and obtain the conforming eigenproblem $\langle \mathrm{curl}\, v, \mathrm{curl}\, u_h\rangle = \lambda_h \langle v, u_h\rangle$. Conversely, we verify that if $u_h \in V_h^{1,c}$ solves (78) then it also solves (77) for all $v \in V_h^1$. The relationship (79) between the null spaces

follows from the equalities $\ker\left(\widetilde{\text{curl}_h}\ \text{curl}_h\right) = \ker(\text{curl}_h)$, $\ker\left(\widetilde{\text{curl}_h^c}\ \text{curl}_h^c\right) = \ker(\text{curl}_h^c) = \text{grad}\, V_h^{0,c} \overset{\perp}{\oplus} \mathcal{H}_h^1$ and

$$\ker(\text{curl}_h) = \ker(\text{curl}_h^c) \oplus (I - P_h^1)V_h^1$$

which was observed in, e.g., [18]. □

These eigenvalue problems may be expressed in symmetric matrix form by expressing the eigenmodes in the primal bases and the equations in the dual bases, as we did for the Poisson and Maxwell equations in Sects. 3.1 and 3.2. For the Poisson eigenvalue problem (74) we obtain

$$\mathbb{A}^0 \boldsymbol{\phi} = \lambda_h \mathbb{H}^0 \boldsymbol{\phi} \tag{80}$$

with $\mathbb{A}^0 = \mathbb{H}^0(\mathbb{L}^0 + \alpha \mathbb{S}^0) = (\mathbb{G}\mathbb{P}^0)^T \mathbb{H}^1 \mathbb{G}\mathbb{P}^0 + \alpha(\mathbb{I} - \mathbb{P}^0)^T \mathbb{H}^0(\mathbb{I} - \mathbb{P}^0)$ as in (57). Similarly we can write the Hodge–Laplace eigenvalue problem (75) as

$$\mathbb{A}^1 \mathbf{u} = \lambda_h \mathbb{H}^1 \mathbf{u} \tag{81}$$

with matrix

$$\mathbb{A}^1 = (\mathbb{C}\mathbb{P}^1)^T \mathbb{H}^2 \mathbb{C}\mathbb{P}^1 + \mathbb{H}^1 \mathbb{G}\mathbb{P}^0 \tilde{\mathbb{H}}^0 (\mathbb{G}\mathbb{P}^0)^T \mathbb{H}^1 + \alpha(\mathbb{I} - \mathbb{P}^1)^T \mathbb{H}^1 (\mathbb{I} - \mathbb{P}^1),$$

and the curl-curl eigenvalue problem (76) as

$$(\mathbb{C}\mathbb{P}^1)^T \mathbb{H}^2 \mathbb{C}\mathbb{P}^1 \mathbf{u} = \lambda_h \left[(\mathbb{P}^1)^T \mathbb{H}^1 \mathbb{P}^1 + (\mathbb{I} - \mathbb{P}^1)^T \mathbb{H}^1 (\mathbb{I} - \mathbb{P}^1) \right] \mathbf{u}. \tag{82}$$

3.5 Magnetostatic Problems with Harmonic Constraints

We next consider a magnetostatic problem of the form

$$\begin{cases} \text{div}\, B = 0 \\ \text{curl}\, B = J \end{cases} \tag{83}$$

posed for a current $J \in L^2(\Omega)$. Unlike the Poisson and Maxwell source problems above, this problem requires an additional constraint in non-contractible domains. Indeed it can only be well-posed if $\ker \text{curl} \cap \ker \text{div} = \{0\}$, i.e., if the harmonic forms are trivial. To formulate this more precisely we need to take into account particular boundary conditions.

3.5.1 Magnetostatic Problem with Pseudo-Vacuum Boundary Condition

We first consider a boundary condition of the form $n \times B = 0$, which is sometimes used to model pseudo-vacuum boundaries [39]. A mixed formulation is then: Find $B \in H_0(\text{curl}; \Omega)$ and $p \in H_0^1(\Omega)$ such that

$$\begin{cases} \langle \text{grad}\, q, B \rangle = 0 & \forall q \in H_0^1(\Omega) \\ \langle v, \text{grad}\, p \rangle + \langle \text{curl}\, v, \text{curl}\, B \rangle = \langle \text{curl}\, v, J \rangle & \forall v \in H_0(\text{curl}; \Omega) \end{cases} \tag{84}$$

see e.g. [28]. Here the auxiliary unknown p is a Lagrange multiplier for the divergence constraint written in weak form.

The well-posedness of (84) is related to the space of harmonic 1-forms $\mathcal{H}^1$, defined as the kernel of the Hodge–Laplace operator (6) in the homogeneous sequence, i.e.,

$$\mathcal{H}^1 = \ker \mathcal{L}^1 = \{v \in H_0(\mathrm{curl};\Omega) : \ \mathrm{curl}\, v = \mathrm{div}\, v = 0\}. \tag{85}$$

As discussed in [2], $\mathcal{H}^1 = \mathcal{H}^1(\Omega)$ is isomorphic to a de Rham cohomology group and its dimension corresponds to a Betti number of the domain Ω. With homogeneous, resp. inhomogeneous boundary conditions its dimension is $b_2(\Omega)$ the number of cavities, resp. $b_1(\Omega)$ the number of handles in Ω. Thus in a contractible domain we have $\mathcal{H}^1 = \{0\}$ and the problem is well posed, but in general $\mathcal{H}^1$ may not be trivial. Additional constraints must then be imposed on the solution, such as $B \in (\mathcal{H}^1)^\perp$, which can be associated with an additional Lagrange multiplier $z \in \mathcal{H}^1$. The constrained problem then consists of finding $B \in H_0(\mathrm{curl};\Omega)$, $p \in H_0^1(\Omega)$ and $z \in \mathcal{H}^1$, such that

$$\begin{cases} \langle \mathrm{grad}\, q, B\rangle = 0 & \forall q \in H_0^1(\Omega) \\ \langle v, \mathrm{grad}\, p\rangle + \langle \mathrm{curl}\, v, \mathrm{curl}\, B\rangle + \langle v, z\rangle = \langle \mathrm{curl}\, v, J\rangle & \forall v \in H_0(\mathrm{curl};\Omega) \\ \langle w, B\rangle = 0 & \forall w \in \mathcal{H}^1. \end{cases} \tag{86}$$

In our broken FEEC framework this problem is discretized as: find $p_h \in V_h^0$, $B_h \in V_h^1$ and $z_h \in \mathcal{H}_h^1$, such that

$$\begin{cases} \alpha^0 \langle (I - P_h^0)q, (I - P_h^0)p_h\rangle + \langle \mathrm{grad}\, P_h^0 q, B_h\rangle = 0 \\ \langle v, \mathrm{grad}\, P_h^0 p_h\rangle + \langle \mathrm{curl}\, P_h^1 v, \mathrm{curl}\, P_h^1 B_h\rangle \\ \quad + \alpha^1 \langle (I - P_h^1)v, (I - P_h^1)B_h\rangle + \langle v, z_h\rangle = \langle \mathrm{curl}\, P_h^1 v, J\rangle \\ \langle w, B_h\rangle = 0 \end{cases} \tag{87}$$

for all $q \in V_h^0$, $v \in V_h^1$ and $w \in \mathcal{H}_h^1$. Here, $\alpha^\ell \in \mathbb{R}$ are stabilization parameters for the jump terms in V_h^0 and V_h^1, and $\mathcal{H}_h^1 = \ker(\mathcal{L}_h^1 + \alpha^1 S_h^1)$ may be computed as the kernel of the stabilized discrete Hodge–Laplace operator (47). As discussed above it coincides with that of the conforming Hodge–Laplace operator, hence

$$\mathcal{H}_h^1 = \{v \in V_h^{1,c} : \mathrm{curl}\, v = 0 \ \text{ and } \ \langle \mathrm{grad}\, q, v\rangle = 0, \ \forall q \in V_h^{0,c}\}. \tag{88}$$

In operator form, this amounts to finding $p_h \in V_h^0$, $B_h \in V_h^1 \cap (\mathcal{H}_h^1)^\perp$ and $z_h \in \mathcal{H}_h^1$ such that

$$\begin{cases} \alpha^0 S_h^0 p_h + \widetilde{\mathrm{div}}_h B_h = 0 \\ \mathrm{grad}_h\, p_h + \widetilde{\mathrm{curl}}_h\, \mathrm{curl}_h\, B_h + \alpha^1 S_h^1 B_h + z_h = \widetilde{\mathrm{curl}}_h\, \tilde{\Pi}_h^2 J \end{cases} \tag{89}$$

Proposition 5 *System (87) [or equivalently (89)] is well-posed for arbitrary non-zero stabilization parameters α^0, $\alpha^1 \neq 0$, and its solution satisfies*

$$\begin{aligned} &B_h \in V_h^{1,c} \cap (\mathcal{H}_h^1 \oplus \mathrm{grad}\, V_h^{0,c})^\perp \\ &p_h \in V_h^{0,c} \cap \ker \mathrm{grad} = \{0\} \\ &z_h = 0. \end{aligned} \tag{90}$$

Moreover the discrete magnetic field can be decomposed according to (17), as

$$B_h = B_h^{\mathrm{g}} + B_h^{\mathrm{h}} + B_h^{\mathrm{c}} \in \mathrm{grad}_h^c\, V_h^{0,c} \overset{\perp}{\oplus} \mathcal{H}_h^1 \overset{\perp}{\oplus} \widetilde{\mathrm{curl}}_h^c\, V_h^{2,c}$$

with discrete grad, harmonic and curl components characterized by

$$\begin{cases} B_h^{\mathrm{g}} = 0 \\ B_h^{\mathrm{h}} = 0 \\ \langle w, \operatorname{curl} B_h^{\mathrm{c}} \rangle = \langle w, J \rangle \qquad \forall w \in \operatorname{curl} V_h^{1,c}. \end{cases} \tag{91}$$

In particular, the solution is independent of the non-zero stabilization parameters and the conforming projection operators.

Proof The result follows by using appropriate test functions and the orthogonality of the conforming discrete Hodge–Helmholtz decomposition (17). In particular, taking $v = z_h$ (in $\mathcal{H}_h^1 \subset V_h^{1,c}$) yields $z_h = 0$, taking $q = (I - P_h^0)p_h$ and $v = \operatorname{grad} \bar{P}_h^0 p_h$ shows that $p_h = 0$, and the characterization of B_h follows by taking first $v = (I - P_h^1)B_h$ and then $v \in V_h^{1,c}$, an arbitrary conforming test function. □

Remark 4 Proposition 5 states that the auxiliary unknowns p_h and z_h may be discarded a posteriori from the system. However they are needed in (87) to have a square matrix.

In practice the discrete harmonic fields can be represented by a basis of $\mathcal{H}_h^1$, of the form $\Lambda_i^{1,H}$, $i = 1, \ldots, \dim(\mathcal{H}_h^1) = b_2(\Omega)$, computed as the zero eigenmodes of a penalized $\mathcal{L}_h^1 + \alpha S_h^1$, where $\alpha > 0$ is arbitrary and $b_2(\Omega)$ is the Betti number of order 2, i.e. the number of cavities in Ω. Using these harmonic fields, one assembles the rectangular mass matrix

$$(\mathbb{M}^{1,H})_{i,j} = \langle \Lambda_i^1, \Lambda_j^{1,H} \rangle, \quad i = 1, \ldots, N^1, \ \ j = 1, \ldots, b_2(\Omega). \tag{92}$$

which allows us to rewrite (87) as

$$\begin{cases} \alpha^0 \mathbb{S}^0 \mathbf{p} + (\mathbb{GP}^0)^T \mathbb{H}^1 \mathbf{B} = 0 \\ \mathbb{H}^1 \mathbb{GP}^0 \mathbf{p} + \big((\mathbb{CP}^1)^T \mathbb{H}^2 \mathbb{CP}^1 + \alpha^1 \mathbb{S}^1 \big) \mathbf{B} + \mathbb{M}^{1,H} \mathbf{z} = (\mathbb{CP}^1)^T \tilde{\boldsymbol{\sigma}}^2(J) \\ (\mathbb{M}^{1,H})^T \mathbf{B} = 0 \end{cases} \tag{93}$$

where $\mathbf{p}$, $\mathbf{B}$ and $\mathbf{z}$ contain the coefficients of p_h, B_h and z_h in the (primal) bases of V_h^0, V_h^1 and $\mathcal{H}_h^1$ respectively.

3.5.2 Magnetostatic Problem with Metallic Boundary Conditions

We next consider a boundary condition of the form

$$n \cdot B = 0$$

which corresponds to a metallic (perfectly conducting) boundary. In our framework it can be approximated by using the inhomogeneous sequence (4) which we denote by $\bar{V}^\ell$ as in Sect. 3.3, and by modelling the boundary condition in a weak form. The mixed formulation takes a form similar to (84) with a few changes. Namely, we now look for $p \in \bar{V}^0 = H^1(\Omega)$ and $B \in \bar{V}^1 = H(\operatorname{curl}; \Omega)$, solution to

$$\begin{cases} \langle \operatorname{grad} q, B \rangle = 0 & \forall q \in H^1(\Omega) \\ \langle v, \operatorname{grad} p \rangle + \langle \operatorname{curl} v, \operatorname{curl} B \rangle = \langle \operatorname{curl} v, J \rangle & \forall v \in H(\operatorname{curl}; \Omega). \end{cases} \tag{94}$$

Compared to (84), the only change is in the spaces chosen for the test functions. In particular we may formally decompose the second equation into a first set of test functions with $q|_{\partial\Omega} = 0$

which enforces $\operatorname{div} B = 0$, and a second set with $q|_{\partial\Omega} \neq 0$ which enforces $n \cdot B = 0$ on the boundary.

Again, this problem is not well-posed in general: on domains with holes (i.e., handles) a constraint must be added corresponding to harmonic forms, which leads to an augmented system with one additional Lagrange multiplier z_h as we did in the previous section. Here the proper space of harmonic forms is the one associated with the inhomogeneous sequence (4) involving $\bar{V}^1 = H(\operatorname{curl};\Omega)$ and $\bar{V}_1^* = H_0(\operatorname{div};\Omega)$. Thus, it reads

$$\bar{\mathcal{H}}^1(\Omega) = \{v \in H_0(\operatorname{div};\Omega) : \ \operatorname{curl} v = \operatorname{div} v = 0\}. \tag{95}$$

We also observe that now p is only defined up to constants, so that an additional constraint needs to be added, such as $p \in (\ker \operatorname{grad})^\perp$. In practice this constraint may either be enforced in a similar way as the harmonic constraint, or by a so-called regularization technique where a term of the form $\varepsilon\langle q, p\rangle$, with $\varepsilon \neq 0$, is added to the first equation of (94). The constrained problem reads then: Find $B \in H(\operatorname{curl};\Omega)$, $p \in H^1(\Omega)$ and $z \in \bar{\mathcal{H}}^1$, such that

$$\begin{cases} \varepsilon\langle q, p\rangle + \langle \operatorname{grad} q, B\rangle = 0 & \forall q \in H^1(\Omega) \\ \langle v, \operatorname{grad} p\rangle + \langle \operatorname{curl} v, \operatorname{curl} B\rangle + \langle v, z\rangle = \langle \operatorname{curl} v, J\rangle & \forall v \in H(\operatorname{curl};\Omega) \\ \langle w, B\rangle = 0 & \forall w \in \bar{\mathcal{H}}^1. \end{cases} \tag{96}$$

We note that here the result does not depend on ε (indeed by testing with $v = \operatorname{grad} p$ we find that p is a constant, and with $q = p$ we find that $p = 0$), hence we may set $\varepsilon = 1$.

At the discrete level we write a system similar to (87) or (89), but we must replace the space (88) with

$$\bar{\mathcal{H}}_h^1 = \{v \in \bar{V}_h^{1,c} : \operatorname{curl} v = 0 \ \text{ and } \ \langle \operatorname{grad} q, v\rangle = 0, \ \forall q \in \bar{V}_h^{0,c}\} \tag{97}$$

where we have denoted $\bar{V}_h^{\ell,c} = V_h^\ell \cap \bar{V}^\ell$. Observe that the for the inhomogeneous sequence, the decomposition (17) becomes

$$\bar{V}_h^{1,c} = \operatorname{grad}_h^c \bar{V}_h^{0,c} \overset{\perp}{\oplus} \bar{\mathcal{H}}_h^1 \overset{\perp}{\oplus} \widetilde{\operatorname{curl}}_h^c \bar{V}_h^{2,c} \tag{98}$$

where $\widetilde{\operatorname{curl}}_h^c : \bar{V}_h^{2,c} \to \bar{V}_h^{1,c}$ is now the discrete adjoint of $\operatorname{curl}_h^c : \bar{V}_h^{1,c} \to \bar{V}_h^{2,c}$.

We compute the space (97) as the kernel of the stabilized Hodge–Laplace operator associated with the inhomogeneous sequence, $\bar{\mathcal{H}}_h^1 = \ker(\bar{\mathcal{L}}_h^1 + \alpha^1 \bar{S}_h^1)$, with an arbitrary positive $\alpha^1 > 0$. Note that the matrix of $\bar{\mathcal{L}}_h^1$ takes the same form as in (48),

$$\bar{\mathbb{L}}^1 = \tilde{\mathbb{H}}^1 (\mathbb{C}\bar{\mathbb{P}}^1)^T \mathbb{H}^2 \mathbb{C}\bar{\mathbb{P}}^1 + \mathbb{G}\bar{\mathbb{P}}^0 \tilde{\mathbb{H}}^0 (\mathbb{G}\bar{\mathbb{P}}^0)^T \mathbb{H}^1 \tag{99}$$

where $\bar{\mathbb{P}}^0$ and $\bar{\mathbb{P}}^1$ are the conforming projection matrices on the inhomogeneous spaces, which leave the boundary degrees of freedom untouched instead of setting them to zero. The Hodge (mass) and differential matrices are those of the broken spaces which have no boundary conditions, hence they are the same as in Sect. 3.5.1. The resulting system reads: find $p_h \in \bar{V}_h^0$, $B_h \in \bar{V}_h^1$ and $z_h \in \bar{\mathcal{H}}_h^1$, such that

$$\begin{cases} \langle q, p_h\rangle + \alpha^0 \langle (I - \bar{P}_h^0)q, (I - \bar{P}_h^0)p_h\rangle + \langle \operatorname{grad} \bar{P}_h^0 q, B_h\rangle = 0 \\ \langle v, \operatorname{grad} \bar{P}_h^0 p_h\rangle + \langle \operatorname{curl} \bar{P}_h^1 v, \operatorname{curl} \bar{P}_h^1 B_h\rangle \\ \quad + \alpha^1 \langle (I - \bar{P}_h^1)v, (I - \bar{P}_h^1)B_h\rangle + \langle v, z_h\rangle = \langle \operatorname{curl} \bar{P}_h^1 v, J\rangle \\ \langle w, B_h\rangle = 0 \end{cases} \tag{100}$$

for all $q \in \bar{V}_h^0$, $v \in \bar{V}_h^1$ and $w \in \bar{\mathcal{H}}_h^1$. An operator form similar to (89) can also be written.

Finally the matrix form of our broken FEEC magnetostatic equation with metallic boundary conditions is similar to (93), with the following differences:

- the conforming projection operators map in the full conforming spaces $\bar{V}^\ell$ (boundary dofs are not set to zero),
- the discrete harmonic space is now $\bar{\mathcal{H}}_h^1$ the kernel of the $\bar{\mathcal{L}}_h^1$ operator associated with the full sequence, which in practice is also implemented by using conforming projection operators on the inhomogeneous spaces,
- a regularization term $\mathbb{M}^0\mathbf{p}$ involving the mass matrix in V_h^0 is added to the first equation to fully determine p.

Proposition 6 *System* (100) *is well-posed for arbitrary stabilization parameters* $\alpha^0 > 0$, $\alpha^1 \neq 0$, *and its solution satisfies*

$$\begin{aligned} &B_h \in \bar{V}_h^{1,c} \cap (\bar{\mathcal{H}}_h^1 \oplus \operatorname{grad} \bar{V}_h^{0,c})^\perp \\ &p_h = 0 \\ &z_h = 0. \end{aligned} \tag{101}$$

Moreover the discrete magnetic field can be decomposed according to (98), *as*

$$B_h = B_h^{\mathrm{g}} + B_h^{\mathrm{h}} + B_h^{\mathrm{c}} \in \operatorname{grad}_h^c \bar{V}_h^{0,c} \overset{\perp}{\oplus} \bar{\mathcal{H}}_h^1 \overset{\perp}{\oplus} \widetilde{\operatorname{curl}}_h^c \bar{V}_h^{2,c}$$

with discrete grad, harmonic and curl components characterized by

$$\begin{cases} B_h^{\mathrm{g}} = 0 \\ B_h^{\mathrm{h}} = 0 \\ \langle w, \operatorname{curl} B_h^{\mathrm{c}} \rangle = \langle w, J \rangle \qquad \forall w \in \operatorname{curl} \bar{V}_h^{1,c}. \end{cases} \tag{102}$$

In particular, the solution is independent of the parameters $\alpha^0 > 0$, $\alpha^1 \neq 0$, *and the conforming projection operators.*

Proof Taking $v = z_h$ (in $\bar{\mathcal{H}}_h^1 \subset \bar{V}_h^{1,c}$) and using the orthogonality (98) shows that $z_h = 0$. Taking next $v = \operatorname{grad} \bar{P}_h^0 p_h$ and using again (98) shows that $\bar{P}_h^0 p_h$ is a constant, and with $q = 1$ we see that $\langle 1, p_h \rangle = 0$. It follows that with $q = (I - \bar{P}_h^0) p_h$ the first equation becomes $\|p_h\|^2 + \alpha^0 \|(I - \bar{P}_h^0) p_h\|^2 = 0$, hence $p_h = 0$. Taking next $v = (I - \bar{P}_h^1) B_h$ yields $\|(I - \bar{P}_h^1) B_h\|^2 = 0$, hence $B_h \in \bar{V}_h^{1,c}$. Since it is orthogonal to both $\bar{\mathcal{H}}_h^1$ and $\operatorname{grad} \bar{V}_h^{0,c}$, it belongs to $\widetilde{\operatorname{curl}}_h^c V_h^{2,c}$, and it is characterized by $\langle \operatorname{curl} v, \operatorname{curl} B_h \rangle = \langle \operatorname{curl} v, J \rangle$ for all $v \in \bar{V}_h^{1,c}$, which completes the proof. □

3.6 Time-Dependent Maxwell's Equations

We conclude this section by recalling the CONGA discretization of Maxwell's time-dependent equations,

$$\begin{cases} \partial_t E - \operatorname{curl} B = -J \\ \partial_t B + \operatorname{curl} E = 0 \end{cases} \tag{103}$$

which consists of computing $E_h \in V_h^1$ and $B_h \in V_h^2$ solution to

$$\begin{cases} \partial_t E_h - \widetilde{\mathrm{curl}}_h B_h = -J_h \\ \partial_t B_h + \mathrm{curl}_h\, E = 0 \end{cases} \tag{104}$$

with a discrete source approximated with the dual commuting projection

$$J_h = \tilde{\Pi}_h^1 J. \tag{105}$$

This discretization has been proposed and studied in [18–20], where it has been shown to be structure-preserving and have long-time stability properties: in addition to conserve energy in the absence of sources, it preserves exactly the discrete Gauss laws

$$\begin{cases} \widetilde{\mathrm{div}}_h E_h = \tilde{\Pi}_h^0 \rho \\ \mathrm{div}_h\, B_h = 0 \end{cases} \tag{106}$$

thanks to the commuting diagram property $\widetilde{\mathrm{div}}_h \tilde{\Pi}_h^1 J = \tilde{\Pi}_h^0 \,\mathrm{div}\, J$ satisfied by the dual projection operators, see (34). Moreover, the filtering by $(P_h^1)^*$ involved in the source approximation operator (32) avoids the accumulation of approximation errors in the non-conforming part of the kernel of the CONGA curl curl operator [18].

Remark 5 The full commuting diagram property (34) is actually not needed for the preservation of the discrete Gauss law. One can indeed verify that (106) still holds for a current source defined by a simple L^2 projection,

$$J_h = Q_{V_h^1} J \tag{107}$$

since one has in this case $\langle \widetilde{\mathrm{div}}_h J_h, \varphi\rangle = -\langle J_h, \mathrm{grad}\, P_h^0 \varphi\rangle = -\langle J, \mathrm{grad}\, P_h^0 \varphi\rangle = \langle \mathrm{div}\, J, P_h^0 \varphi\rangle = \langle \tilde{\Pi}_h^0 \,\mathrm{div}\, J, \varphi\rangle$ so that (106) follows from the compatibility relation $\mathrm{div}\, J + \partial_t \rho = 0$ satisfied by the exact sources. The additional filtering of the source by $(P_h^1)^*$ involved in the dual commuting projection (105) is nevertheless important for long term stability, as analyzed in [18] and verified numerically in Sect. 5.7 below.

An attractive feature of the CONGA discretization is that for an explicit time-stepping method such as the standard leap-frog scheme

$$\begin{cases} B_h^{n+\frac{1}{2}} = B_h^n - \dfrac{\Delta t}{2}\,\mathrm{curl}_h\, E_h^n \\ E_h^{n+1} = E_h^n + \Delta t\big(\widetilde{\mathrm{curl}}_h B_h^{n+\frac{1}{2}} - \tilde{\Pi}_h^1 J^{n+\frac{1}{2}}\big) \\ B_h^{n+1} = B_h^{n+\frac{1}{2}} - \dfrac{\Delta t}{2}\,\mathrm{curl}_h\, E_h^{n+1} \end{cases} \tag{108}$$

each time step is purely local in space. This is easily seen in the matrix form of (108)

$$\begin{cases} \mathbf{B}^{n+\frac{1}{2}} = \mathbf{B}^n - \dfrac{\Delta t}{2}\mathbb{C}\mathbb{P}^1 \mathbf{E}^n \\ \mathbf{E}^{n+1} = \mathbf{E}^n + \Delta t \tilde{\mathbb{H}}^1\big((\mathbb{C}\mathbb{P}^1)^T \mathbb{H}^2 \mathbf{B}^{n+\frac{1}{2}} - (\mathbb{P}^1)^T \tilde{\boldsymbol{\sigma}}^1 (J^{n+\frac{1}{2}})\big) \\ \mathbf{B}^{n+1} = \mathbf{B}^{n+\frac{1}{2}} - \dfrac{\Delta t}{2}\mathbb{C}\mathbb{P}^1 \mathbf{E}^{n+1} \end{cases} \tag{109}$$

where all the matrices except $\mathbb{P}^1$ are patch-diagonal, and $\mathbb{P}^1$ only couples degrees of freedom of neighboring patches.

Another key property is that for a time-averaged current source,

$$J^{n+\frac{1}{2}} := \Delta t^{-1} \int_{t^n}^{t^{n+1}} J(t')\,\mathrm{d}t', \tag{110}$$

the discrete Gauss law (106) is also preserved by the fully discrete solution, namely

$$\begin{cases} \widetilde{\mathrm{div}}_h E_h^n = \tilde{\Pi}_h^0 \rho(t^n) \\ \mathrm{div}_h B_h^n = 0 \end{cases} \tag{111}$$

holds for all $n > 0$, provided it holds for $n = 0$. We also remind that in the absence of source ($J = 0$), the leap-frog time scheme requires a standard CFL condition for numerical stability, of the form

$$\Delta t \,|||\,\mathrm{curl}_h\,||| < 2 \tag{112}$$

where $|||\,\mathrm{curl}_h\,||| = \max_{\boldsymbol{F}\in V_h^1} \frac{\|\mathrm{curl}_h\,\boldsymbol{F}\|}{\|\boldsymbol{F}\|}$. Indeed the discrete pseudo-energy

$$\mathcal{H}_h^{n,*} := \frac{1}{2}\big(\|\boldsymbol{E}_h^n\|^2 + \|B_h^{n+\frac{1}{2}}\|^2\big) + \frac{\Delta t}{2}\langle \mathrm{curl}_h\,\boldsymbol{E}_h^n,\, B_h^{n+\frac{1}{2}}\rangle$$

is a constant, $\mathcal{H}_h^{n,*} = \mathcal{H}_h^*$, so that (112) yields a long-time bound

$$\Big(1 + \frac{\Delta t\,|||\,\mathrm{curl}_h\,|||}{2}\Big)^{-1} \mathcal{H}_h^* \le \frac{1}{2}\big(\|\boldsymbol{E}_h^n\|^2 + \|B_h^{n+\frac{1}{2}}\|^2\big) \le \Big(1 - \frac{\Delta t\,|||\,\mathrm{curl}_h\,|||}{2}\Big)^{-1} \mathcal{H}_h^*$$

valid for all $n \ge 0$. In practice we set $\Delta t = C_{\mathrm{cfl}}(2/|||\,\mathrm{curl}_h\,|||)$ with $C_{\mathrm{cfl}} \approx 0.8$, and we evaluate the operator norm of curl_h with an iterative power method, noting that it amounts to computing the spectral radius of a diagonalizable matrix with non-negative eigenvalues, namely

$$|||\,\mathrm{curl}_h\,|||^2 = \max_{\boldsymbol{F}\in V_h^1} \frac{\langle \widetilde{\mathbf{curl}}_h\,\mathrm{curl}_h\,\boldsymbol{F},\,\boldsymbol{F}\rangle}{\|\boldsymbol{F}\|^2} = \rho\big(\tilde{\mathbb{H}}^1(\mathbb{CP}^1)^T\,\mathbb{H}^2\mathbb{CP}^1\big).$$

4 Geometric Broken FEEC Discretizations with Mapped Spline Patches

In this section we detail the construction of a broken FEEC discretization on a 2D multipatch domain where each patch is the image of the reference square,

$$\Omega_k = F_k(\hat{\Omega}), \quad \hat{\Omega} =]0,1[^2 \tag{113}$$

with smooth diffeomorphisms F_k, $k = 1,\dots,K$. For simplicity we consider the case of planar domains $\Omega_k \subset \mathbb{R}^2$ and orientation-preserving mappings, in the sense that the Jacobian matrices $DF_k(\hat{\boldsymbol{x}})$ have positive Jacobian determinants $J_{F_k}(\hat{\boldsymbol{x}}) = \det(DF_k(\hat{\boldsymbol{x}})) > 0$ for all $\hat{\boldsymbol{x}} \in \hat{\Omega}$.

We also assume that the multipatch decomposition is conforming in the sense that any interface $\Gamma_{k,l} = \partial\Omega_k \cap \partial\Omega_l$ between two distinct patches

(i) is either a vertex, or a full edge of both patches,
(ii) admits the same parametrization from both patches, up to the orientation.

In the case where the interface is a vertex, condition (ii) is empty. If it is a full patch edge of the form

$$\Gamma_{k,l} = F_k([\hat{\boldsymbol{x}}_0, \hat{\boldsymbol{x}}_0 + \boldsymbol{e}_d]) = F_l([\hat{\boldsymbol{y}}_0, \hat{\boldsymbol{y}}_0 + \boldsymbol{e}_b]) \tag{114}$$

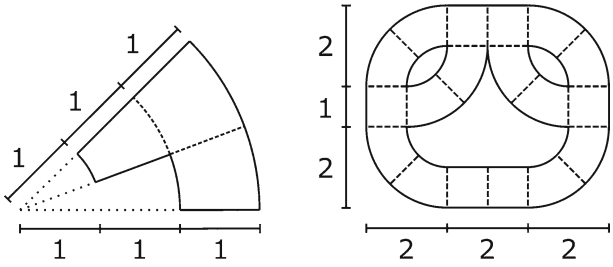

Fig. 1 Two multipatch domains: a curved L-shaped (left) and a non-contractible domain (right). Solid and dashed lines are used to represent the domain boundaries and the patch interfaces, respectively

where $\hat{\boldsymbol{x}}_0$ and $\hat{\boldsymbol{y}}_0$ are vertices of the reference domain $\hat{\Omega}$, condition (ii) means that

$$F_k(\hat{\boldsymbol{x}}_0 + s\boldsymbol{e}_d) = F_l(\hat{\boldsymbol{y}}_0 + \theta_{k,l}(s)\boldsymbol{e}_b), \quad s \in [0,1] \tag{115}$$

holds with $\theta_{k,l}$ an affine bijection on $[0, 1]$, that is $\theta_{k,l}(s) = s$ or $1 - s$.

With spline spaces defined on each patch with symmetric knot sequences, these conditions imply that the patches are fully matching in the sense of Assumption 3.3 from Buffa et al. [13].

Examples of such domains are represented on Fig. 1 where the left one is a standard curved L-shaped domain with circular patch boundaries that is used in some reference academic test-cases, see e.g. [29], and the right one is a non contractible domain that also involves analytical mappings, shaped as a simplified pretzel for cultural reasons. In the latter domain we remind that the presence of holes leads a priori to non exact de Rham sequences, and hence non trivial harmonic forms.

On such multipatch domains, the construction of mapped spline complexes is fairly standard

[15, 16]: for each patch a reference spline complex is first defined on the logical domain $\hat{\Omega}$ using tensor-product spaces, and the mapped spline spaces are next obtained by transforming the reference ones with push-forward operators. To build our conforming projection operators we shall use geometric degrees of freedom corresponding to pointwise evaluations and integrations over geometric elements, following the approach of Bochev et al. [4], Robidoux [47] and Gerritsma [31]. Specifically, we consider *broken* geometric degrees of freedom of the form

$$\sigma^0_{k,\boldsymbol{i}}(v) = v|_{\Omega_k}(\mathrm{n}_{k,\boldsymbol{i}}), \quad \sigma^1_{k,\mu}(\boldsymbol{v}) = \int_{\mathrm{e}_{k,\mu}} \boldsymbol{v}|_{\Omega_k} \cdot \boldsymbol{\tau}^*, \quad \sigma^2_{k,\boldsymbol{i}}(v) = \int_{\mathrm{c}_{k,\boldsymbol{i}}} v|_{\Omega_k} \tag{116}$$

associated with local grids nodes $\mathrm{n}_{k,\boldsymbol{i}}$, edges $\mathrm{e}_{k,\mu}$ and cells $\mathrm{c}_{k,\boldsymbol{i}}$ in each patch Ω_k. Here $\boldsymbol{\tau}^* = \boldsymbol{\tau}$ (a unit vector tangent to $\mathrm{e}_{k,\mu}$) or $\boldsymbol{\tau}^\perp$ (normal to the edge), depending on which 2D de Rham sequence is used. We refer to Section B in the Appendix for more details.

4.1 Conforming Projection Operators

In addition to yield commuting projection operators, geometric degrees of freedom naturally provide a simple characterization of the discrete fields v_h in the broken spaces V_h^ℓ which are actually conforming. In order to belong to the space V^ℓ appearing in the continuous de Rham sequence (1) (and hence to the conforming spline space $V_h^{\ell,c} = V_h^\ell \cap V^\ell$) a field must satisfy regularity conditions which are well known for piecewise-smooth functions. For

$\ell = 0$, the condition for $H^1(\Omega)$ regularity amounts to continuity across the patch interfaces, which is equivalent to requiring that the broken degrees of freedom associated to the same interpolation node coincide:

$$\mathrm{n}_{k,\boldsymbol{i}} = \mathrm{n}_{l,\boldsymbol{j}} \quad \Longrightarrow \quad \sigma^0_{k,\boldsymbol{i}}(v_h) = \sigma^0_{l,\boldsymbol{j}}(v_h). \tag{117}$$

For $\ell = 1$ in the **grad** $-$ curl sequence, the interface constraint for $\boldsymbol{H}(\mathrm{curl};\Omega)$ regularity consists in the continuity of the tangential traces, which amounts to requiring that edge degrees of freedom associated to the same edge coincide, up to the orientation. Namely,

$$\mathrm{e}_{k,\mu} = \mathrm{e}_{l,\nu} \quad \Longrightarrow \quad \sigma^1_{k,\mu}(v_h) = \varepsilon^{\mathrm{e}}(k,\mu;l,\nu)\sigma^1_{l,\nu}(v_h) \tag{118}$$

where $\varepsilon^{\mathrm{e}}(k,\mu;l,\nu) = \pm 1$ is the relative orientation of the edges, see (B.15).

For $\ell = 1$ in the **curl** $-$ div sequence, the interface constraint for $\boldsymbol{H}(\mathrm{div};\Omega)$ regularity consists in the continuity of the normal traces, which again amounts to requiring that edge degrees of freedom associated to the same edge coincide, up to the orientation: this constraint takes the same form as (118). Finally as $V^2 = L^2(\Omega)$ there are no constraints for $\ell = 2$, i.e., the spaces V^2_h and $V^{2,c}_h$ coincide. We gather these constraints in a single formula

$$\mathrm{g}^\ell_{k,\mu} = \mathrm{g}^\ell_{l,\nu} \quad \Longrightarrow \quad \sigma^\ell_{k,\mu}(v_h) = \varepsilon^\ell(k,\mu;l,\nu)\sigma^\ell_{l,\nu}(v_h) \tag{119}$$

where $\mathrm{g}^\ell_{k,\mu}$ denotes the geometric element (node, edge or cell) of dimension ℓ associated with a multi-index $(k,\mu) \in \mathcal{M}^\ell_h$, and ε^1 denotes the relative orientation of two edges, while $\varepsilon^0 = \varepsilon^2 := 1$.

Thanks to the conformity assumption of the multipatch geometry and to the symmetry of the interpolatory grid, each broken degree of freedom on an interface can be matched to those of the adjacent patches in such a way that the constraints above are satisfied. Accordingly, the resulting broken discrete field will belong to the conforming space $V^{\ell,c}_h$. In particular we may define simple conforming projection operators P^ℓ by averaging the broken degrees of freedom associated with interface elements. Using the broken basis functions $\Lambda^\ell_{k,\mu}$ associated with the above degrees of freedom, this yields an expression similar to the one given in [23] for tensor-product polynomial elements, with additional relative orientation factors due to the general mapping configurations,

$$P^\ell_h \Lambda^\ell_{l,\nu} := \frac{1}{\#\mathcal{M}^\ell_h(\mathrm{g}^\ell_{l,\nu})} \sum_{(k,\mu)\in\mathcal{M}^\ell_h(\mathrm{g}^\ell_{l,\nu})} \varepsilon^\ell(k,\mu;l,\nu)\Lambda^\ell_{k,\mu} \tag{120}$$

where $\mathcal{M}^\ell_h(\mathrm{g}^\ell_{l,\nu})$ contains the patch-wise indices corresponding to a given geometric element. The entries of the corresponding operator matrix (36) read

$$\mathbb{P}_{(k,\mu),(l,\nu)} = \begin{cases} \frac{\varepsilon^\ell(k,\mu;l,\nu)}{\#\mathcal{M}^\ell_h(\mathrm{g}^\ell_{l,\nu})} & \text{if } \mathrm{g}^\ell_{k,\mu} = \mathrm{g}^\ell_{l,\nu} \\ 0 & \text{otherwise} \end{cases} \tag{121}$$

for all $(k,\mu), (l,\nu) \in \mathcal{M}^\ell_h$. We may summarize our construction with the following result.

Proposition 7 *The broken geometric degrees of freedom* (116) *satisfy the properties listed in Sect. 2.4, with local domain spaces* $U^\ell(\Omega_k)$ *defined in* (B.19) *and local differential matrices independent of the mappings* F_k. *Moreover, the operators* $P^\ell_h : V^\ell_h \to V^\ell_h$ *defined by* (120) *are projections on the conforming subspaces* $V^{\ell,c}_h = V^\ell_h \cap V^\ell$.

Proof The boundedness of $\sigma^\ell_{k,\mu}$ on the local spaces $U^\ell(\Omega_k)$, as well as the commuting properties, are verified in Proposition B.2 in the Appendix. The inter-patch conformity property (31) follows from the fact that piecewise smooth functions that belong to $H^1(\Omega)$, resp. $H(\mathrm{curl};\Omega)$ and $H(\mathrm{div};\Omega)$, admit a unique trace, resp. tangential and normal trace on patch interfaces [5]. The same property, together with the interpolation nature of the geometric basis functions, allows verifying that the operators $P^\ell_h : V^\ell_h \to V^\ell_h$ are characterized by the relations

$$\sigma^\ell_{k,\mu}(P^\ell_h v_h) = \frac{1}{\#\mathcal{M}^\ell_h(\mathfrak{g}^\ell_{k,\mu})} \sum_{(l,\nu)\in\mathcal{M}^\ell_h(\mathfrak{g}^\ell_{k,\mu})} \varepsilon^\ell(k,\mu;l,\nu)\sigma^\ell_{l,\nu}(v_h) \tag{122}$$

for all $(k,\mu) \in \mathcal{M}^\ell_h$. Using the geometric condition (119), this allows verifying that P^ℓ_h is indeed a projection on the conforming subspace $V^{\ell,c}_h$. □

Remark 6 (*Boundary conditions*) As stated, the above construction actually corresponds to the inhomogeneous sequences. If one considers the spaces with homogeneous boundary conditions,

then P^ℓ_h should further set the boundary degree of freedom to 0, which amounts to restricting the non-zeros entries in (121) to the geometrical elements $\mathfrak{g}^\ell_{k,\mu}$ that are inside Ω. As already observed in Sect. 3.3, this does not affect the broken spaces V^ℓ_h since they are not required to have boundary conditions.

Remark 7 (*Extension to 3D*) The extension to the 3D setting of the above construction poses no particular difficulty, using the same tensor-product and mapped spline spaces as in [15, 27], and the same geometric degrees of freedom as in [24, Sect. 6.1] for the primal sequence.

4.2 Primal-Dual Matrix Diagram with B-Splines

In practice, a natural approach is to work with B-splines. Indeed the geometric (interpolatory) splines $\Lambda^\ell_{k,\mu}$ (dual to the geometric degrees of freedom) are not known explicitly and depend on the interpolation grids. They are also less local than the B-splines, as they are in general supported on their full patch Ω_k: for patches with many cells, this would lead to an expensive computation of the fully populated mass matrices.

In our numerical experiments we have followed da Veiga et al. [27] and Campos Pinto et al. [24] and used tensor-product splines $\hat{B}^\ell_\mu$ on the reference domain $\hat{\Omega}$, composed of normalized B-splines $\mathcal{N}^p_i$ in the dimensions of degree p and of Curry-Schoenberg B-splines $\mathcal{D}^{p-1}_i = \left(\frac{p}{\xi_{i+p+1}-\xi_{i+1}}\right)\mathcal{N}^{p-1}_{i+1}$ (also called M-splines) in the dimensions of degree $(p-1)$. On the mapped patches $\Omega_k = F_k(\hat{\Omega})$ the basis functions are defined again as push-forwards $B^\ell_{k,\mu} := \mathcal{F}^\ell_k(\hat{B}^\ell_\mu)$ for $(k,\mu) \in \mathcal{M}^\ell_h$.

The discrete elements in the matrix diagram (41) must then be adapted for B-splines: one first observe that the change of basis is provided by the patch-wise collocation matrices whose diagonal blocks read

$$\mathbb{K}^\ell_{(k,\mu),(k,\nu)} = \sigma^\ell_{k,\mu}(B^\ell_{k,\nu}) = \hat{\sigma}^\ell_\mu(\hat{B}^\ell_\nu), \quad \mu,\nu \in \hat{\mathcal{M}}^\ell \tag{123}$$

where we have used (B.10) from the Appendix. As $B^\ell_{k,\nu} = \sum_\mu \mathbb{K}^\ell_{(k,\mu),(k,\nu)} \Lambda^\ell_{k,\mu}$ it follows that the B-spline coefficients of the geometric projection (30), namely

$$\Pi^\ell_h v = \sum_{(k,\mu)\in\mathcal{M}^\ell_h} \sigma^\ell_{k,\mu}(v)\Lambda^\ell_{k,\mu} = \sum_{(k,\mu)\in\mathcal{M}^\ell_h} \beta^\ell_{k,\mu}(v) B^\ell_{k,\mu} \tag{124}$$

read (using some implicit flattening $\mathcal{M}^\ell_h \ni (k,\mu) \mapsto i \in \{1,\dots,N^\ell\}$)

$$\boldsymbol{\beta}^\ell(v) = (\mathbb{K}^\ell)^{-1}\boldsymbol{\sigma}^\ell(v). \tag{125}$$

Accordingly, we obtain the matrices $\mathbb{P}^\ell_B = (\beta^\ell_i(P^\ell_h B^\ell_j))_{1\le i,j\le N^\ell}$ of the conforming projection operator (120) in the B-spline bases by combining the matrices (121) with the above change of basis: this gives

$$\mathbb{P}^\ell_B = (\mathbb{K}^\ell)^{-1}\mathbb{P}^\ell\mathbb{K}^\ell. \tag{126}$$

Here we note that the collocation matrices $\mathbb{K}^\ell$ are Kronecker products of univariate banded matrices, see [24, Sect. 6.2], so that (125) and (126) may be implemented in a very efficient way. The primal sequence is completed by computing the patch-wise differential matrices in the B-spline bases,

$$(\mathbb{D}^\ell_B)_{(k,\mu),(k,\nu)} := \beta^{\ell+1}_{k,\mu}(d^\ell B^\ell_{k,\nu}).$$

Thanks to the univariate relation $\frac{\mathrm{d}}{\mathrm{d}x}\mathcal{N}^p_i = \mathcal{D}^{p-1}_{i-1} - \mathcal{D}^{p-1}_i$, these are patch-wise incidence matrices, just as the ones in the geometric bases [24, 27]. For the dual sequence we use bi-orthogonal splines characterized by the relations

$$\tilde{B}_{k,\mu} \in V^\ell_h(\Omega_k), \quad \tilde{\beta}^\ell_{k,\nu}(\tilde{B}^\ell_{k,\mu}) = \delta_{\mu,\nu} \quad \forall \mu,\nu \in \hat{\mathcal{M}}^\ell$$

with dual degrees of freedom

$$\tilde{\beta}^\ell_{k,\mu}(v) := \langle v, B^\ell_{k,\mu}\rangle. \tag{127}$$

This leads to defining again the primal Hodge matrices as patch-diagonal mass matrices, $\mathbb{H}^\ell_B = \mathbb{M}^\ell_B$ and the dual Hodge ones as their patch-diagonal inverses $\tilde{\mathbb{H}}^\ell_B = (\mathbb{M}^\ell_B)^{-1}$. These matrices can be computed on the reference domain according to

$$(\mathbb{M}^\ell_B)_{(k,\mu),(k,\nu)} = \langle B^\ell_{k,\mu}, B^\ell_{k,\nu}\rangle = \langle \mathcal{F}^\ell_k(\hat{B}^\ell_\mu), \mathcal{F}^\ell_k(\hat{B}^\ell_\nu)\rangle. \tag{128}$$

Specifically, for the 2D **grad** − curl sequence we obtain

$$(\mathbb{M}^\ell_B)_{(k,\mu),(k,\nu)} = \begin{cases} \int_{\hat{\Omega}} \hat{B}^0_\mu \hat{B}^0_\nu J_{F_k}\,\mathrm{d}\hat{\boldsymbol{x}}, & \text{for} \ell = 0 \\ \int_{\hat{\Omega}} (\hat{B}^1_\mu)^T (DF_k^T DF_k)^{-1} \hat{B}^1_\nu J_{F_k}\,\mathrm{d}\hat{\boldsymbol{x}}, & \text{for} \ell = 1 \\ \int_{\hat{\Omega}} (\hat{B}^2_\mu)^T \hat{B}^2_\nu J^{-1}_{F_k}\,\mathrm{d}\hat{\boldsymbol{x}}, & \text{for} \ell = 2 \end{cases} \tag{129}$$

and for the 2D **curl** − div sequence we find

$$(\mathbb{M}^1_B)_{(k,\mu),(k,\nu)} = \int_{\hat{\Omega}} (\hat{B}^1_\mu)^T DF_k^T DF_k \hat{B}^1_\nu J^{-1}_{F_k}\,\mathrm{d}\hat{\boldsymbol{x}}, \tag{130}$$

while $\mathbb{M}^0_B$ and $\mathbb{M}^2_B$ take the same values as in (129). Here we have used the explicit form of the pull-back operators (A.12) and (A.13) recalled in the Appendix. In 3D the formulas can be derived from the pull-backs given in [27].

Finally the coefficients of the dual commuting projections (32)–(33) in the dual B-spline bases read

$$\tilde{\boldsymbol{\beta}}^{\ell}(\tilde{\Pi}_h^{\ell} v) = (\mathbb{P}_B^{\ell})^T \tilde{\boldsymbol{\beta}}^{\ell}(v)$$

using the dual degrees of freedom (127) and the same implicit flattening as in (125), (126).

Gathering the above elements in 3D we obtain a new version of diagram (41), where the coefficient spaces (still defined as $\mathbb{R}^{N^\ell}$) are now denoted $\mathcal{C}_B^\ell$ and $\tilde{\mathcal{C}}_B^\ell$ to indicate that they contain coefficients in the B-spline and dual B-spline basis, respectively.

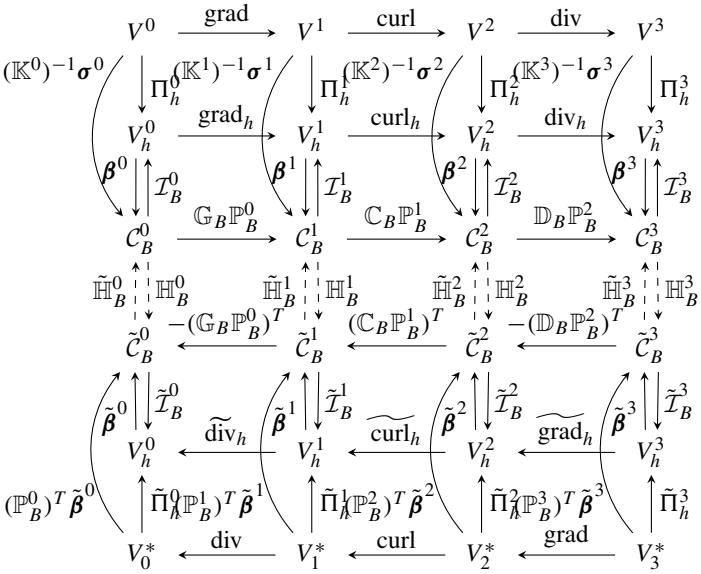

(131)

Note that here the primal and dual interpolation operators are simply

$$\mathcal{I}_B^{\ell} : \mathbf{b} \mapsto \sum_{i=1}^{N^\ell} b_i B_i^{\ell} \quad \text{and} \quad \tilde{\mathcal{I}}_B^{\ell} : \tilde{\mathbf{b}} \mapsto \sum_{i=1}^{N^\ell} \tilde{b}_i \tilde{B}_i^{\ell} \,. \tag{132}$$

5 Numerical Validation of the Broken FEEC Schemes

In this section we conduct numerical experiments to test our novel broken FEEC schemes from Sect. 3 using the multipatch spline spaces described in Sect. 4. These experiments have been performed with the Psydac library [32], where the different operators from the primal/dual commuting diagram (131) have been implemented. In contrast to conforming FEEC appproximations, we remind that these operators are local in the sense explained in the introduction, thanks ot the use of the fully discontinuous spaces V_h^ℓ and the local conforming projections represented by the matrices $\mathbb{P}_B^\ell$.

Table 1 Relative L^2 errors for the Poisson problem with homogeneous boundary conditions discretized with (52), using various numbers of cells per patch and spline degrees. In each case the error is computed with respect to the finite element projection $\Pi_h^0 \phi$ of the analytic solution (133) on the space V_h^0

Degree	2×2	3×3	4×4	5×5
Cells p.p.				
4×4	0.99420	0.73962	0.35919	0.41536
8×8	0.11599	0.12811	0.13921	0.16493
16×16	0.00692	0.00892	0.01013	0.00684

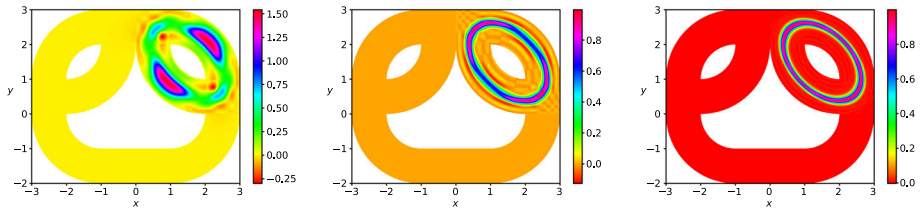

(a) 4×4 cells p.p. (b) 8×8 cells p.p. (c) 16×16 cells p.p.

Fig. 2 Solutions $\phi_h \in V_h^0$ computed by the scheme (52), with spline elements of degree 3×3 and $N \times N$ of cells per patches as indicated, corresponding to some of the errors shown in Table 1

5.1 Poisson Problem with Homogeneous Boundary Conditions

We first test our CONGA scheme for the homogeneous Poisson problem presented in Sect. 3.1. For this we consider an analytical solution on the pretzel-shaped domain shown in Fig. 1, given by

$$\phi(\boldsymbol{x}) = \exp\Big(-\frac{\tau^2(\boldsymbol{x})}{2\sigma^2}\Big) \quad \text{with} \quad \tau(\boldsymbol{x}) = as^2(\boldsymbol{x}) + bt^2(\boldsymbol{x}) - 1. \tag{133}$$

Here, $s(\boldsymbol{x}) = \tilde{x} - \tilde{y}$, $t(\boldsymbol{x}) = \tilde{x} + \tilde{y}$ with $\tilde{x} = x - x_0$, $\tilde{y} = y - y_0$ and we take $x_0 = y_0 = 1.5$, $a = (1/1.7)^2$, $b = (1/1.1)^2$ and $\sigma = 0.11$ in order to satisfy the homogeneous boundary condition with accuracy $\approx 1e-10$. The associated manufactured source is

$$f = -\Delta\phi = -\left(\frac{\tau^2\|\nabla\tau\|^2}{\sigma^4} - \frac{\tau\Delta\tau + \|\nabla\tau\|^2}{\sigma^2}\right)\phi\,. \tag{134}$$

In Table 1 we show the relative L^2 errors corresponding to different grids and spline degrees, and in Fig. 2 we plot the numerical solutions corresponding to spline elements of degree 3×3 on each patch. These results show that the numerical solutions converge towards the exact one as the grids are refined. We do not observe significant improvements however when higher order polynomials are used. As the next results will show, this is most likely due to the steep nature of the solution.

5.2 Poisson Problem with Inhomogeneous Boundary Conditions

Our second test is with an inhomogeneous Poisson–Dirichlet problem (64), using the lifting method described in Sect. 3.3 for the boundary condition and the solver tested just above for the homogeneous part of the solution. Specifically, we define $\phi_{g,h} \in V_h^0$ by computing its

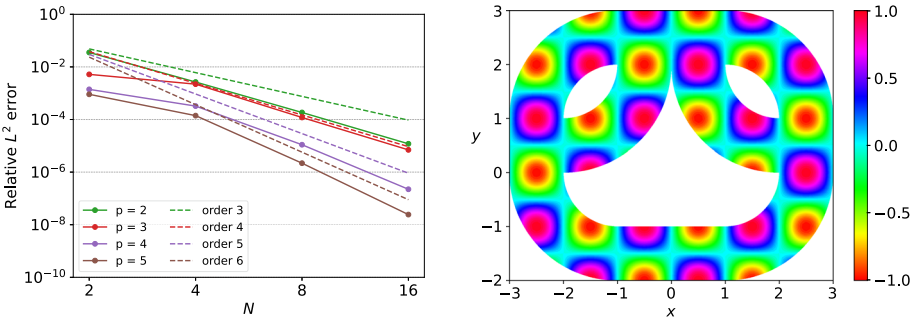

(a) convergence curves (b) solution ϕ_h for $N = 16$, $p = 3$

Fig. 3 Convergence study for the inhomogeneous Poisson solver with source and boundary conditions given by (135). The left plot shows the relative L^2 errors corresponding to various grids of $N \times N$ cells per patch (i.e., $18N^2$ cells in total) and spline degrees $p \times p$ as indicated. The right plot shows one numerical solution ϕ_h of good accuracy

boundary degrees of freedom from the data g on $\partial\Omega$ (this is straightforward with our geometric boundary degrees of freedom (B.12)), and we compute $\phi_{0,h} = \phi_h - \phi_{g,h}$ by solving (67). As we are not constrained by a specific condition on the domain boundary we consider a smooth solution to assess whether high order convergence rates can be observed despite the singularities in the domain boundaries. Specifically, we use again the pretzel-shaped domain and set the source and boundary condition as

$$f(\boldsymbol{x}) = -2\pi^2 \sin(\pi x)\cos(\pi y) \ \text{ in } \Omega, \quad g(\boldsymbol{x}) = \phi(\boldsymbol{x}) \ \text{ on } \partial\Omega \tag{135}$$

where $\phi(\boldsymbol{x}) = \sin(\pi x)\cos(\pi y)$ is the exact solution.

In Fig. 3 we plot the convergence curves corresponding to various $N \times N$ grids for the 18 patches of the domain, and various degrees $p = 2, \ldots 5$. They show that the solutions converge with optimal rate $p + 1$ (and even $p + 2$ for $p = 2$) as the patch grids are refined. Since the stabilized broken FEEC solution coincides with the conforming one according to our analysis in Sects. 3.1 and 3.3, these rates follow from the optimality of conforming FEM approximations to elliptic problems and the approximation power of multipatch spline spaces established in [16].

5.3 Time-Harmonic Maxwell Problem with Homogeneous Boundary Conditions

We next turn to a numerical assessment of our CONGA solvers for the Maxwell equation, and as we did for the Poisson equation we begin with the homogeneous case presented in Sect. 3.2. Since now the solution depends a priori on the time pulsation ω we opt for a physically relevant current source localized around the upper right hole of the pretzel-shaped domain,

$$\boldsymbol{J} = \phi \mathbf{curl} \tau \tag{136}$$

where ϕ and τ are as in (133). We plot this source in Fig. 4.

We then consider two values for the time pulsation, namely $\omega = \sqrt{50}$ and $\omega = \sqrt{170}$, and for each of these values we use as reference solutions the numerical solutions computed using our method on a mesh with 20×20 cells per patch (i.e. 7200 cells in total) and elements of degree 6×6 in each patch. These reference solutions are shown in Fig. 5. Interestingly,

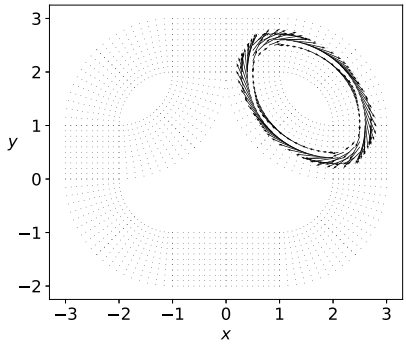

(a) vector field $\boldsymbol{J}$

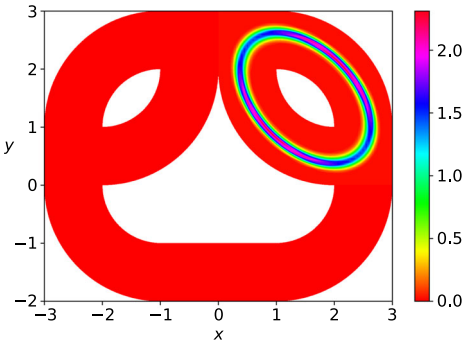

(b) amplitude $|\boldsymbol{J}|$

Fig. 4 Source (136) (vector field and amplitude) for the homogeneous Maxwell solutions plotted in Fig. 5 below

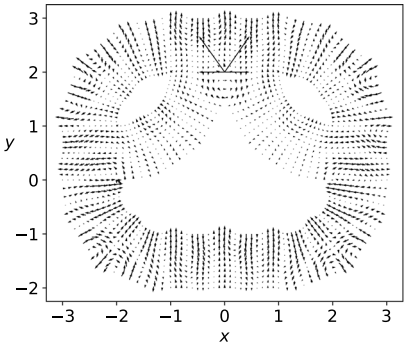

(a) vector field ($\omega = \sqrt{50}$)

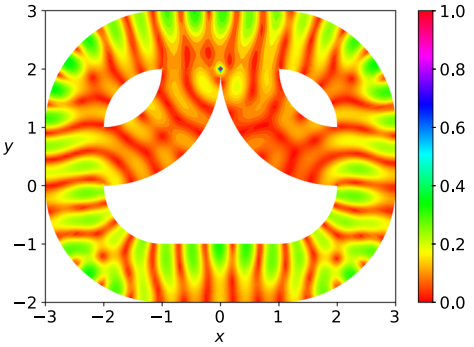

(b) amplitude ($\omega = \sqrt{50}$)

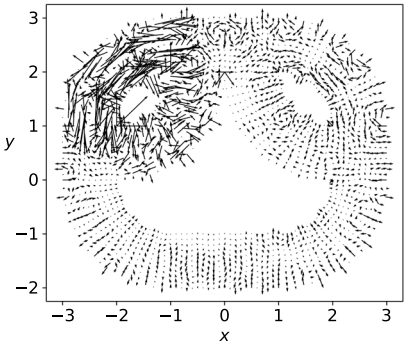

(c) vector field ($\omega = \sqrt{170}$)

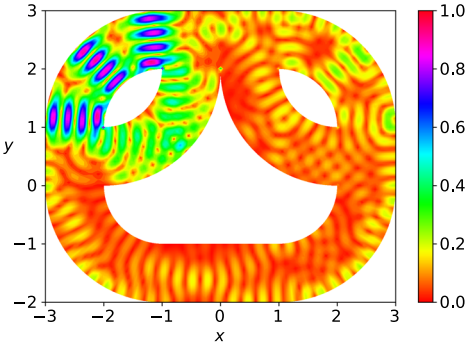

(d) amplitude ($\omega = \sqrt{170}$)

Fig. 5 Reference numerical solutions for the homogeneous Maxwell problem with source (136) and time pulsation $\omega = \sqrt{50}$ (top) and $\omega = \sqrt{170}$ (bottom). These solutions have been obtained using 20×20 cells per patch and spline elements of degree 6×6. The vector fields are shown on the left while the amplitudes are shown on the right

Table 2 L^2 errors for the solution of the homogeneous Maxwell problem with source (136) and time pulsation ω as indicated. Here the errors are computed using the numerical reference solutions shown in Fig. 5

Degree	2×2	3×3	4×4	5×5
Cells p.p.				
Errors for $\omega = \sqrt{50}$				
4×4	1.32277	1.53875	0.42168	0.02399
8×8	0.45461	0.03990	0.03640	0.02547
16×16	0.02158	0.02354	0.01333	0.00738
Errors for $\omega = \sqrt{170}$				
4×4	0.99472	1.00119	1.00864	1.00200
8×8	1.03397	1.39890	0.29048	0.11714
16×16	0.68206	0.00828	0.00880	0.00484

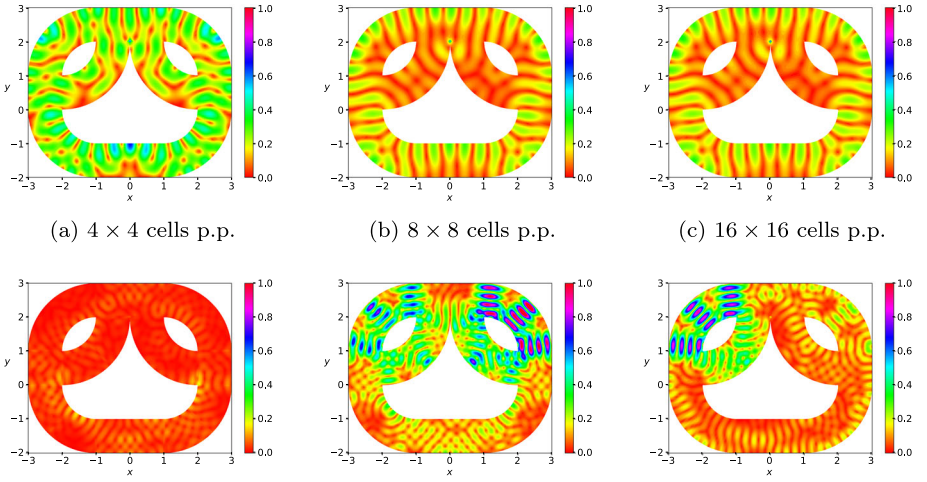

(a) 4×4 cells p.p. (b) 8×8 cells p.p. (c) 16×16 cells p.p.

(d) 4×4 cells p.p. (e) 8×8 cells p.p. (f) 16×16 cells p.p.

Fig. 6 Numerical solutions obtained with spline elements of degree 3×3 and different grids as indicated, corresponding to the errors shown in Table 2

we observe that for the higher pulsation $\omega = \sqrt{170}$ the source triggers a time-harmonic field localized around the upper left hole, opposite to where the source is.

In Table 2 we show the L^2 errors corresponding to different grids and spline degrees for the two values of the pulsation ω, and we also plot in Fig. 6 the different solutions corresponding to spline elements of degree 3×3. These results show that the numerical solutions converge towards the reference ones as the grids are refined, and with a faster convergence in the case of the lower pulsation $\omega = \sqrt{50}$, due to the higher smoothness of the corresponding solution.

5.4 Time-Harmonic Maxwell Problem with Inhomogeneous Boundary Conditions

As we did for the Poisson problem, we next test our Maxwell solver with a smooth solution and handle the inhomogeneous boundary conditions with the lifting method described in Sect. 3.3. Specifically, we define $\boldsymbol{u}_{g,h} \in V_h^1$ by computing its boundary degrees of freedom from the data $g = \boldsymbol{n} \times \boldsymbol{u}$ on $\partial\Omega$ [this is again straightforward with our geometric boundary

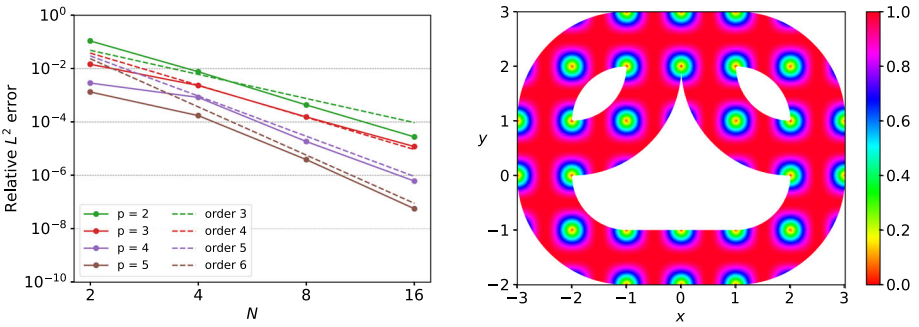

(a) convergence curves (b) solution $|\boldsymbol{u}_h|$ for $N = 16$, $p = 3$

Fig. 7 Convergence study for the time-harmonic Maxwell solver with source given by (137) and inhomogeneous boundary conditions $\boldsymbol{n} \times \boldsymbol{u} = g$. Relative L^2 errors are plotted on the left for various grids of $N \times N$ cells per patch (corresponding to a total of $18N^2$ cells) and spline degrees $p \times p$ as indicated. The right plot shows the amplitude of a numerical solution $\boldsymbol{u}_h$ of good accuracy

degrees of freedom (B.13)], and we compute $\boldsymbol{u}_{0,h} = \boldsymbol{u}_h - \boldsymbol{u}_{g,h}$ by solving (69). Here we take $\omega = \pi$ and consider (65) with the source-solution pair

$$\boldsymbol{J} = \begin{pmatrix} -\pi^2 \sin(\pi y)\cos(\pi x) \\ 0 \end{pmatrix}, \quad \boldsymbol{u} = \begin{pmatrix} \sin(\pi y) \\ \sin(\pi x)\cos(\pi y) \end{pmatrix} \tag{137}$$

and a boundary condition given by $g := \boldsymbol{n} \times \boldsymbol{u}$ on $\partial\Omega$.

In Fig. 7 we plot the convergence curves corresponding to spline elements of various degrees $p \times p$ and $N \times N$ cells per patch. The results are similar to what was observed for the Poisson problem: the solutions converge with optimal rate $p+1$ as the grids are refined (again a rate of $p+2$ is observed for $= 2$) which confirms the numerical accuracy of our approach for the Maxwell problem combined with a geometric lifting technique for the Dirichlet boundary condition. These convergence rates can be justified by the approximation power of multipatch spline spaces established in [16] and the error analysis from Monk and Demkowicz [43] which establishes optimal convergence under the condition that the finite element spaces satisfy the discrete compactness property: for FEEC spaces the discrete compactness property follows from the existence of L^2 stable commuting projection operators (see Sect. 3.6 [2]), and for multipatch spaces this has been recently proven in [25]. Note that the convergence observed here is actually better than expected, since $H(\mathrm{curl})$ multipatch spline spaces of maximal degree p should only have p order accuracy [16].

5.5 Eigenvalue Problems

We next assess the accuracy of our CONGA approximation (76) for the curl-curl eigenvalue problem.

We test our discretization on the two domains shown in Fig. 1, and plot in Fig. 8 the amplitude of the first five eigenmodes, together with their positive eigenvalues. Here the eigenmodes are computed using spline elements of degree 6×6 and 56×56, resp. 20×20 cells per patch in the case of the curved L-shaped, resp. pretzel-shaped domain composed of 3, resp. 18 patches. On the former domain this corresponds to 9408 cells in total and 22,692 degrees of freedom for the broken space V_h^1, while on the latter domain it corresponds to 7200

cells and 23,400 degrees of freedom for V_h^1 (a higher value than for the L-shaped domain despite less cells, because of the duplication of boundary dofs at the patch interfaces).

In Fig. 9 we then plot the relative eigenvalue errors

$$e_{h,i} = \frac{|\lambda_i - \lambda_{h,i}|}{\max(\lambda_i, \lambda_{h,i})} \tag{138}$$

as a function of the eigenvalue index i, for degrees $p = 3$ and 5, and $N \times N$ cells per patch with $N = 2$, 4, 8 and 16. For the curved L-shaped domain we use as reference the eigenvalues provided as benchmark in [29, 30], and for the pretzel-shaped domain we use the eigenvalues computed using our CONGA scheme, with as many reliable digits as we could find using uniform patches with degree 6×6 and $N \times N$ cells per patch with $N \leq 20$ (this limit being imposed by the fact that we compute the matrix eigenmodes with Scipy's `eigsh` solver with a sparse LU decomposition).

This allows us to verify numerically that the discrete eigenvalues converge towards the exact ones, with smaller errors corresponding to the smoother eigenmodes visible in Fig. 8.

5.6 Magnetostatic Test-Cases

We next study the CONGA discretizations of the magnetostatic problems presented in Sect. 3.5: either the one for the problem with pseudo-vacuum boundary conditions (86) or the one with metallic boundary conditions (96).

To this end we consider a scalar dipole current source,

$$J_z = \psi_0 - \psi_1 \quad \text{where } \psi_m = \exp\Big(- \frac{\big((x - x_m)^2 + (y - y_m)^2\big)^2}{2\sigma^2} \Big) \tag{139}$$

in the pretzel-shaped domain, with $\sigma = 0.02$. We set the positive current pole at $x_0 = y_0 = 1$ and the negative one at $x_1 = y_1 = 2$. We then consider the discrete solvers described in Sects. 3.5.1 and 3.5.2 for the problems with pseudo-vacuum and metallic boundary conditions, respectively.

In Fig. 10 we plot the scalar source J_z together with the vector-valued $\mathbf{curl} J_z$ field, and for each of the boundary conditions, we plot in Fig. 11 fine solutions computed using the CONGA scheme on a mesh with 20×20 cells per patch (i.e. 7200 cells in total) and elements of degree 6×6 in each patch.

In Table 3 we then show the relative L^2 errors corresponding to coarser grids and lower spline degrees for both boundary conditions, using as reference the fine solutions shown in Fig. 11. We also plot in Fig. 12 the solutions corresponding to spline elements of degree 3×3 on each patch. Again these results indicate that our CONGA solutions converge nicely as the grids are refined, with smaller errors associated with higher polynomial degrees.

5.7 Time-Dependent Maxwell Equation

We finally assess the qualitative and quantitative properties of our mapped spline-based CONGA scheme for the time-dependent Maxwell system, using a leap-frog time stepping (108)–(109). We will consider two test-cases.

Our first test-case consists of an initial electric pulse

$$\boldsymbol{E}(t = 0) = \mathbf{curl}\psi, \quad \psi(\boldsymbol{x}) = \exp\Big(- \frac{\big((x - x_0)^2 + (y - y_0)^2\big)^2}{2\sigma^2} \Big) \tag{140}$$

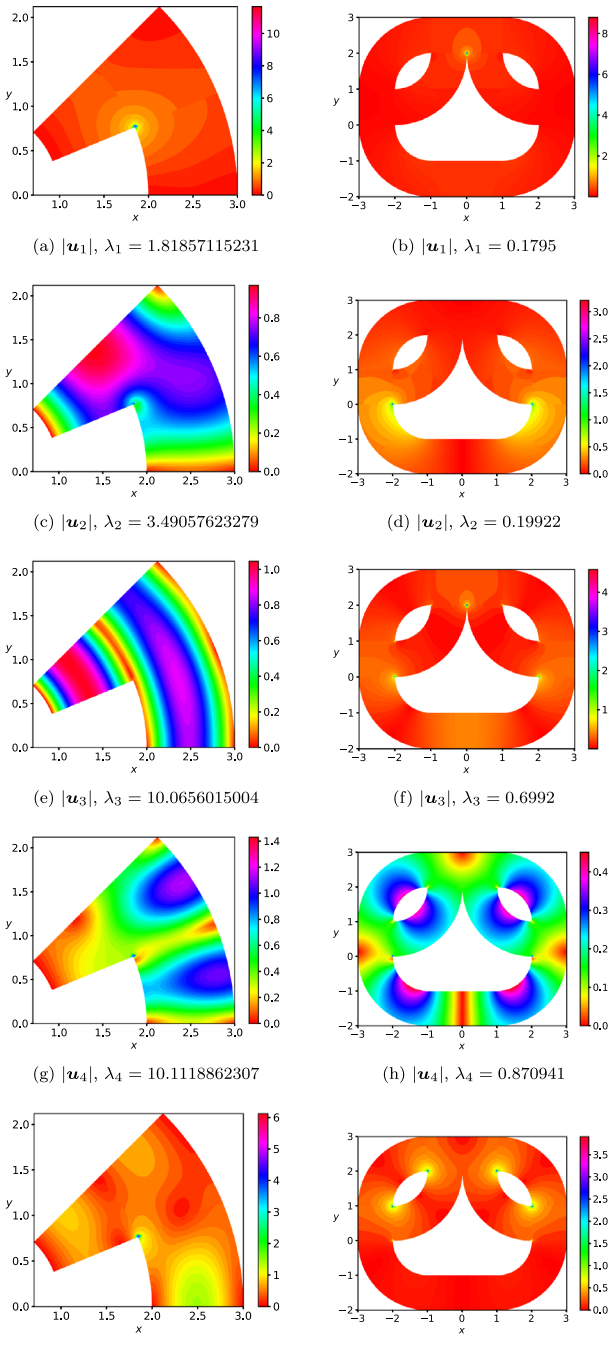

(a) $|\boldsymbol{u}_1|$, $\lambda_1 = 1.81857115231$ (b) $|\boldsymbol{u}_1|$, $\lambda_1 = 0.1795$

(c) $|\boldsymbol{u}_2|$, $\lambda_2 = 3.49057623279$ (d) $|\boldsymbol{u}_2|$, $\lambda_2 = 0.19922$

(e) $|\boldsymbol{u}_3|$, $\lambda_3 = 10.0656015004$ (f) $|\boldsymbol{u}_3|$, $\lambda_3 = 0.6992$

(g) $|\boldsymbol{u}_4|$, $\lambda_4 = 10.1118862307$ (h) $|\boldsymbol{u}_4|$, $\lambda_4 = 0.870941$

(i) $|\boldsymbol{u}_5|$ $\lambda_5 = 12\ 4355372484$ (j) $|\boldsymbol{u}_5|$ $\lambda_5 = 1\ 1945$

Fig. 8 Eigenmodes of the curl-curl problem on the curved-L-shaped domain (left) and on the pretzel domain (right), obtained on fine grids with 20×20 cells per patch and degree 6×6

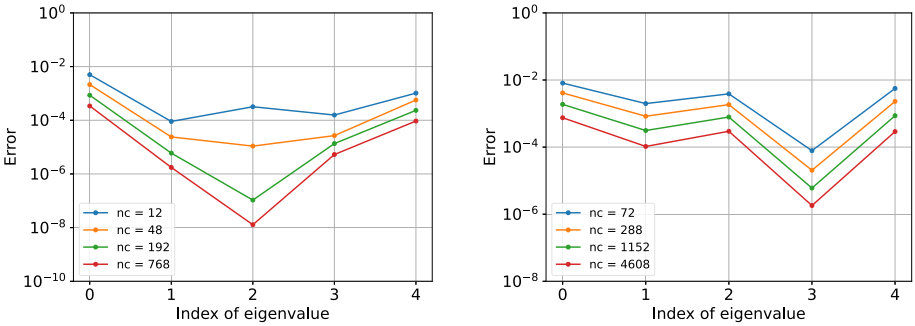

(a) curved L-shaped domain, $p = 3$ (b) pretzel domain, $p = 3$

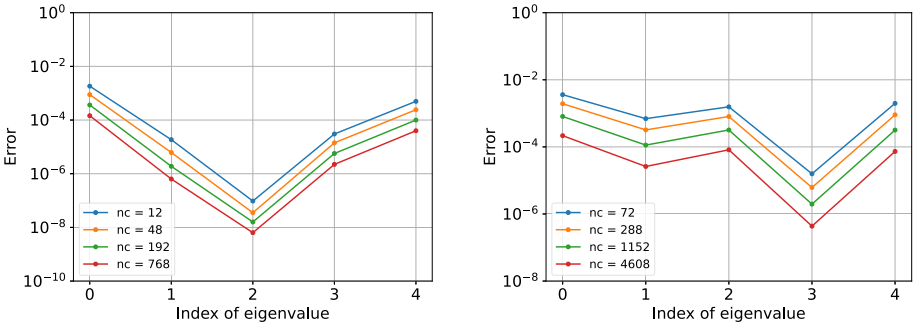

(c) curved L-shaped domain, $p = 5$ (d) pretzel domain, $p = 5$

Fig. 9 Relative eigenvalue errors (138) for the curl-curl problem on the curved-L-shaped domain (left) and on the pretzel domain (right), using elements of degree $p \times p$ as indicated, and $N \times N$ cells per patch with $N = 2, 4, 8$ and 16. The resulting total numbers of cells are $\mathtt{nc} = 3N^2$ and $18N^2$ for the respective multipatch domains

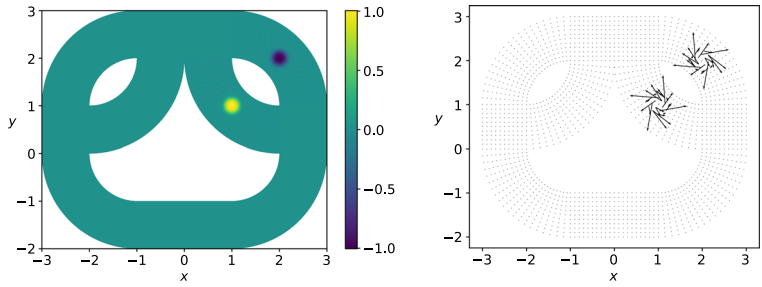

(a) J_z source (b) $\mathbf{curl}\, J_z$

Fig. 10 Source for the magnetostatic test-cases: the scalar current density (139) is plotted on the left panel and its vector-valued curl is shown on the right

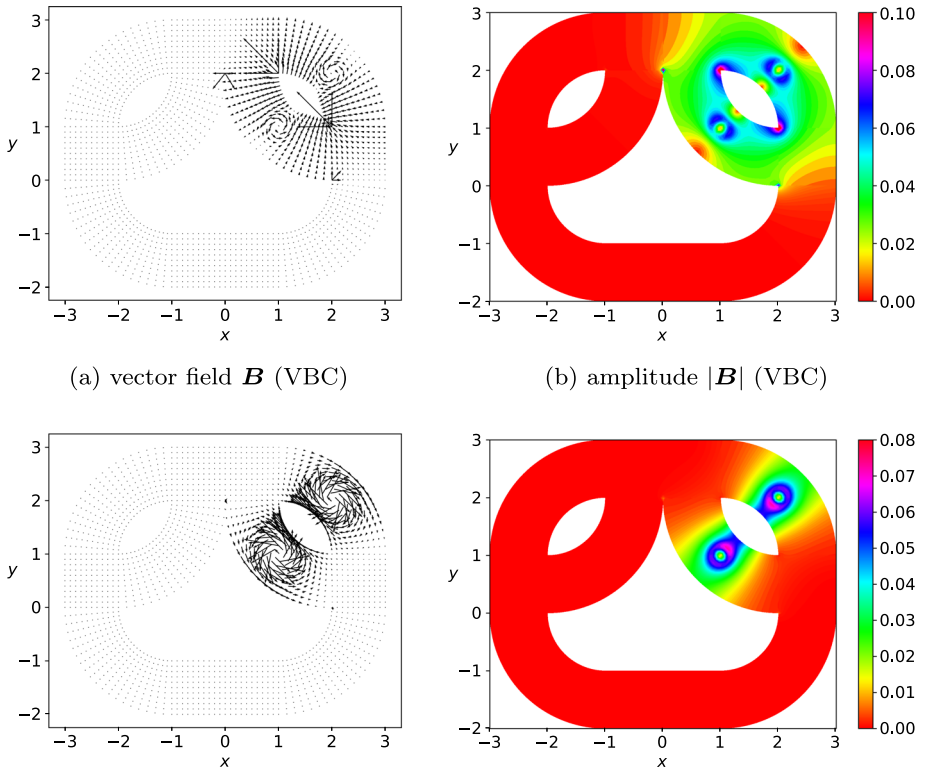

Fig. 11 Reference numerical solutions obtained with 20 × 20 cells per patch and elements of degree 6 × 6, for the magnetostatic test-cases with pseudo-vacuum (top) and metallic boundary conditions (bottom). The vector fields are shown on the left while the amplitudes are shown on the right

Table 3 L^2 errors for the $\boldsymbol{B}_h$ solutions of the magnetostatic test-cases with pseudo-vacuum and metallic boundary conditions, corresponding to the amplitude plots shown in Fig. 12. Here the errors are computed using numerical reference solutions obtained with 20 × 20 cells per patch and degree 6 × 6

Degree	2 × 2	3 × 3	4 × 4	5 × 5
Cells p.p.				
Errors for pseudo-vacuum boundary conditions				
2 × 2	0.23443	0.16028	0.10290	0.06425
4 × 4	0.10514	0.05855	0.05773	0.03029
8 × 8	0.03909	0.02414	0.01893	0.01542
16 × 16	0.018733	0.01193	0.008375	0.00567
Errors for metallic boundary conditions				
2 × 2	0.37023	0.24518	0.15902	0.09266
4 × 4	0.15490	0.07747	0.08660	0.03508
8 × 8	0.03776	0.01840	0.01736	0.01550
16 × 16	0.00544	0.00187	0.00153	0.00085

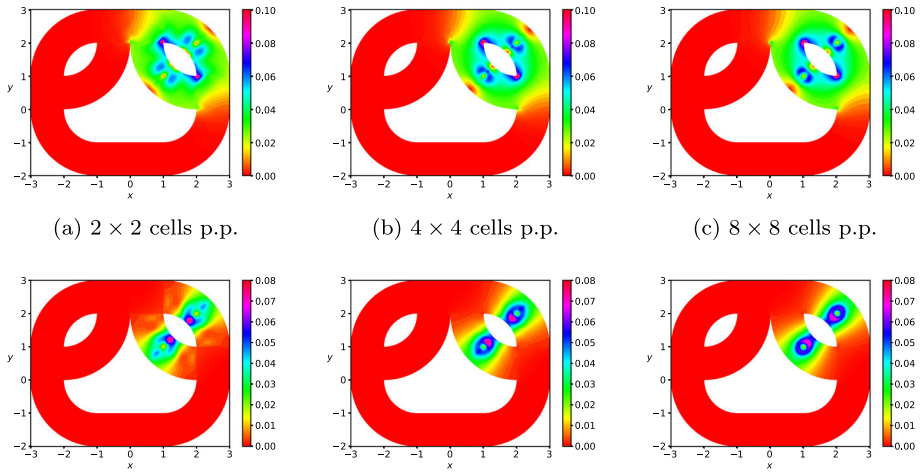

(a) 2×2 cells p.p. (b) 4×4 cells p.p. (c) 8×8 cells p.p.

(d) 2×2 cells p.p. (e) 4×4 cells p.p. (f) 8×8 cells p.p.

Fig. 12 Numerical solutions for the magnetostatic test-cases with pseudo-vacuum (top) and metallic boundary conditions (bottom), obtained with elements of degree 3×3 and different patch-wise grids, as indicated

in the pretzel-shaped domain, with $x_0 = y_0 = 1$ and $\sigma = 0.02$. The initial magnetic field and the source is

$$B(t = 0) = 0, \quad \text{and} \quad \boldsymbol{J}(t, \boldsymbol{x}) = 0. \tag{141}$$

In Fig. 13 we compare successive snapshots of two solutions corresponding to different numbers $N \times N$ of cells per patch and degrees $p \times p$: on the left plots the solution is computed with $N = 8$ and $p = 3$, while that on the right plots uses $N = 20$ and $p = 6$. We observe that these results display a qualitatively correct behaviour for propagating waves with reflecting boundary conditions, and that the profile for both resolutions are similar up to small scale features, which can be seen as a practical indicator of convergence.

Since this test-case is without source the discrete energy should be preserved up to bounded oscillations, as recalled in Sect. 3.6. In Fig. 14 we plot the time evolution of the discrete energy $\mathcal{H}_h(t^n) = \frac{1}{2}\big(\|\boldsymbol{E}_h^n\|^2 + \|B_h^n\|^2\big)$, together with that of the electric and magnetic fields, and we observe that the total energy is very stable. We also plot the amplitude of the discrete divergence as time evolves: assuming all computations exact it should be zero according to (106), indeed we have $\rho = \operatorname{div} \boldsymbol{E}(t = 0) = 0$ in this test case. On Fig. 14 we verify that it is zero up to machine accuracy and small quadrature errors.

We next study the quality of the source approximation operator $\boldsymbol{J} \to \boldsymbol{J}_h$ which is involved in the discrete Ampere equation (104). For this we use a second time-dependent test-case with a zero initial condition

$$\boldsymbol{E}(t = 0) = 0, \quad \text{and} \quad B(t = 0) = 0 \tag{142}$$

and a source of the form

$$\boldsymbol{J}(t) = \mathbf{curl}\psi - \cos(\omega t)\, \operatorname{grad} \psi \tag{143}$$

with ψ as in (140). The associated charge density is then

$$\rho(t) = -\int_0^t \operatorname{div} \boldsymbol{J}(t')\, \mathrm{d}t' = \omega^{-1} \sin(\omega t) \Delta \psi.$$

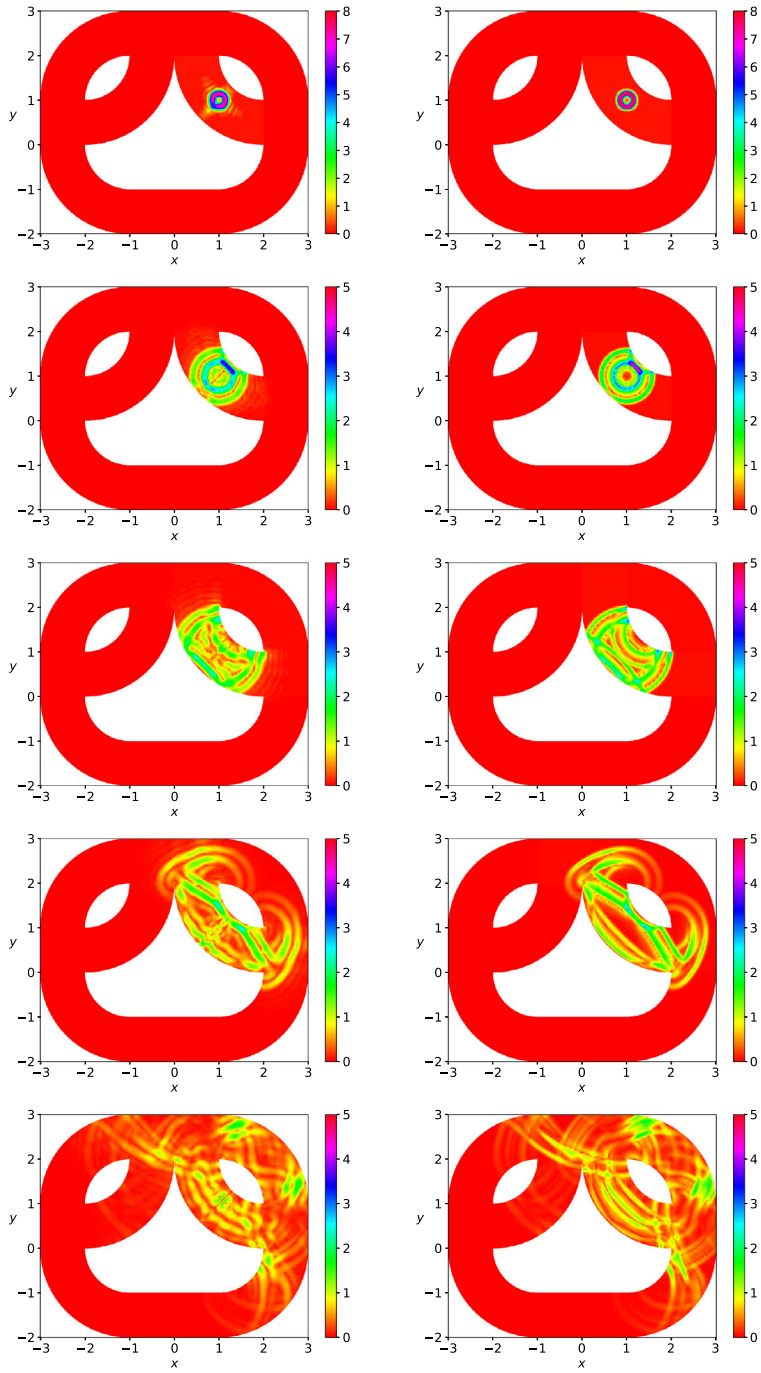

Fig. 13 Snapshots of numerical solutions to the time-dependent Maxwell test-case (140)–(141) at $t = 0, 0.4, 0.8, 1.6$ and 3.2 (from top to bottom) discretized with the CONGA method (104) using spline elements of degree $p \times p$ and $N \times N$ cells per patch, and a leap-frog time stepping. The solution on the left corresponds to $N = 8$ and $p = 3$, while the one on the right has been obtained $N = 20$ and $p = 6$

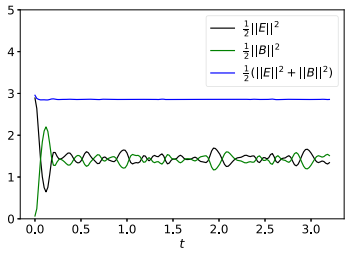

(a) Energy $\mathcal{H}_h(t^n)$ for $N = 8$, $p = 3$

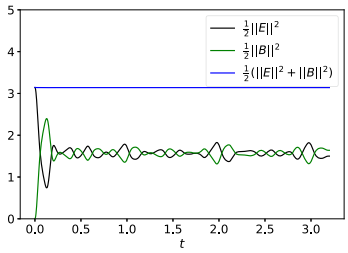

(b) Energy $\mathcal{H}_h(t^n)$ for $N = 20$, $p = 6$

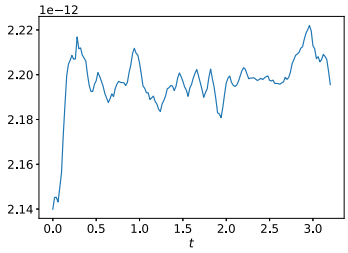

(c) $\|\widetilde{\mathrm{div}}_h \boldsymbol{E}_h(t^n)\|$ for $N = 8$, $p = 3$

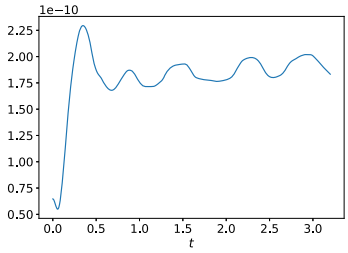

(d) $\|\widetilde{\mathrm{div}}_h \boldsymbol{E}_h(t^n)\|$ for $N = 20$, $p = 6$

Fig. 14 Energy (top) and discrete divergence amplitude (bottom) of the coarse (left) and fine (right) numerical solutions of the time-dependent Maxwell test-case (140)–(141) shown in Fig. 13

In Figs. 15 and 16 we compare three different approximation operators for the current source, namely:

(i) the primal finite element projection: $\boldsymbol{J}_h = \Pi_h^1 \boldsymbol{J}$,
(ii) the L^2 projection on the broken space: $\boldsymbol{J}_h = Q_{V_h^1} \boldsymbol{J}$,
(iii) the dual projection: $\boldsymbol{J}_h = \tilde{\Pi}_h^1 \boldsymbol{J}$

where we remind that $\tilde{\Pi}_h^1 = (P_h^1)^* Q_{V_h^1}$, see (32). We note that each of these projection operators are local, in the sense that none requires solving a global problem on the computational domain Ω. We also remind that the primal projection Π_h^1 interpolates the geometric (edge) degrees of freedom and satisfies a commuting diagram property with the primal (strong) differential operators, but not with the dual ones. Hence it does not allow to preserve the discrete electric Gauss law in (106). In contrast, both the L^2 projection on the broken space V_h^1 and the dual projection $\tilde{\Pi}_h^1$ guarantee the preservation of the discrete Gauss laws, however we expect an increased stability for the latter one as discussed in Remark 5.

In Fig. 15 we first show some snapshots of the three numerical solutions on a time range $t \in [0, T]$ with $T = 20$: There we see that the primal projection yields a very strong and steadily growing field in the region of the source (visible from the changing color scale) which points towards a large error. In contrast, the L^2 and the dual projections produce solutions with moderate amplitude with some visible differences, namely an electric field that also builds up in the region where the source is located.

To better analyse the quality of these simulations we next show in Fig. 16 two error indicators for each one of the numerical strategies described above, namely the Gauss law errors associated with the broken solution $\mathcal{G}_h^n(\boldsymbol{E}_h^n)$, and that of its conforming projection

$\mathcal{G}_h^n(P_h^1 \boldsymbol{E}_h^n)$, where we have denoted

$$\mathcal{G}_h^n(\boldsymbol{F}_h) = \|\widetilde{\mathrm{div}}_h \boldsymbol{F}_h - \tilde{\Pi}^0 \rho(t^n)\| \quad \text{for } \boldsymbol{F}_h \in V_h^1. \tag{144}$$

Here the former errors are expected to be zero for both the L^2 and dual projections, see Remark 5: The numerical results confirm this value, up to machine accuracy, whereas they show significant errors for the primal projection shown in the left plots. As for the second error, it has no reason to be strictly zero but should remain small for accurate and stable solutions, hence it is also an interesting error indicator. Here the curves show very large values (around 80 at $t = T$) for the primal projection operator Π_h^1, with a linear time growth (which is somehow consistent with the strong growth of the former error indicator $\mathcal{G}_h^n(\boldsymbol{E}_h^n)$). For the L^2 projection the error is smaller but it is far from being negligible (close to 3), and also grows linearly in time. In contrast, the error is much smaller (on the order of 0.01) for the dual projection $\tilde{\Pi}_h^1$, and it oscillates but does not seem to grow. These results tend to indicate that the growing field visible in Fig. 15 corresponds to a numerical error, and they highlight the improved stability of the CONGA scheme with a proper source approximation.

6 Conclusions

In this work we have extended the classical theory of finite element exterior calculus (FEEC) to mapped multipatch domains, using finite element spaces that are fully discontinuous across the patch interfaces. We refer to this approach as the "broken FEEC" or "CONGA" (COnforming/Non conforming GAlerkin) method. While the foundational theory relative to the solution of the Hodge–Laplace equation was presented in recent work [23], here we have presented stable broken FEEC formulations for many problems arising in electromagnetic applications, including Poisson's equation, time-dependent and time-harmonic (source and eigenvalue) Maxwell's problems, and magnetostatic problems with pseudo-vacuum and metallic boundary conditions. Further, we have detailed a numerical framework based on tensor-product splines on each patch, under the assumption of geometric conformity across the patch interfaces.

For all the electromagnetic problems presented, we have verified our broken FEEC framework through extensive numerical testing in L-shaped and pretzel-like two-dimensional domains. The latter geometry is particularly challenging because of its three holes and sharp reentrant corner. The nominal order of accuracy was achieved in all cases, and the structure-preserving properties (such as divergence of harmonic constraints) were respected to floating-point accuracy. For the time-dependent Maxwell problem with a current source, we could also observe long-term stability of the method, and presented alternative formulations which lack this property.

As explained in the introduction, the main benefit of our approach compared to a standard conforming FEEC discretization is to provide local coderivative operators, as well as local Hodge and commuting projection operators for both the primal and dual complexes. As such, broken FEEC methods allow for parallel algorithms where only communications between contiguous patches are needed in the direct application of every operator appearing in the primal/dual commuting diagram.

Another appealing feature of this approach lies in the modularity of the implementation: as every operator in the commuting diagram involves either a single patch operator or a conforming projection (which performs averages between contiguous patches and can be applied matrix-free), extending a single-patch code to multipatch domains essentially

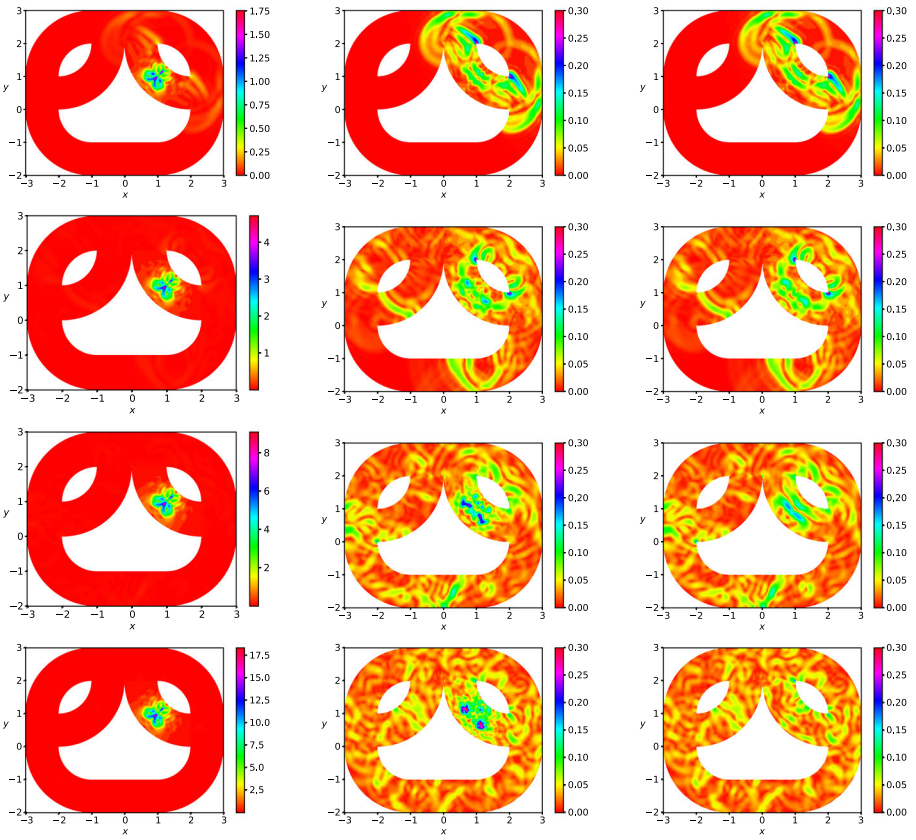

Fig. 15 Snapshots of numerical solutions to the time-dependent Maxwell problem with a time-varying source (143) discretized with the CONGA scheme (104) using spline elements of degree 3×3 and 8×8 cells per patch. The amplitudes $|P_h^1 \boldsymbol{E}_h^n|$ are shown at $t = 2$, 5, 10 and 20 (from top to bottom). In the left panels the source projection $\boldsymbol{J} \to \boldsymbol{J}_h$ is a primal projection operator Π_h^1 which does not commute with the dual differential operators (note the time-varying color scale). The middle panels use an orthogonal projection $Q_{V_h^1}$, and the ones on the right a dual commuting projection $\tilde{\Pi}_h^1$. See the text for more details

amounts to writing these conforming projections operators. In particular, solving problems in the broken multipatch spaces can be done with a global data structure that just consists of a list of the patch-wise data structures.

Given its solid theoretical bases and convincing numerical results, we are confident that the broken FEEC framework will find practical use in the computational physics community. To this end we plan to relax the grid conformity constraints at the interfaces, allowing for independent refinement of the patches, and to investigate the efficiency of parallel implementations for high-performance computing applications. This will allow us to tackle large problems in three dimensions, including MHD and kinetic models for plasma physics.

Acknowledgements The authors would like to thank Eric Sonnendrücker for inspiring discussions throughout this work.

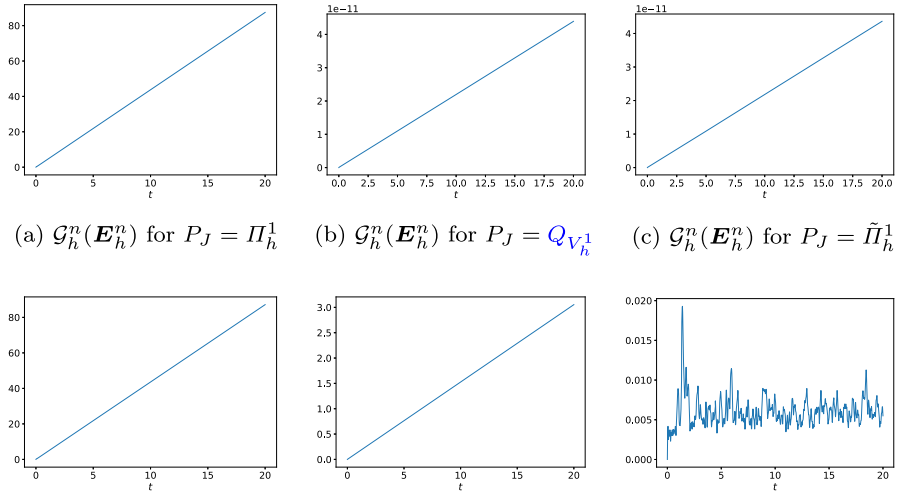

(a) $\mathcal{G}_h^n(\boldsymbol{E}_h^n)$ for $P_J = \Pi_h^1$ (b) $\mathcal{G}_h^n(\boldsymbol{E}_h^n)$ for $P_J = Q_{V_h^1}$ (c) $\mathcal{G}_h^n(\boldsymbol{E}_h^n)$ for $P_J = \tilde{\Pi}_h^1$

(d) $\mathcal{G}_h^n(P_h^1\boldsymbol{E}_h^n)$ for $P_J = \Pi_h^1$ (e) $\mathcal{G}_h^n(P_h^1\boldsymbol{E}_h^n)$ for $P_J = Q_{V_h^1}$ (f) $\mathcal{G}_h^n(P_h^1\boldsymbol{E}_h^n)$ for $P_J = \tilde{\Pi}_h^1$

Fig. 16 Discrete Gauss law errors (144) as a function of time for the test-case (142)–(143), using different approximation operators for the discrete source $\boldsymbol{J}_h = P_J\boldsymbol{J}$. The top panels show the errors relative to the broken field $\boldsymbol{E}_h$, whereas those on the bottom panels show the error relative to its conforming projection $P_h^1\boldsymbol{E}_h$. For each indicator, the left, middle and right plots correspond to the different source approximation operators shown in Fig. 15

Funding Open Access funding enabled and organized by Projekt DEAL. The work of Yaman Güçlü was partially supported by the European Council under the Horizon 2020 Project Energy oriented Centre of Excellence for computing applications—EoCoE, Project ID 676629.

Availability of Data and Materials The data used for this article has been described in Sect. 5. Otherwise missing data is available upon request.

Declarations

Conflict of interest The authors declare that they have no conflict of interest.

Open Access This article is licensed under a Creative Commons Attribution 4.0 International License, which permits use, sharing, adaptation, distribution and reproduction in any medium or format, as long as you give appropriate credit to the original author(s) and the source, provide a link to the Creative Commons licence, and indicate if changes were made. The images or other third party material in this article are included in the article's Creative Commons licence, unless indicated otherwise in a credit line to the material. If material is not included in the article's Creative Commons licence and your intended use is not permitted by statutory regulation or exceeds the permitted use, you will need to obtain permission directly from the copyright holder. To view a copy of this licence, visit http://creativecommons.org/licenses/by/4.0/.

Appendix

A Broken Multipatch Spline Complexes

In this appendix we detail the construction of broken spline complexes on 2D multipatch spaces.

A.1 De Rham Sequences in 2D

In 2D the de Rham sequence (1) may be reduced in two different ways, namely

$$V^0 \xrightarrow{\textbf{grad}} V^1 \xrightarrow{\text{curl}} V^2 \tag{A.1}$$

and

$$V^0 \xrightarrow{\textbf{curl}} V^1 \xrightarrow{\text{div}} V^2 \tag{A.2}$$

where **curl** and curl denote the vector and scalar-valued curl operators respectively (for clarity we use bold fonts to denote vector-valued fields and operators in the subsequent sections). Here the operators in the second sequence are dual to those in the first one, and in each case we may consider spaces with homogeneous boundary conditions, namely

$$V^0 = H_0^1(\Omega), \quad V^1 = \boldsymbol{H}_0(\text{curl}; \Omega), \quad V^2 = L^2(\Omega) \tag{A.3}$$

for the first sequence and

$$V^0 = H_0(\textbf{curl}; \Omega), \quad V^1 = \boldsymbol{H}_0(\text{div}; \Omega), \quad V^2 = L^2(\Omega) \tag{A.4}$$

for the second one, or the full inhomogeneous spaces

$$V^0 = H^1(\Omega), \quad V^1 = \boldsymbol{H}(\text{curl}; \Omega), \quad V^2 = L^2(\Omega), \tag{A.5}$$

and

$$V^0 = H(\textbf{curl}; \Omega), \quad V^1 = \boldsymbol{H}(\text{div}; \Omega), \quad V^2 = L^2(\Omega). \tag{A.6}$$

In the numerical examples presented in this article we will consider the first sequence (A.1) as the primal one, both with homogeneous spaces (A.3) or inhomogeneous ones (A.5). As mentioned in Sect. 3.3 this distinction only affects the conforming projection operators, indeed the broken spaces consist of local spaces which have no boundary conditions. This point is also discussed in Remark 6.

A.2 Reference Spline Complexes

On each mapped patch the local sequence (19) is built as the push-forward of tensor-product spline spaces defined on the reference patch $\hat{\Omega} =]0, 1[^2$ following [14, 15]. To simplify the construction of the conforming spaces $\{V_h^{\ell,c}\}_\ell$ over domains with non-trivial inter-patch connectivities, we consider a discretization which has reflectional and rotational symmetries over $\hat{\Omega}$. This amounts to using the same knot sequence along every dimension of $\hat{\Omega}$, and to require such a knot sequence to be left-right symmetric as explained below.

To construct the reference tensor-product spline complex with maximal coordinate degree $p \geq 1$ on a grid with N cells per dimension, we equip the interval $[0, 1]$ with an open knot

sequence

$$0 = \xi_0 = \cdots = \xi_p < \xi_{p+1} < \cdots < \xi_{n-1} < \xi_n = \cdots = \xi_{n+p} = 1 \tag{A.7}$$

where $n = N + p$. This sequence is assumed symmetric for simplicity, in the sense that $\xi_i = 1 - \xi_{n+p-i}$ for all i. For $i = 0, \ldots, n-1$ and $q \in \{p-1, p\}$ we then let $\mathcal{N}_i^q$ be the normalized B-spline of degree q associated with the knots $(\xi_i, \ldots, \xi_{i+q+1})$, see [48, Definition 4.19]. The spline space $\mathbb{S}_q = \mathbb{S}_q(\boldsymbol{\xi}) := \mathrm{Span}\{\mathcal{N}_i^q : i = 0, \ldots, n-1\}$ then corresponds to splines of maximal regularity on the given subdivision, namely

$$\mathbb{S}_q = \{v \in \mathcal{C}^{q-1}([0,1]) : v|_{(\xi_{q+j}, \xi_{q+j+1})} \in \mathbb{P}_q,\ \forall j = 0, \ldots, N-1\}.$$

Notice that here $\mathcal{N}_0^{p-1}$ vanishes identically; it is only kept in the formulas for notational simplicity. Tensor-product spline spaces of degree $\boldsymbol{q} \in \{p-1, p\}^2$ are then defined on the reference domain $\hat{\Omega}$ as

$$\mathbb{S}_{\boldsymbol{q}} := \mathrm{Span}\left\{\mathcal{N}_{\boldsymbol{i}}^{\boldsymbol{q}} : \boldsymbol{i} \in [\![0, n-1]\!]^2\right\} \quad \text{with} \quad \mathcal{N}_{\boldsymbol{i}}^{\boldsymbol{q}}(\hat{\boldsymbol{x}}) := \prod_{d=1}^{2} \mathcal{N}_{i_d}^{q_d}(\hat{x}_d). \tag{A.8}$$

The reference spline complex [14] associated with the **grad** − curl sequence (A.1) reads then

$$\hat{\mathbb{V}}^0 := \mathbb{S}_{(p,p)} \xrightarrow{\mathbf{grad}} \hat{\mathbb{V}}^1 := \begin{pmatrix} \mathbb{S}_{(p-1,p)} \\ \mathbb{S}_{(p,p-1)} \end{pmatrix} \xrightarrow{\mathrm{curl}} \hat{\mathbb{V}}^2 := \mathbb{S}_{(p-1,p-1)} \tag{A.9}$$

while the one associated to the **curl** − div sequence (A.2) reads

$$\hat{\mathbb{V}}^0 := \mathbb{S}_{(p,p)} \xrightarrow{\mathbf{curl}} \hat{\mathbb{V}}^1 := \begin{pmatrix} \mathbb{S}_{(p,p-1)} \\ \mathbb{S}_{(p-1,p)} \end{pmatrix} \xrightarrow{\mathrm{div}} \hat{\mathbb{V}}^2 := \mathbb{S}_{(p-1,p-1)}. \tag{A.10}$$

A.3 Broken FEEC Spaces on the Mapped Patches

Following Monk and Demkowicz [35], Buffa et al. [15] and Perse et al. [46] we define the local spaces (19) on the mapped patches $\Omega_k = F_k(\hat{\Omega})$ as push-forwards of the reference spline spaces, namely

$$V_h^\ell(\Omega_k) := \mathcal{F}_k^\ell(\hat{\mathbb{V}}^\ell) \tag{A.11}$$

where the push-forward transforms associated with a mapping F_k are obtained as the 2D reduction of the usual ones in 3D. For the **grad** − curl sequence (A.1) they read

$$\begin{cases} \mathcal{F}_k^0 : \hat{v} \mapsto v := \hat{v} \circ F_k^{-1} \\ \mathcal{F}_k^1 : \hat{\boldsymbol{v}} \mapsto \boldsymbol{v} := \left(DF_k^{-T}\hat{\boldsymbol{v}}\right) \circ F_k^{-1} \\ \mathcal{F}_k^2 : \hat{v} \mapsto v := \left(J_{F_k}^{-1}\hat{v}\right) \circ F_k^{-1} \end{cases} \tag{A.12}$$

and for the **curl** − div sequence (A.2) they read

$$\begin{cases} \mathcal{F}_k^0 : \hat{v} \mapsto v := \hat{v} \circ F_k^{-1} \\ \mathcal{F}_k^1 : \hat{\boldsymbol{v}} \mapsto \boldsymbol{v} := \left(J_{F_k}^{-1} DF_k \hat{\boldsymbol{v}}\right) \circ F_k^{-1} \\ \mathcal{F}_k^2 : \hat{v} \mapsto v := \left(J_{F_k}^{-1}\hat{v}\right) \circ F_k^{-1} \end{cases} \tag{A.13}$$

We remind that $DF_k = \left(\partial_b (F_k)_a(\hat{\boldsymbol{x}})\right)_{1 \le a,b \le 2}$ denotes the Jacobian matrix of F_k, and J_{F_k} its (positive) metric determinant corresponding to the surface measure for two-dimensional

manifolds in $\mathbb{R}^3$, see e.g. [16, 35, 37, 41]. The inverse transforms $(\mathcal{F}_k^\ell)^{-1}$ are called pull-backs, and a fundamental property of these transforms is that they commute with the differential operators [31, 35], namely

$$(\mathcal{F}_k^{\ell+1})^{-1}(d^\ell) = \hat{d}^\ell (\mathcal{F}_k^\ell)^{-1} \tag{A.14}$$

holds with (d^0, d^1) the differential operators in the sequences (A.1) or (A.2), and $(\hat{d}^0, \hat{d}^1)$ their counterparts on the logical (reference) domain. As these transforms are linear operators, the local spaces are spanned by the push-forwarded basis functions. In particular, setting

$$\Lambda_{k,\mu}^\ell := \begin{cases} \mathcal{F}_k^\ell(\hat{\Lambda}_\mu^\ell) & \text{on } \Omega_k \\ 0 & \text{on } \Omega \setminus \Omega_k \end{cases} \qquad \text{for } (k,\mu) \in [\![1, K]\!] \times \hat{\mathcal{M}}^\ell \tag{A.15}$$

provides us with local bases for the global broken spaces (20), i.e.,

$$V_h^\ell = \mathrm{Span}\{\Lambda_{k,\mu}^\ell : (k,\mu) \in \mathcal{M}_h^\ell\} \quad \text{where} \quad \mathcal{M}_h^\ell := [\![1, K]\!] \times \hat{\mathcal{M}}^\ell. \tag{A.16}$$

B Broken Geometric Degrees of Freedom

Using the notation introduced in Sect. A we now detail the geometric degrees of freedom involved in our broken FEEC diagram (131).

B.1 Geometric Degrees of Freedom on the Reference Patch

Following Bochev et al. [4], Robidoux [47], Gerritsma [31], Campos Pinto et al. [24] we equip the reference complexes (A.9) and (A.10) with geometric degrees of freedom which are known to commute with the differential operators. They are based on an interpolation grid

$$0 = \zeta_0 < \cdots < \zeta_{n-1} = 1$$

for the univariate spline space $\mathbb{S}_p$ in the sense of [48, Th. 4.61], that is also symmetric, namely $\zeta_i = 1 - \zeta_{n-1-i}$ for all $i = 0, \ldots, n-1$. Here the usual choice is to consider Greville points associated with the knots (A.7). On the reference domain $\hat{\Omega}$ we then consider the interpolatory nodes, edges and cells

$$\begin{cases} \hat{\mathrm{n}}_{\boldsymbol{i}} := (\zeta_{i_1}, \zeta_{i_2}) & \text{for } \boldsymbol{i} \in \hat{\mathcal{M}}^0 \\ \hat{\mathrm{e}}_{d,\boldsymbol{i}} := [\hat{\mathrm{n}}_{\boldsymbol{i}}, \hat{\mathrm{n}}_{\boldsymbol{i}+\boldsymbol{e}_d}] & \text{for } (d,\boldsymbol{i}) \in \hat{\mathcal{M}}^1 \\ \hat{\mathrm{c}}_{\boldsymbol{i}} := [\hat{\mathrm{e}}_{1,\boldsymbol{i}}, \hat{\mathrm{e}}_{1,\boldsymbol{i}+\boldsymbol{e}_2}] = \displaystyle\prod_{1 \le d \le 2} [\zeta_{i_d}, \zeta_{i_d+1}] & \text{for } \boldsymbol{i} \in \hat{\mathcal{M}}^2. \end{cases} \tag{B.1}$$

Here the square brackets $[\cdot]$ denote convex hulls, $\boldsymbol{e}_d$ is the canonical basis vector of $\mathbb{R}^2$ along dimension d and the multi-index sets read

$$\begin{cases} \hat{\mathcal{M}}^0 := \{\boldsymbol{i} : \boldsymbol{i} \in [\![0, n-1]\!]^2\} \\ \hat{\mathcal{M}}^1 := \{(d,\boldsymbol{i}) : d \in [\![1,2]\!], \boldsymbol{i} \in [\![0, n-1]\!]^2, i_d + 1 < n\} \\ \hat{\mathcal{M}}^2 := \{\boldsymbol{i} : \boldsymbol{i} \in [\![0, n-2]\!]^2\}. \end{cases}$$

Geometric degrees of freedom associated with the **grad** − curl sequence (A.1) are then defined as the linear forms

$$\begin{cases} \hat{\sigma}^0_{\boldsymbol{i}}(v) := v(\hat{\mathrm{n}}_{\boldsymbol{i}}) & \text{for } \boldsymbol{i} \in \hat{\mathcal{M}}^0 \\ \hat{\sigma}^1_{d,\boldsymbol{i}}(\boldsymbol{v}) := \displaystyle\int_{\hat{\mathrm{e}}_{d,\boldsymbol{i}}} \boldsymbol{v} \cdot \boldsymbol{e}_d & \text{for } (d,\boldsymbol{i}) \in \hat{\mathcal{M}}^1 \\ \hat{\sigma}^2_{\boldsymbol{i}}(v) := \displaystyle\int_{\hat{\mathrm{c}}_{\boldsymbol{i}}} v & \text{for } \boldsymbol{i} \in \hat{\mathcal{M}}^2 \end{cases} \tag{B.2}$$

where we observe that the reference edges are oriented according to their natural parametrization,

$$\hat{\boldsymbol{x}}^{\mathrm{e}}_{d,\boldsymbol{i}}(s) := \hat{\mathrm{n}}_{\boldsymbol{i}} + (s - \zeta_{i_d})\boldsymbol{e}_d \quad \text{for } s \in [\zeta_{i_d}, \zeta_{i_d+1}]. \tag{B.3}$$

For the **curl** − div sequence (A.2) we define $\hat{\sigma}^0_{\boldsymbol{i}}$ and $\hat{\sigma}^2_{\boldsymbol{i}}$ similarly, while the intermediate degrees of freedom are modified such that

$$\hat{\sigma}^1_{d,\boldsymbol{i}}(\boldsymbol{v}) := \int_{\hat{\mathrm{e}}_{d,\boldsymbol{i}}} \boldsymbol{v} \cdot \boldsymbol{e}_d^{\perp} \quad \text{for } (d,\boldsymbol{i}) \in \hat{\mathcal{M}}^1, \tag{B.4}$$

where $\boldsymbol{e}_d^{\perp} := (\boldsymbol{e}_2, -\boldsymbol{e}_1)^T$ corresponds to a $\pi/2$ rotation (counterclockwise) of the basis vector $\boldsymbol{e}_d$. As these degrees of freedom are unisolvent we let $\hat{\Lambda}^{\ell}_{\mu}, \mu \in \hat{\mathcal{M}}^{\ell}$, be the *geometric basis* for the spline space $\hat{\mathbb{V}}^{\ell}$, characterized by the duality relations

$$\hat{\sigma}^{\ell}_{\mu}(\hat{\Lambda}^{\ell}_{\nu}) = \delta_{\mu,\nu} \quad \text{for} \quad \mu, \nu \in \hat{\mathcal{M}}^{\ell}. \tag{B.5}$$

Because the degrees of freedom $\hat{\sigma}^0_{\mu}$ are based on point values they cannot be applied to general functions in $H^1(\hat{\Omega})$, indeed this space contains discontinuous and even unbounded functions. Similarly the degrees of freedom $\hat{\sigma}^1_{\mu}$ are not well-defined on $H(\mathrm{curl};\hat{\Omega})$ since functions in this space may not have tangential traces on local edges. Thus we are in the situation described in Remark 1 where the degrees of freedom are not well-defined on the sequence

$$\hat{V}^0 := H^1(\hat{\Omega}) \xrightarrow{\mathbf{grad}} \hat{V}^1 := H(\mathrm{curl};\hat{\Omega}) \xrightarrow{\mathrm{curl}} \hat{V}^2 := L^2(\hat{\Omega}). \tag{B.6}$$

Hence, we need to specify some proper domain spaces.

Proposition B.1 *The reference degrees of freedom $\hat{\sigma}^{\ell}_{\mu}$ are well defined on the domain spaces $\hat{U}^{\ell} := \hat{V}^{\ell} \cap \hat{U}^{\ell}_{L^1}$, where we have set*

$$\hat{U}^0_{L^1} := W^1_{1,2}(\hat{\Omega}) \xrightarrow{\mathbf{grad}} \hat{U}^1_{L^1} := \begin{pmatrix} W^1_2(\hat{\Omega}) \\ W^1_1(\hat{\Omega}) \end{pmatrix} \xrightarrow{\mathrm{curl}} \hat{U}^2_{L^1} := L^1(\hat{\Omega}) \tag{B.7}$$

for the **grad** − curl *sequence* (A.1)*, and*

$$\hat{U}^0_{L^1} := W^1_{1,2}(\hat{\Omega}) \xrightarrow{\mathbf{curl}} \hat{U}^1_{L^1} := \begin{pmatrix} W^1_1(\hat{\Omega}) \\ W^1_2(\hat{\Omega}) \end{pmatrix} \xrightarrow{\mathrm{div}} \hat{U}^2_{L^1} := L^1(\hat{\Omega}) \tag{B.8}$$

for the **curl** − div *sequence* (A.2)*, with anisotropic Sobolev spaces defined as $W^1_{1,2}(\hat{\Omega}) := \{v \in L^1(\hat{\Omega}) : \partial_1\partial_2 v \in L^1(\hat{\Omega})\}$ and $W^1_d(\hat{\Omega}) := \{v \in L^1(\hat{\Omega}) : \partial_d v \in L^1(\hat{\Omega})\}$ for $d \in \{1,2\}$.*

Moreover they commute with the local differential operators, namely we have

$$\hat{\sigma}_{\mu}^{\ell+1}(d^{\ell}v) = \sum_{\nu\in\hat{\mathcal{M}}^{\ell}} \hat{D}^{\ell}_{\mu,\nu}\hat{\sigma}^{\ell}_{\nu}(v) \quad \forall\, v\in\hat{U}^{\ell}, \quad \forall\, \mu\in\hat{\mathcal{M}}^{\ell}, \tag{B.9}$$

with graph-incidence Kronecker-product matrices $\hat{D}^{\ell}$.

Proof Nodal degrees of freedom $\hat{\sigma}^0_\mu$ are well defined on $\hat{U}^0_{L^1} = W^1_{1,2}(\hat{\Omega})$ because this space is continuously imbedded in $C^0(\hat{\Omega})$: this can be verified using Remarks 9 and 13 from Brezis [12, Sect. 9], and a density argument. Next we observe that edge degrees of freedom (B.2) along horizontal edges $\mathrm{e}_{1,\boldsymbol{i}}$ are of the form

$$\hat{\sigma}_{1,\boldsymbol{i}}(\boldsymbol{v}) = \int_{\zeta_{i_1+1}}^{\zeta_{i_1}} v_1(x',\zeta_{i_2})\,\mathrm{d}x' = \phi(\zeta_{i_1+1},\zeta_{i_2}) - \phi(\zeta_{i_1},\zeta_{i_2})$$

where $\phi(x,y) := \int_0^x v_1(x',y)\,\mathrm{d}x'$. If $v_1 \in W^1_2(\hat{\Omega})$, then we see that both ϕ and $\partial_1\partial_2\phi = \partial_2 v_1$ are in $L^1(\hat{\Omega})$, hence $\phi \in W^1_{1,2}(\hat{\Omega}) \subset C^0(\hat{\Omega})$, in particular $\hat{\sigma}_{1,\boldsymbol{i}}$ is indeed well defined on $\hat{U}^1_{L^1}$. Similarly we see that $\hat{\sigma}_{2,\boldsymbol{i}}$ is also well defined on $\hat{U}^1_{L^1}$, and the other degrees of freedom are analyzed with the same reasoning. We also verify easily that in both cases, namely (B.7) and (B.8), the spaces $\hat{U}^{\ell}_{L^1}$ form a de Rham sequence. Taking the intersection with (B.6) thus yields a subsequence $\hat{U}^{\ell} \subset \hat{V}^{\ell}$ where the degrees of freedom are indeed well-defined. As for the commuting property, it is well known and follows from the Stokes formula, see e.g. [4]. We refer to [24] for a description of the graph-incidence and Kronecker-product structure of the matrices $\hat{D}^{\ell}$. □

B.2 Geometric Degrees of Freedom on the Mapped Patches

In connection with the multipatch structure of V_h^{ℓ} we define broken degrees of freedom using pull-back transforms, which are the inverse of the push-forward operators (A.12) or (A.13), to obtain

$$\sigma^{\ell}_{k,\mu}(v) := \hat{\sigma}^{\ell}_{\mu}\big((\mathcal{F}^{\ell}_k)^{-1}(v|_{\Omega_k})\big) \quad \text{for } (k,\mu)\in\mathcal{M}^{\ell}_h. \tag{B.10}$$

By construction these degrees of freedom are in duality with the local basis functions (A.15), i.e.

$$\sigma^{\ell}_{k,\mu}(\Lambda^{\ell}_{l,\nu}) = \delta_{(k,\mu),(l,\nu)} \quad \text{for} \quad (k,\mu),(l,\nu)\in\mathcal{M}^{\ell}_h. \tag{B.11}$$

A key feature of the pull-back operators is to carry the geometric nature of the reference degrees of freedom to the mapped elements. For $\ell = 0$ the degrees of freedom simply consist of pointwise evaluations on the mapped nodes, i.e.

$$\sigma^0_{k,\boldsymbol{i}}(v) = v|_{\Omega_k}(\mathrm{n}_{k,\boldsymbol{i}}) \quad \text{with} \quad \mathrm{n}_{k,\boldsymbol{i}} := F_k(\hat{\mathrm{n}}_{\boldsymbol{i}}). \tag{B.12}$$

For $\ell = 1$ with the **grad** − curl sequence (A.1), they correspond to line integrals along the mapped edges $\mathrm{e}_{k,\mu} := F_k(\hat{\mathrm{e}}_\mu)$ with $\mu = (d,\boldsymbol{i}) \in \hat{\mathcal{M}}^1$. Specifically, using the pull-back $\hat{\boldsymbol{v}}_k := (\mathcal{F}^1_k)^{-1}(\boldsymbol{v}|_{\Omega_k}) = DF_k^T(\boldsymbol{v}|_{\Omega_k}\circ F_k)$ from (A.12) and the parametrization (B.3), we have

$$\sigma^1_{k,\mu}(\boldsymbol{v}) = \int_{\zeta_{i_d}}^{\zeta_{i_d+1}} \big(\boldsymbol{v}|_{\Omega_k}(F_k(\hat{\boldsymbol{x}}^{\mathrm{e}}_\mu(s)))\big)\cdot\big(DF_k(\hat{\boldsymbol{x}}^{\mathrm{e}}_\mu(s))\boldsymbol{e}_d\big)\,\mathrm{d}s = \int_{\mathrm{e}_{k,\mu}} \boldsymbol{v}|_{\Omega_k}\cdot\boldsymbol{\tau} \tag{B.13}$$

where $\boldsymbol{\tau}$ is the unit vector tangent to $\Subset_{k,\mu}$ with the orientation inherited from that of $\hat{\Subset}_\mu$, as mapped by F_k: at $\boldsymbol{x} = \boldsymbol{x}^{\Subset}_{k,\mu}(s) = F_k(\hat{\boldsymbol{x}}^{\Subset}_\mu(s))$ it reads

$$\boldsymbol{\tau}(\boldsymbol{x}) = \frac{\tilde{\boldsymbol{\tau}}(s)}{\|\tilde{\boldsymbol{\tau}}(s)\|} \quad \text{with} \quad \tilde{\boldsymbol{\tau}}(s) := \frac{\partial \boldsymbol{x}^{\Subset}_{k,\mu}}{\partial s}(s) = DF_k(\hat{\boldsymbol{x}}^{\Subset}_\mu(s))\boldsymbol{e}_d. \tag{B.14}$$

According to the interpatch conformity assumption (114)–(115), we observe that the relation

$$\frac{\partial \boldsymbol{x}^{\Subset}_{k,\mu}}{\partial s}(s) = \varepsilon^{\Subset}(k,\mu;l,\nu)\frac{\partial \boldsymbol{x}^{\Subset}_{l,\nu}}{\partial s}(\theta_{k,l}(s)) \tag{B.15}$$

holds with a constant $\varepsilon^{\Subset}(k,\mu;l,\nu) = \pm 1$ corresponding to the relative orientation of the edges $\Subset_{k,\mu}$ and $\Subset_{l,\nu}$.

For $\ell = 1$ in the **curl** − div sequence (A.2), the pull-back corresponding to (A.13) reads $\hat{\boldsymbol{v}}_k := (\mathcal{F}^1_k)^{-1}(\boldsymbol{v}|_{\Omega_k}) = J_{F_k} DF_k^{-1}(\boldsymbol{v}|_{\Omega_k} \circ F_k)$, so that (B.4) gives

$$\sigma^1_{k,\mu}(\boldsymbol{v}) = \int_{\zeta_{i_d}}^{\zeta_{i_d+1}} \left(\boldsymbol{v}|_{\Omega_k}(F_k(\hat{\boldsymbol{x}}^{\Subset}_\mu(s))\right) \cdot \left(J_{F_k} DF_k^{-T}(\hat{\boldsymbol{x}}^{\Subset}_\mu(s))\boldsymbol{e}^{\perp}_d\right) \mathrm{d}s = \int_{\Subset_{k,\mu}} \boldsymbol{v}|_{\Omega_k} \cdot \boldsymbol{\tau}^{\perp} \tag{B.16}$$

where $\boldsymbol{\tau}^{\perp}$ is the result of a $\pi/2$ rotation (counterclockwise) of the unit tangent vector (B.14), and reads

$$\boldsymbol{\tau}^{\perp} = \frac{\tilde{\boldsymbol{\tau}}^{\perp}(s)}{\|\tilde{\boldsymbol{\tau}}(s)\|} \quad \text{with} \quad \tilde{\boldsymbol{\tau}}^{\perp}(s) = J_{F_k} DF_k^{-T}(\hat{\boldsymbol{x}}^{\Subset}_\mu(s))\boldsymbol{e}^{\perp}_d. \tag{B.17}$$

Finally for $\ell = 2$ the degrees of freedom are the integrals on the mapped cells,

$$\sigma^2_{k,\boldsymbol{i}}(v) = \int_{\hat{\mathrm{c}}_{\boldsymbol{i}}} \left(v|_{\Omega_k}(F_k(\hat{\boldsymbol{x}})\right) J_{F_k}(\hat{\boldsymbol{x}})\,\mathrm{d}\hat{\boldsymbol{x}} = \int_{\mathrm{c}_{k,\boldsymbol{i}}} v|_{\Omega_k} \quad \text{with} \quad \mathrm{c}_{k,\boldsymbol{i}} := F_k(\hat{\mathrm{c}}_{\boldsymbol{i}}). \tag{B.18}$$

Proposition B.2 *The broken degrees of freedom $\sigma^\ell_{k,\mu}$ are well defined on the local domain spaces*

$$U^\ell(\Omega_k) := \mathcal{F}^\ell_k(\hat{U}^\ell) = \{v \in V^\ell(\Omega_k) : (\mathcal{F}^\ell_k)^{-1}(v) \in \hat{U}^\ell\} \tag{B.19}$$

which involve the spaces $\hat{U}^\ell$ from (B.7) and (B.8), and form local de Rham sequences. Moreover these degrees of freedom commute with the local differential operators. Namely, (29) holds on $U^\ell(\Omega_k)$ with the coefficients $D^\ell_{k,\mu,\nu} = \hat{D}^\ell_{\mu,\nu}$ from Proposition B.1 which are independent of the mapping F_k.

Proof The first statement is a direct consequence of the definition (B.10) and Proposition B.1. In particular the fact that the spaces (B.19) form a sequence follows from the similar property of the reference spaces and the commutation (A.14) of the pull-backs. As for the local commuting property, it also follows from (A.14) and the similar property (B.9) of the reference degrees of freedom, indeed

$$\begin{aligned}\sigma^{\ell+1}_{k,\mu}(d^\ell v) &= \hat{\sigma}^{\ell+1}_\mu((\mathcal{F}^{\ell+1}_k)^{-1}(d^\ell v)) = \hat{\sigma}^{\ell+1}_\mu(\hat{d}^\ell(\mathcal{F}^\ell_k)^{-1}v) \\ &= \sum_{\nu\in\hat{\mathcal{M}}^\ell} \hat{D}^\ell_{\mu,\nu}\hat{\sigma}^\ell_\nu((\mathcal{F}^\ell_k)^{-1}v) = \sum_{\nu\in\hat{\mathcal{M}}^\ell} \hat{D}^\ell_{\mu,\nu}\sigma^\ell_{k,\nu}(v).\end{aligned}$$

□

References

1. Arnold, D.N., Falk, R.S., Winther, R.: Finite element exterior calculus, homological techniques, and applications. Acta Numerica **15**, 1–155 (2006)
2. Arnold, D.N., Falk, R.S., Winther, R.: Finite element exterior calculus: from Hodge theory to numerical stability. Bull. Am. Math. Soc. (NS) **47**(2), 281–354 (2010)
3. Assous, F., Ciarlet, P., Labrunie, S.: Mathematical Foundations of Computational Electromagnetism. Springer (2018)
4. Bochev, P.B., Hyman, J.M.: Principles of mimetic discretizations of differential operators. In: Compatible Spatial Discretizations. Papers Presented at IMA Hot Topics Workshop: Compatible Spatial Discretizations for Partial Differential Equations, Minneapolis, MN, USA, May 11–15, 2004, pp. 89–119. Springer, New York (2006)
5. Boffi, D., Brezzi, F., Fortin, M.: Mixed Finite Element Methods and Applications, Volume 44 of Springer Series in Computational Mathematics. Springer (2013)
6. Boffi, D.: Finite element approximation of eigenvalue problems. Acta Numer. **19**, 1–120 (2010)
7. Boffi, D., Fernandes, P., Gastaldi, L., Perugia, I.: Computational models of electromagnetic resonators: analysis of edge element approximation. SIAM J. Numer. Anal. **36**(4), 1264–1290 (1999)
8. Bonazzoli, M., Rapetti, F.: High-order finite elements in numerical electromagnetism: degrees of freedom and generators in duality. Numer. Algorithms **74**(1), 111–136 (2016)
9. Bossavit, A.: Mixed finite elements and the complex of Whitney forms. In: The Mathematics of Finite Elements and Applications. VI (Uxbridge, 1987), pp. 137–144. Academic Press, London (1988)
10. Bossavit, A.: Solving Maxwell equations in a closed cavity, and the question of 'spurious modes'. IEEE Trans. Magn. **26**(2), 702–705 (1990)
11. Bossavit, A.: Computational Electromagnetism: Variational Formulations, Complementarity, Edge Elements. Academic Press (1998)
12. Brezis, H.: Functional Analysis, Sobolev Spaces and Partial Differential Equations. Springer (2010)
13. Buffa, A., Vázquez, R.H., Sangalli, G., Beirão da Veiga, L.: Approximation estimates for isogeometric spaces in multipatch geometries. Numer. Methods Part. Differ. Equ. **31**(2), 422–438 (2015)
14. Buffa, A., Sangalli, G., Vázquez, R.: Isogeometric analysis in electromagnetics: B-splines approximation. Comput. Methods Appl. Mech. Eng. **199**(17), 1143–1152 (2010)
15. Buffa, A., Rivas, J., Sangalli, G., Vázquez, R.: Isogeometric discrete differential forms in three dimensions. SIAM J. Numer. Anal. **49**, 818–844 (2011)
16. Buffa, A., Dölz, J., Kurz, S., Schöps, S., Vázquez, R., Wolf, F.: Multipatch approximation of the de Rham sequence and its traces in isogeometric analysis. Numer. Math. **144**(1), 201–236 (2019)
17. Campos Pinto, M.: Constructing exact sequences on non-conforming discrete spaces. Compt. Rendus Math. **354**(7), 691–696 (2016)
18. Campos Pinto, M., Sonnendrücker, E.: Gauss-compatible Galerkin schemes for time-dependent Maxwell equations. Math. Comput. **85**, 2651–2685 (2016)
19. Campos Pinto, M., Sonnendrücker, E.: Compatible Maxwell solvers with particles I: conforming and non-conforming 2D schemes with a strong Ampere law. SMAI J. Comput. Math. **3**, 53–89 (2017)
20. Campos Pinto, M., Sonnendrücker, E.: Compatible Maxwell solvers with particles II: conforming and non-conforming 2D schemes with a strong Faraday law. SMAI J. Comput. Math. **3**, 91–116 (2017)
21. Campos Pinto, M., Jund, S., Salmon, S., Sonnendrücker, E.: Charge-conserving FEM-PIC schemes on general grids. Compt. Rendus Méc. **342**(10–11), 570–582 (2014)
22. Campos Pinto, M., Mounier, M., Sonnendrücker, E.: Handling the divergence constraints in Maxwell and Vlasov–Maxwell simulations. Appl. Math. Comput. **272**, 403–419 (2016)
23. Campos Pinto, M., Güçlü, Y.: Broken-FEEC discretizations and Hodge Laplace problems. Preprint at arXiv:2109.02553 (2022)
24. Campos Pinto, M., Kormann, K., Sonnendrücker, E.: Variational framework for structure-preserving electromagnetic particle-in-cell methods. J. Sci. Comput. **91**, 46 (2022)
25. Campos Pinto, M., Schnack, F.: Bounded commuting projections for multipatch spaces with non-matching interfaces. arXiv:2303.14449 (2023)
26. Caorsi, S., Fernandes, P., Raffetto, M.: On the convergence of Galerkin finite element approximations of electromagnetic eigenproblems. SIAM J. Numer. Anal. **38**(2), 580–607 (2000) (electronic)
27. da Veiga, L.B., Buffa, A., Sangalli, G., Vázquez, R.: Mathematical analysis of variational isogeometric methods. Acta Numer. **23**, 157–287 (2014)
28. da Veiga, L.B., Brezzi, F., Dassi, F., Marini, L.D., Russo, A.: Virtual element approximation of 2d magnetostatic problems. Comput. Methods Appl. Mech. Eng. **327**, 173–195 (2017)
29. Dauge, M.: Benchmark computations for Maxwell equations for the approximation of highly singular solutions. http://perso.univ-rennes1.fr/monique.dauge/benchmax.html. Accessed 06 Oct 2022

30. Duruflé, M.: Numerical integration and high order finite element methods applied to time-harmonic Maxwell equations. Ph.D. thesis, Université Paris Dauphine (2006)
31. Gerritsma, M.: Edge functions for spectral element methods. In: Spectral and High Order Methods for Partial Differential Equations, pp. 199–207. Springer, Heidelberg (2011)
32. Gïçlü, Y., Hadjout, S., Ratnani, A.: PSYDAC: a high-performance IGA library in Python. In: Eccomas2022. https://www.scipedia.com/public/Guclu_et_al_2022a
33. Gross, P.W., Robert Kotiuga, P.: Electromagnetic Theory and Computation: A Topological Approach, vol. 48. Cambridge University Press, Cambridge (2004)
34. Hiptmair, R.: Discrete Hodge operators. Numer. Math. **90**(2), 265–289 (2001)
35. Hiptmair, R.: Finite elements in computational electromagnetism. Acta Numer. **11**, 237–339 (2002)
36. Holderied, F., Possanner, S., Ratnani, A., Wang, X.: Structure-preserving vs. standard particle-in-cell methods: the case of an electron hybrid model. J. Comput. Phys. **402**, 109108 (2020)
37. Holderied, F., Possanner, S., Wang, X.: MHD-kinetic hybrid code based on structure-preserving finite elements with particles-in-cell. J. Comput. Phys. **433**, 110143 (2021)
38. Hyman, J.M., Shashkov, M.: Mimetic discretizations for Maxwell's equations. J. Comput. Phys. **151**(2), 881–909 (1999)
39. Jackson, A., Sheyko, A., Marti, P., Tilgner, A., Cébron, D., Vantieghem, S., Simitev, R., Busse, F., Zhan, X., Schubert, G., et al.: A spherical shell numerical dynamo benchmark with pseudo-vacuum magnetic boundary conditions. Geophys. J. Int. **196**(2), 712–723 (2014)
40. Kraus, M., Kormann, K., Morrison, P.J., Sonnendrücker, E.: GEMPIC: geometric electromagnetic particle-in-cell methods. J. Plasma Phys. **83**(04), 905830401 (2017)
41. Kreeft, J., Palha, A., Gerritsma, M.: Mimetic framework on curvilinear quadrilaterals of arbitrary order. arXiv:1111.4304 (2011)
42. Monk, P.: An analysis of Nédélec's method for the spatial discretization of Maxwell's equations. J. Comput. Appl. Math. **47**(1), 101–121 (1993)
43. Monk, P., Demkowicz, L.: Discrete compactness and the approximation of Maxwell's equations in R3. Math. Comput. **70**, 507–523 (2001)
44. Moon, H., Teixeira, F.L., Omelchenko, Y.A.: Exact charge-conserving scatter-gather algorithm for particle-in-cell simulations on unstructured grids: a geometric perspective. Comput. Phys. Commun. **194**, 43–53 (2015)
45. Nédélec, J.-C.: Mixed finite elements in R^3. Numer. Math. **35**(3), 315–341 (1980)
46. Perse, B., Kormann, K., Sonnendrücker, E.: Geometric particle-in-cell simulations of the Vlasov–Maxwell system in curvilinear coordinates. SIAM J. Sci. Comput. **43**(1), B194–B218 (2021)
47. Robidoux, N.: Polynomial histopolation, superconvergent degrees of freedom and pseudospectral discrete Hodge operators (2008) (unpublished)
48. Schumaker, L.: Spline Functions: Basic Theory, 3rd edn. Cambridge University Press, Cambridge (2007)
49. Whitney, H.: Geometric integration theory. Princeton University Press, Princeton (1957)

Publisher's Note Springer Nature remains neutral with regard to jurisdictional claims in published maps and institutional affiliations.